

# Nanomaterials for Electrochemical Energy Conversion and Storage Technologies

Lead Guest Editor: Suresh K. Balasingam

Guest Editors: S. N. Karthick, Mohammed H. Abdul Jabbar,  
Ananthakumar Ramadoss, Sathish K. Kamaraj, and Manab Kundu





---

# **Nanomaterials for Electrochemical Energy Conversion and Storage Technologies**

## **Nanomaterials for Electrochemical Energy Conversion and Storage Technologies**

Lead Guest Editor: Suresh K. Balasingam

Guest Editors: Karthick Sivalingham Nallathambi,  
Mohammed H. Abdul Jabbar, Ananthakumar Ramadoss,  
Sathish K. Kamaraj, and Manab Kundu



---

Copyright © 2019 Hindawi. All rights reserved.

This is a special issue published in "Journal of Nanomaterials." All articles are open access articles distributed under the Creative Commons Attribution License, which permits unrestricted use, distribution, and reproduction in any medium, provided the original work is properly cited.

## Editorial Board

- Domenico Acierno, Italy  
Katerina Aifantis, USA  
Nageh K. Allam, USA  
Margarida Amaral, Portugal  
Martin Andersson, Sweden  
Raul Arenal, Spain  
Ilaria Armentano, Italy  
Vincenzo Baglio, Italy  
Lavinia Balan, France  
Thierry Baron, France  
Andrew R. Barron, USA  
Stefano Bellucci, Italy  
Enrico Bergamaschi, Italy  
D. Bhattacharyya, New Zealand  
Sergio Bietti, Italy  
Giovanni Bongiovanni, Italy  
Mohamed Bououdina, Bahrain  
Victor M. Castaño, Mexico  
Albano Cavaleiro, Portugal  
Bhanu P. S. Chauhan, USA  
Shafiq Chowdhury, USA  
Yu-Lun Chueh, Taiwan  
Elisabetta Comini, Italy  
Giuseppe Compagnini, Italy  
David Cornu, France  
Miguel A. Correa-Duarte, Spain  
P. Davide Cozzoli, Italy  
Anuja Datta, USA  
Loretta L. Del Mercato, Italy  
Yong Ding, USA  
Yu Dong, Australia  
Zehra Durmus, Turkey  
Joydeep Dutta, Oman  
Ovidiu Ersen, France  
Ana Espinosa, France  
Claude Estournès, France  
Giuliana Faggio, Italy  
Andrea Falqui, Saudi Arabia  
Matteo Ferroni, Italy  
Ilaria Fratoddi, Italy  
Siddhartha Ghosh, Singapore  
Filippo Giubileo, Italy  
Fabien Gasset, Japan  
Jean M. Greneche, France
- Kimberly Hamad-Schifferli, USA  
Simo-Pekka Hannula, Finland  
Michael Harris, USA  
Yasuhiko Hayashi, Japan  
Michael Z. Hu, USA  
Nay Ming Huang, Malaysia  
Zafar Iqbal, USA  
Balachandran Jeyadevan, Japan  
J.-w. Kang, Republic of Korea  
Hassan Karimi-Maleh, Iran  
Antonios Kelarakis, UK  
Alireza Khataee, Iran  
Ali Khorsand Zak, Iran  
Philippe Knauth, France  
Prashant Kumar, UK  
Eric Le Bourhis, France  
Jun Li, Singapore  
Meiyong Liao, Japan  
Shijun Liao, China  
Silvia Licoccia, Italy  
Nathan C. Lindquist, USA  
Zainovia Lockman, Malaysia  
Jim Low, Australia  
Gaurav Mago, USA  
Muhamamd A. Malik, UK  
Francesco Marotti de Sciarra, Italy  
Ivan Marri, Italy  
Laura Martinez Maestro, UK  
Sanjay R. Mathur, Germany  
Tony McNally, UK  
Yogendra Mishra, Germany  
Paulo Cesar Morais, Brazil  
Paul Munroe, Australia  
J.-M. Myoung, Republic of Korea  
Rajesh R. Naik, USA  
Albert Nasibulin, Russia  
Toshiaki Natsuki, Japan  
Hiromasa Nishikiori, Japan  
Natalia Noginova, USA  
Sherine Obare, USA  
Won-Chun Oh, Republic of Korea  
Abdelwahab Omri, Canada  
Ungyu Paik, Republic of Korea  
Edward A. Payzant, USA
- Alessandro Pegoretti, Italy  
Oscar Perales-Pérez, Puerto Rico  
Jorge Pérez-Juste, Spain  
Alexey P. Popov, Finland  
Thathan Premkumar, Republic of Korea  
Helena Prima-García, Spain  
Alexander Pyatenko, Japan  
Haisheng Qian, China  
You Qiang, USA  
Philip D. Rack, USA  
Mohammad Rahimi-Gorji, Belgium  
Peter Reiss, France  
Ilker S. Bayer, Italy  
Lucien Saviot, France  
Sudipta Seal, USA  
Shu Seki, Japan  
Donglu Shi, USA  
Bhanu P. Singh, India  
Surinder Singh, USA  
Vladimir Sivakov, Germany  
Adolfo Speghini, Italy  
Kishore Sridharan, India  
Marinella Striccoli, Italy  
Fengqiang Sun, China  
Ashok K. Sundramoorthy, India  
Angelo Taglietti, Italy  
Bo Tan, Canada  
Leander Tapfer, Italy  
Valeri P. Tolstoy, Russia  
Muhammet S. Toprak, Sweden  
R. Torrecillas, Spain  
Achim Trampert, Germany  
Takuya Tsuzuki, Australia  
Tamer Uyar, Turkey  
Luca Valentini, Italy  
Antonio Vassallo, Italy  
Ester Vazquez, Spain  
Ajayan Vinu, Australia  
Ruibing Wang, Macau  
Shiren Wang, USA  
Yong Wang, USA  
Magnus Willander, Sweden  
Ping Xiao, UK  
Zhi Li Xiao, USA



---

Yingchao Yang, USA  
Yoke K. Yap, USA  
Dong Kee Yi, Republic of Korea

Jianbo Yin, China  
William Yu, USA  
Michele Zappalorto, Italy

Renyun Zhang, Sweden

## Contents

### **Nanomaterials for Electrochemical Energy Conversion and Storage Technologies**

Suresh Kannan Balasingam , Karthick Sivalingam Nallathambi , Mohammed Hussain Abdul Jabbar , Ananthakumar Ramadoss , Sathish Kumar Kamaraj , and Manab Kundu   
Editorial (2 pages), Article ID 1089842, Volume 2019 (2019)

### **Electrode Composite LiFePO<sub>4</sub>@Carbon: Structure and Electrochemical Performances**

Le Thanh Nguyen Huynh , Hoang Hai Au Nguyen, Thi Thuy Dung Tran, Thi Thu Trang Nguyen, Thi My Anh Nguyen, Thi Hang La, Van Man Tran, and My Loan Phung Le   
Research Article (10 pages), Article ID 2464920, Volume 2019 (2019)

### **Decreased Surface Photovoltage of ZnO Photoanode Films via Optimal Annealing Temperature for Enhanced Photoelectrochemical Performance**

Yichong Liu, Bohuai Xiao, Haijian Chen, Yunchuan Li , and Shuai Chang   
Research Article (8 pages), Article ID 9367573, Volume 2019 (2019)

### **Determination of Cyclability of Li/FeS<sub>2</sub> Batteries Based on Measurement of Coulombic Efficiency**

Paul Maldonado Nogales, Hee-Youb Song, and Soon-Ki Jeong   
Research Article (6 pages), Article ID 5263132, Volume 2018 (2019)

### **Experimental Study of Al<sub>2</sub>O<sub>3</sub> Nanofluids on the Thermal Efficiency of Curved Heat Pipe at Different Tilt Angle**

S. Razvarz  and R. Jafari   
Research Article (7 pages), Article ID 1591247, Volume 2018 (2019)

### **Porous Activated Carbons Derived from *Pleurotus eryngii* for Supercapacitor Applications**

Yudan Yuan , Ruowei Yi, Yi Sun, Jianqiao Zeng, Jiaqi Li, Jiahao Hu, Yinchao Zhao, Wei Sun, Chun Zhao, Li Yang , and Cezhou Zhao   
Research Article (10 pages), Article ID 7539509, Volume 2018 (2019)

### **Hierarchical N- and O-Doped Porous Carbon Composites for High-Performance Supercapacitors**

Ben-Xue Zou , Yan Wang, Xiaodong Huang, and Yanhua Lu   
Research Article (12 pages), Article ID 8945042, Volume 2018 (2019)

## Editorial

# Nanomaterials for Electrochemical Energy Conversion and Storage Technologies

**Suresh Kannan Balasingam** <sup>1</sup>, **Karthick Sivalingam Nallathambi** <sup>2</sup>,  
**Mohammed Hussain Abdul Jabbar** <sup>3</sup>, **Ananthakumar Ramadoss** <sup>4</sup>,  
**Sathish Kumar Kamaraj** <sup>5</sup>, and **Manab Kundu** <sup>6</sup>

<sup>1</sup>Department of Materials Science and Engineering, Norwegian University of Science and Technology (NTNU), Trondheim 7491, Norway

<sup>2</sup>Electrochemical Materials and Devices Lab, Department of Chemistry, Bharathiar University, Coimbatore 641046, India

<sup>3</sup>Department of Materials Science and Engineering, University of Maryland, College Park, Maryland 20740, USA

<sup>4</sup>Laboratory for Advanced Research in Polymeric Materials (LARPM), Central Institute of Plastic Engineering and Technology (CIPET), Bhubaneswar 751024, India

<sup>5</sup>Laboratory of the Sustainable Environment, Technological Institute of El Llano Aguascalientes (ITEL)/National Technological Institute of Mexico (TecNM), Aguascalientes C.P. 20330, Mexico

<sup>6</sup>Department of Chemistry, SRM Institute of Science and Technology, Chennai 603203, India

Correspondence should be addressed to Suresh Kannan Balasingam; [suresh.k.balasingam@ntnu.no](mailto:suresh.k.balasingam@ntnu.no)

Received 20 December 2018; Accepted 20 December 2018; Published 11 April 2019

Copyright © 2019 Suresh Kannan Balasingam et al. This is an open access article distributed under the Creative Commons Attribution License, which permits unrestricted use, distribution, and reproduction in any medium, provided the original work is properly cited.

In this modern era, our society faces a serious energy crisis due to increasing human population. Energy consumption starts from small-scale electronic gadgets to high power consuming electric vehicles. To supply power on demand, researchers focus on alternative renewable energy resources including solar energy, wind energy, hydropower, geothermal energy, and bioenergy. Effectively, energy conversion and storage technologies such as solar cells, fuel cells, secondary batteries, supercapacitors, and other self-powered systems are under rigorous investigation. The efficient energy conversion and storage performance of those technologies rely on material properties of their electrode, electrolyte, and other device components. It is recently known that nanostructuring of device components leads to enhanced efficiency in terms of robustness and reliability of the energy conversion and storage systems. Moreover, the nanostructured materials have attracted great interest due to their unique physicochemical and electrochemical properties. Hence, the utilization of such materials in nanodimensions will create enormous impact on the efficiency of various

energy conversion and storage devices. The main objective of this special issues is to identify the significant research paradigms of nanomaterials and their potential impacts on applications. In particular, focus of this issue is on the synthesis and characterization of nanostructured materials for various applications such as supercapacitors, batteries, photoelectrochemical, and thermal enhancement systems.

The highlights of the published articles are summarized as follows. In this special issue, Y. Yuan et al. synthesized the porous activated carbon materials from *Pleurotus eryngii*-based biomass material *via* carbonization, followed by KOH activation and utilized it for supercapacitor applications. The as-prepared activated carbon presented a large specific area with high porosity which exhibited a maximum specific capacitance of  $195 \text{ F g}^{-1}$  with 93% capacitance retention after 15000 cycles. It is known that *Pleurotus eryngii* is one of the readily available sources of carbon materials, potentially suitable for supercapacitor applications. Also, this biomass can be the resource for development of porous activated carbon for other energy conversion and storage devices

in the future. Further, B.-X. Zou et al. synthesized hierarchical porous N, O-doped carbon composites by combining low molecular weight phenol resin and silk fibers in various combinations using a hydrothermal method and carbonization process. The as-prepared electroactive materials showed a low resistance and good surface area with hierarchical porosity. The low molecular phenol resin and silk fiber combination increases the surface area and enhanced the electron transport within the active materials. The fabricated symmetric device delivered a maximum energy density of  $7.4 \text{ Wh kg}^{-1}$  and power density of  $90.1 \text{ W kg}^{-1}$  using aqueous electrolyte.

L. T. N. Huynh et al. prepared the  $\text{LiFePO}_4$ @carbon composite material by hydrothermal method followed by thermal treatment for lithium-ion battery application. The different calcination processes did not affect the olivine structure; however, the surface morphology, the quality of carbon coating, and the electrochemical properties were significantly changed. The sample annealed at  $700^\circ\text{C}$  showed a good specific capacity of  $170 \text{ mAh g}^{-1}$  and the decent cyclic stability up to 120 cycles due to an optimum amount of carbon coating over olivine material. In another lithium-ion battery article, P. M. Nogales et al. developed a new method to estimate the ageing evaluation of Li-ion batteries in a shorter time. The authors present the numerical analysis method using coulombic efficiency and capacity loss rate that could determine the cyclic stability of electrode material within a shorter evaluation time.

Y. Liu and coworkers investigated the effect of surface defects density of zinc oxide films on the photoelectrochemical water splitting reaction. The surface defect density of zinc oxide photoanodes was tuned by annealing the electrodes at various temperatures. The surface photovoltage of ZnO films was obtained by Kelvin probe force microscopy. The sample annealed at  $450^\circ\text{C}$  showed minimum surface photovoltage, which confirmed that the low surface defect density sample showed enhancement in photoelectrochemical water oxidation. The applied bias photon-to-current efficiency of annealed ZnO photoanode reached to 0.237%, about 7.4 times higher than that of unannealed ZnO photoanode. This work provided a potential method to design innovative photoanodes for photoelectrochemical water splitting.

S. Razvarz et al. performed the experimental research on thermal enhancement related to the heat pipe (with  $\text{Al}_2\text{O}_3$  nanopowder) at different tilt angle. The important observation is the increase in heat transfer coefficient with the increasing heat flux of the evaporator. While adding  $\text{Al}_2\text{O}_3$  nanoparticles to pure water, the thermal efficiency of the heat pipe enhanced considerably. Optimizing the quantity of the  $\text{Al}_2\text{O}_3$  nanopowder assists in thermal efficiency enhancement. Also, the heat pipe thermal efficiency enhanced with increasing nanoparticle concentrations and tilt angles.

## Conflicts of Interest

We declare that there is no conflict of interests or private agreement with companies regarding our work for this special issue. We have no financial relationship through

employment, consultancies, and either stock ownership or honoraria with industry.

## Acknowledgments

We would like to thank all the contributed authors and referees of this special issue, also grateful to the editorial board for the smoother process flow and rapid publication. The lead editor would like to thank all the editors for their time spent in reviewing and assigning reviewers for the submitted manuscripts.

*Suresh Kannan Balasingam  
Karthick Sivalingam Nallathambi  
Mohammed Hussain Abdul Jabbar  
Ananthakumar Ramadoss  
Sathish Kumar Kamaraj  
Manab Kundu*

## Research Article

# Electrode Composite $\text{LiFePO}_4$ @Carbon: Structure and Electrochemical Performances

Le Thanh Nguyen Huynh <sup>1</sup>, Hoang Hai Au Nguyen,<sup>1</sup> Thi Thuy Dung Tran,<sup>1</sup>  
Thi Thu Trang Nguyen,<sup>2</sup> Thi My Anh Nguyen,<sup>3</sup> Thi Hang La,<sup>4,5</sup> Van Man Tran,<sup>1,6</sup>  
and My Loan Phung Le <sup>1,6</sup>

<sup>1</sup>Applied Physical Chemistry Laboratory (APCLAB), VNUHCM-University of Science, Vietnam

<sup>2</sup>Faculty of Chemistry, HCMC University of Education, Vietnam

<sup>3</sup>Faculty of Material Technology, VNUHCM-University of Technology, Vietnam

<sup>4</sup>Graduate University of Science & Technology – VAST, Vietnam

<sup>5</sup>Vinh Long University of Technology Education (VLUTE), Vietnam

<sup>6</sup>Department of Physical Chemistry, Faculty of Chemistry, VNUHCM-University of Science, Vietnam

Correspondence should be addressed to Le Thanh Nguyen Huynh; [hltnguyen@hcmus.edu.vn](mailto:hltnguyen@hcmus.edu.vn)  
and My Loan Phung Le; [lmphung@hcmus.edu.vn](mailto:lmphung@hcmus.edu.vn)

Received 19 May 2018; Accepted 1 October 2018; Published 4 February 2019

Guest Editor: Sathish K. Kamaraj

Copyright © 2019 Le Thanh Nguyen Huynh et al. This is an open access article distributed under the Creative Commons Attribution License, which permits unrestricted use, distribution, and reproduction in any medium, provided the original work is properly cited.

This work aimed at preparing the electrode composite  $\text{LiFePO}_4$ @carbon by hydrothermal and the calcination process was conducted at 600, 700, and 800°C. The structure and morphology were determined by X-ray diffraction (XRD), SEM, Raman spectroscopy, X-ray photon spectroscopy (XPS), and thermal analysis. The XRD refinement's results point out the orthorhombic structure without impurity phase and the high crystalline of synthesized olivines. The results of Raman spectroscopy and XPS confirmed the pure olivine phase as well as the successful carbon coating on the surface of olivines' powders. Moreover, the calcinated temperature affected the morphology as well as the electrochemical performance of synthesized olivines. The electrochemical measurements were conducted by cyclic voltammetry and galvanostatic cycling test. The diffusion coefficients were calculated from cyclic voltammetry curves and reached  $1.09 \times 10^{-12}$  cm<sup>2</sup>/s for LFP600,  $2.28 \times 10^{-11}$  cm<sup>2</sup>/s for LFP700, and  $3.27 \times 10^{-12}$  cm<sup>2</sup>/s LFP800. The cycling test at rate C/10 exhibited an excellent cyclability with discharge capacity of 145 mAh/g for LFP600, 170 mAh/g for LFP700, and 160 mAh/g for LFP800.

## 1. Introduction

The pioneer work of Padhi et al. [1] launched the reversible Li insertion into the olivine phase  $\text{LiFePO}_4$  with a delivered capacity of 120 mAh/g. Thenceforth, the olivine has been paid attention in the context of cathode materials for lithium-ion batteries (LIBs) because of their advantages in regard to economy (low toxicity, low cost, and high safety) as well as electrochemical performance (excellent cyclability and high-rate capability) [2]. The olivine structure consists of a distorted hexagonal-close-packed oxygen framework; the  $\text{Fe}^{2+}$  ions form the octahedrons  $[\text{FeO}_6]$  with six

surrounded oxygens and the  $\text{P}^{5+}$  ions form the tetrahedrons with four surrounded oxygens. The octahedrons  $[\text{FeO}_6]$  connect by the corner-sharing along b-axis and link with the tetrahedrons by the edge-sharing forming the 1-D channels where Li diffusion pathway is along plan (010). The strong covalency P–O in polyanion  $\text{PO}_4^{3-}$  unit steadies the olivine structure during Li-migration and lowers the Fermi level of the redox couple  $\text{Fe}^{3+}/\text{Fe}^{2+}$  through the Fe–O–P inductive effect that results the discharge voltage 3.45 V (vs.  $\text{Li}^+/\text{Li}$ ) for  $\text{LiFePO}_4$  [3–7].

However, many researches have pointed out that the drawbacks are hindered by low electronic conductivity and

TABLE 1: Summary of composite electrode LiFePO<sub>4</sub>@carbon prepared by hydrothermal method.

Authors	Hydrothermal condition	Grain's size	Temperature pyrolysis	Capacity
Brochu et al. [13]	185°C for 2 hours	240 nm thick and 1 μm length	650°C for 2 hours in argon	160 mAh/g at rate C/10
Chen et al. [14]	200°C for 6 hours	2-3 μm	600°C for 2 hours in argon	150 mAh/g at rate C/10
Lim et al. [15]	240°C from 2 to 36 hours	300–600 nm		180 mAh/g (50 cycles) at rate C/10
Jiang et al. [16]	180°C for 2 hours		700°C for 6 hours in argon	160 mAh/g (100 cycles) at rate C/10
Zhan et al. [17]	180°C for 12 hours	2-3 μm	550°C for 4 hours in argon	150 mAh/g (50 cycles) at rate C/5

sluggish Li transportation; therefore, the bulk LiFePO<sub>4</sub> electrode usually shows poor capacity retention during cycling test at both of monorate capability and high-rate capability [8–12]. To overcome these drawbacks, the strategies have been considered commonly as designing the nanostructure and coating carbon. We summarized in Table 1 the highlighted results of composite electrode LiFePO<sub>4</sub>@carbon prepared by hydrothermal method.

In this work, we prepared the electrode composite LiFePO<sub>4</sub>@carbon based on hydrothermal route and pyrolysis process at different temperature at 600, 700, and 800°C. The glucose as carbon coating source was added at the beginning of hydrothermal reaction. The electrochemical performances of LiFePO<sub>4</sub>@carbon were related to crystalline, carbon content as well as quality, and electronic-ionic conductivity which were characterized by powder X-ray diffraction, Raman spectroscopy, and cyclic voltammetry.

## 2. Experimental

**2.1. Material Preparation.** The composite electrode LiFePO<sub>4</sub>@carbon were synthesized by hydrothermal route. The 2.600 g LiOH.H<sub>2</sub>O (99.9%, Sigma-Aldrich) was dissolved in 20.0 mL distilled water. The 5.0 mL H<sub>3</sub>PO<sub>4</sub> 8.5% was dropped gradually and stirred for 10 minutes to form a white suspension. Meanwhile, the 5.600 g FeSO<sub>4</sub>.7H<sub>2</sub>O (99.9%, Sigma-Aldrich) and 1.500 g glucose (99.9%, Sigma-Aldrich) were dissolved in 30 mL distilled water in nitrogen atmosphere, and then it was added to the white suspension under vigorous stirring. The final mixture was transferred into a stainless-steel autoclave and sealed. The hydrothermal process was conducted at 190°C for 6 hours. The precipitation was collected by filtering, washing, and drying. After that, the collected powder was calcined under argon atmosphere at 600, 700, 800°C for 6 hours.

**2.2. Physical Characterization.** Powder X-ray diffraction (XRD) data were collected on a Bruker D8 Advance Diffractometer (Bruker), using a Cu Kα1 radiation source (λ = 1.5406 Å). The crystal structure of synthesized materials were analyzed by Rietveld method [18] using the Topas computer software [19]. X-ray photoelectron spectroscopy (XPS) measurements were performed on an AXIS-NOVA (Kratos) under a base pressure of 2.6 × 10<sup>-9</sup> Torr. The size and morphological feature of materials were analyzed with a scanning electron microscope (FE-SEM, S-4700N of HITACHI) with a Hitachi S-4700. Raman spectroscopy measurements were carried out on a LabRAM HR 800 Raman Spectrometer

(HORIBA Jobin Yvon) with the green line of an argon-ion laser (514 nm) as the excitation source and the Raman bands were collected in the wavelength range of 500–2000 cm<sup>-1</sup> at room temperature. Thermal analysis (TGA) was conducted with a LABSYS evo TG-DSC 1600 (Setaram, France).

**2.3. Electrochemical Measurements.** The electrochemical measurements were performed in lithium half cell into two-electrode Swagelok cell with a Li foil as negative electrode and synthesized olivine samples LiFePO<sub>4</sub>@C as positive electrode, an electrolyte of 1.0 M LiPF<sub>6</sub> in ethylene carbonate and dimethyl carbonate (EC:DMC = 1 : 1) (Sigma-Aldrich) and three Whatman glass-fiber separators. The positive electrodes were prepared using the following procedure. An 80 : 15 : 5 mixture of synthesized olivine samples LiFePO<sub>4</sub>@C, carbon black, and copolymer poly(vinylidene fluoride-co-hexafluoropropylene) PVDF-HFP (Sigma-Aldrich) binder was mixed with 1-methyl-2-pyrrolidinone (NMP) solvent to form a viscous paste. The paste was coated uniformly on aluminum foil (Al-foil) via coating machine MSK-AFA-III (MTI, USA) with a thickness of 100 μm. The coated Al-foil was dried in a vacuum oven overnight at 120°C and then cut into pellets with a diameter of 10 mm. The cells were assembled in argon-filled glovebox.

All electrochemical measurements were operated on MPG-2 apparatus (Bio-Logic, France) at room temperature. The cyclic voltammetry (CV) were carried out with scan rate from 5 to 60 μV/s, and the galvanostatic cycling tests were performed in a voltage range of 3.0–4.0 V (vs. Li<sup>+</sup>/Li).

## 3. Results and Discussion

**3.1. Structure and Morphology.** We conducted Rietveld refinements to identify the structure of three synthesized samples LFP600, LFP700, and LFP800 (Figure 1). The refinements were performed using the olivine orthorhombic structure and the space group *Pnma* [20] with Li atoms at 4a sites, Fe atoms at 4c sites, P atoms at 4c sites, and O atoms at 4c and 8a sites. The pure phases were confirmed and the fitted structural parameters and the refined results (Wyckoff positions, fractional atomic coordinate parameters) are gathered in Tables 2 and 3. The refinement's results point out the orthorhombic structure without impurity phase and the high crystalline of three synthesized olivines with the “chi-square” (χ<sup>2</sup>) below 5.

According to the Debye-Scherrer formula, the average *c* was calculated from the full width of half maximum (FWHM) of the highest intensity diffraction peak (311).

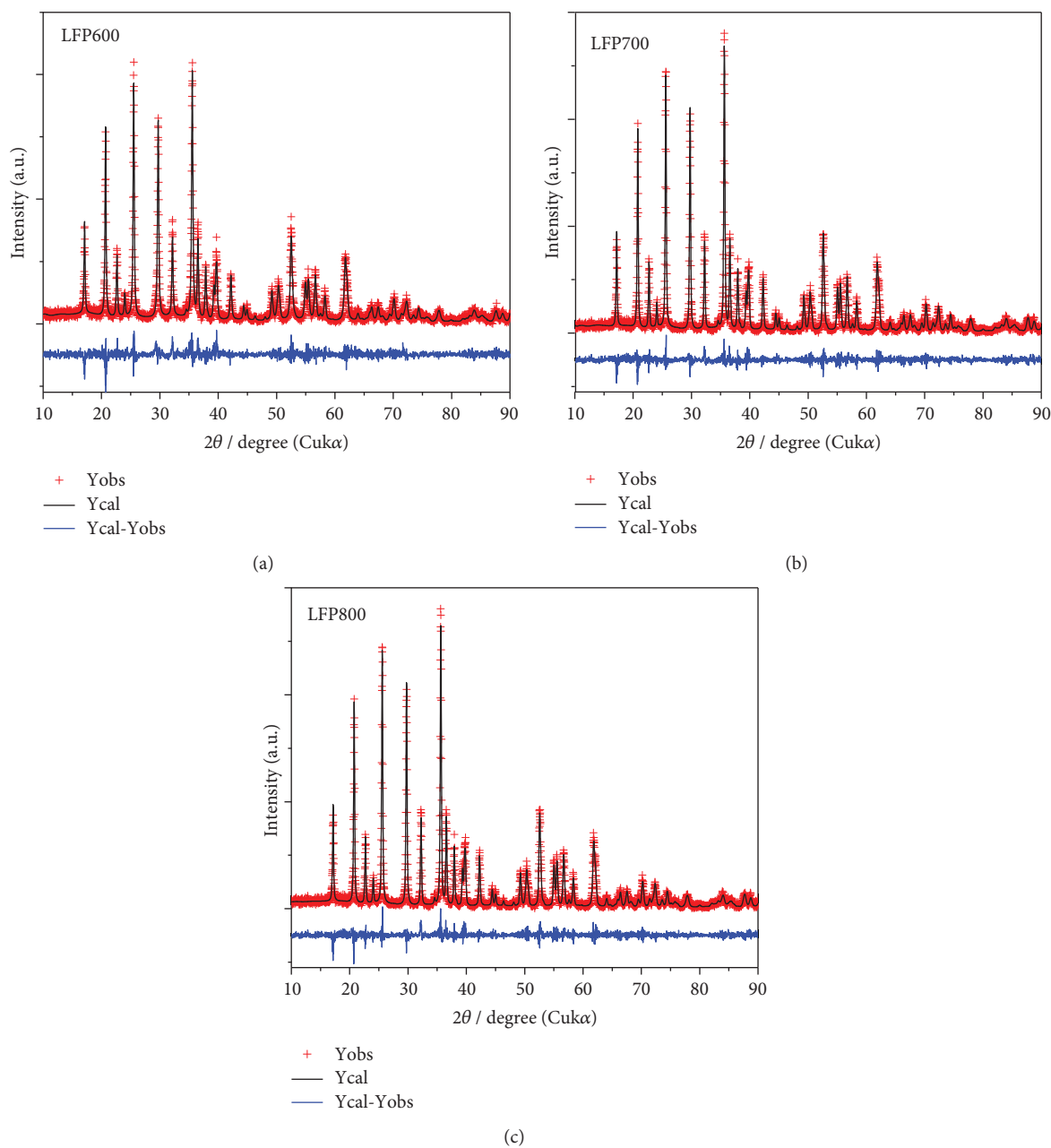


FIGURE 1: XRD patterns of olivines LFP600, LFP700, and LFP800.

TABLE 2: Lattice parameter and refinement's R-factors of LFP600, LFP700, and LFP 800.

	$a/\text{\AA}$	$b/\text{\AA}$	$c/\text{\AA}$	$V/\text{\AA}^3$	$R_{\text{exp}}$	$R_{\text{wp}}$	$\chi^2$
LFP600	10.3272	5.9971	4.6975	290.94	37.1	24.85	2.22
LFP700	10.3203	6.0009	4.6935	290.68	27.3	18.28	2.21
LFP800	10.3205	6.0003	4.6933	290.63	30.3	19.92	2.32

The crystalline sizes of the synthesized olivines were found out of 34 nm for LFP600, 49.5 nm for LFP700, and 42.6 nm for LFP800.

Figure 2 shows the morphologies of olivines' powders. The hydrothermal synthesis promotes the significant particle-size distribution, but the temperature pyrolysis

TABLE 3: Wyckoff positions, fractional atomic coordinates for the synthesized olivines.

	Wyckoff	$x$	$y$	$z$	Occupy
Li	4a	0	0	0	1
Fe	4c	0.2822	0.25	0.9747	1
P	4c	0.0948	0.25	0.4192	1
O1	4c	0.0968	0.25	0.7430	1
O2	4c	0.4567	0.25	0.2060	1
O3	8d	0.1656	0.0466	0.2847	1

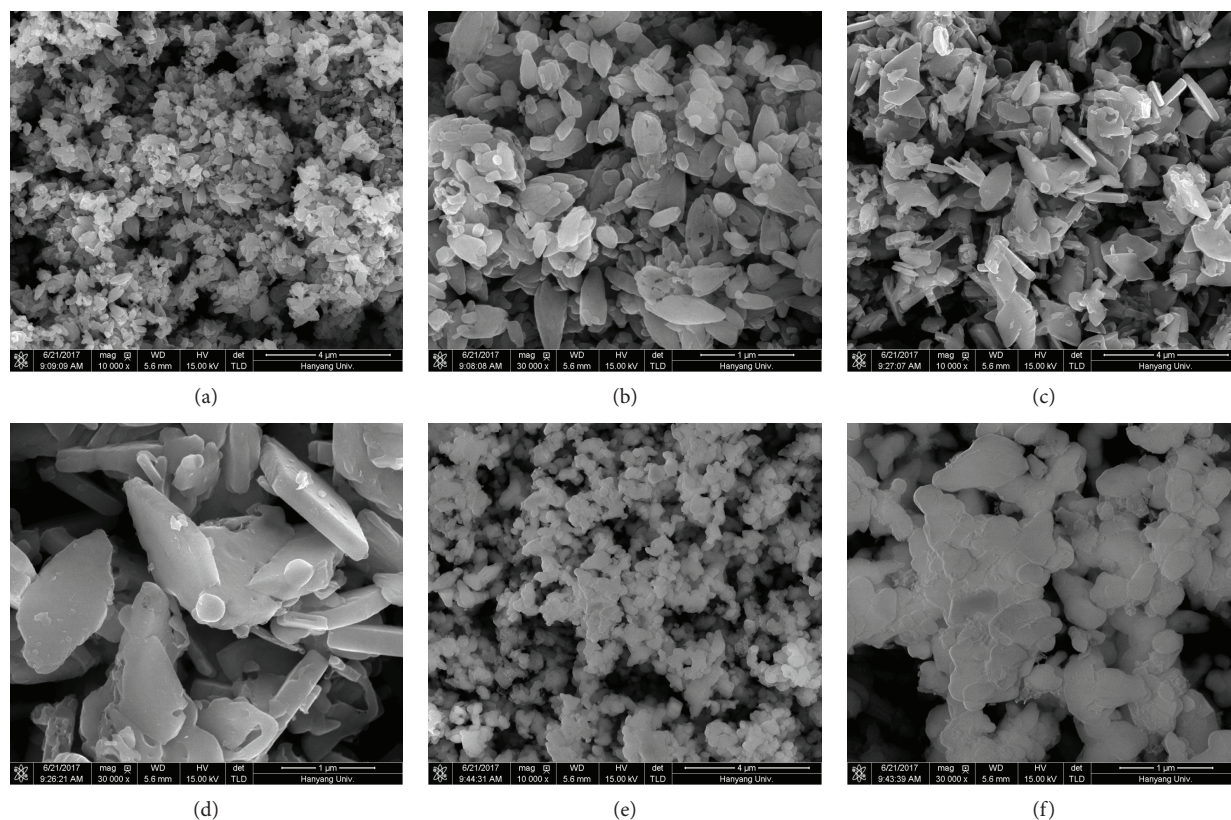


FIGURE 2: SEM images of LFP600 (a, b), LFP700 (c, d), and LFP800 (e, f).

indicates the variation of particle shape. The olivines' powders distribute in the submicrometric; the particle size of LFP600 significantly varied in a large range from 200 to 500 nm with the undefined shapes, LFP700 exhibited the thin-plate particles with a thickness of 200 nm and other dimensions around 800 nm, and LFP800 particles came up with a more spherical shape with about 250 nm dimension.

Three Raman spectra of olivines' powders in Figure 3 exhibit two broad lines in high-frequency region at  $1345$  and  $1583\text{ cm}^{-1}$  which are the fingerprint of carbon. The band at  $1583\text{ cm}^{-1}$  is assigned to the G-band of  $E_{2g}$  mode of crystalline graphite, while the band at  $1345\text{ cm}^{-1}$  is assigned to the D-band of edge modes of disordered graphite. Note that the D-band/G-band intensity ratio characterizes the yield of graphitic bonding in amorphous carbon and the low D-line/G-line ratio encourages the electronic and ionic conductivity [21, 22]. We observed the D-line/G-line ratio of olivine samples following 1.04 for LFP600, 0.87 for LFP700, and 0.96 for LFP800 that indicates the calcination process at  $700^\circ\text{C}$  could increase the graphitization of carbon coating.

X-ray photoelectron spectroscopy (XPS) analysis was performed to examine the valence state of chemical elements of synthesized olivines. Figure 4(a) shows the analog XPS profiles of three olivines' powders in the full scan. For more detail in the narrow scan, the Fe 2p spectra (Figure 4(b)) confirm the  $\text{Fe}^{2+}$  valence state with the spin-orbit coupling by two peaks at a binding energy (BE) of  $710.5$  (Fe 2p<sub>1/2</sub>) and  $723\text{ eV}$  (Fe 2p<sub>3/2</sub>) [23–27].

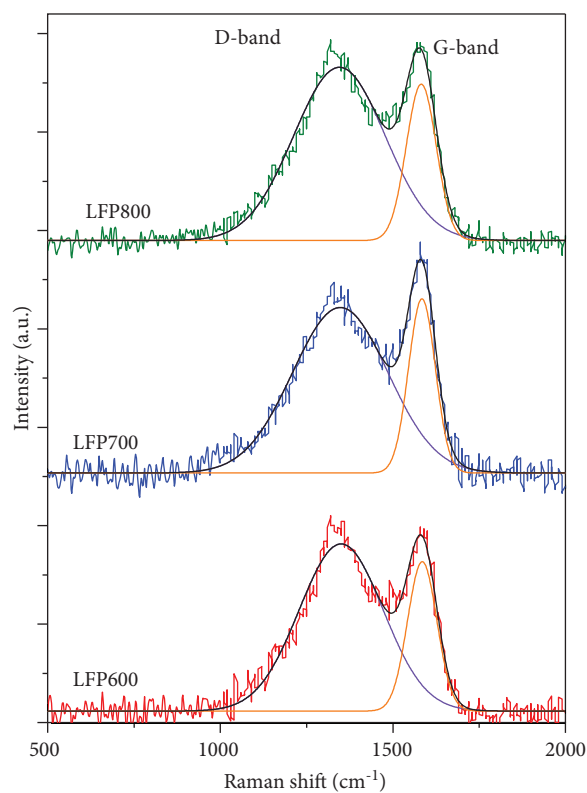


FIGURE 3: Raman spectroscopy of LFP600, LFP700, and LFP800.

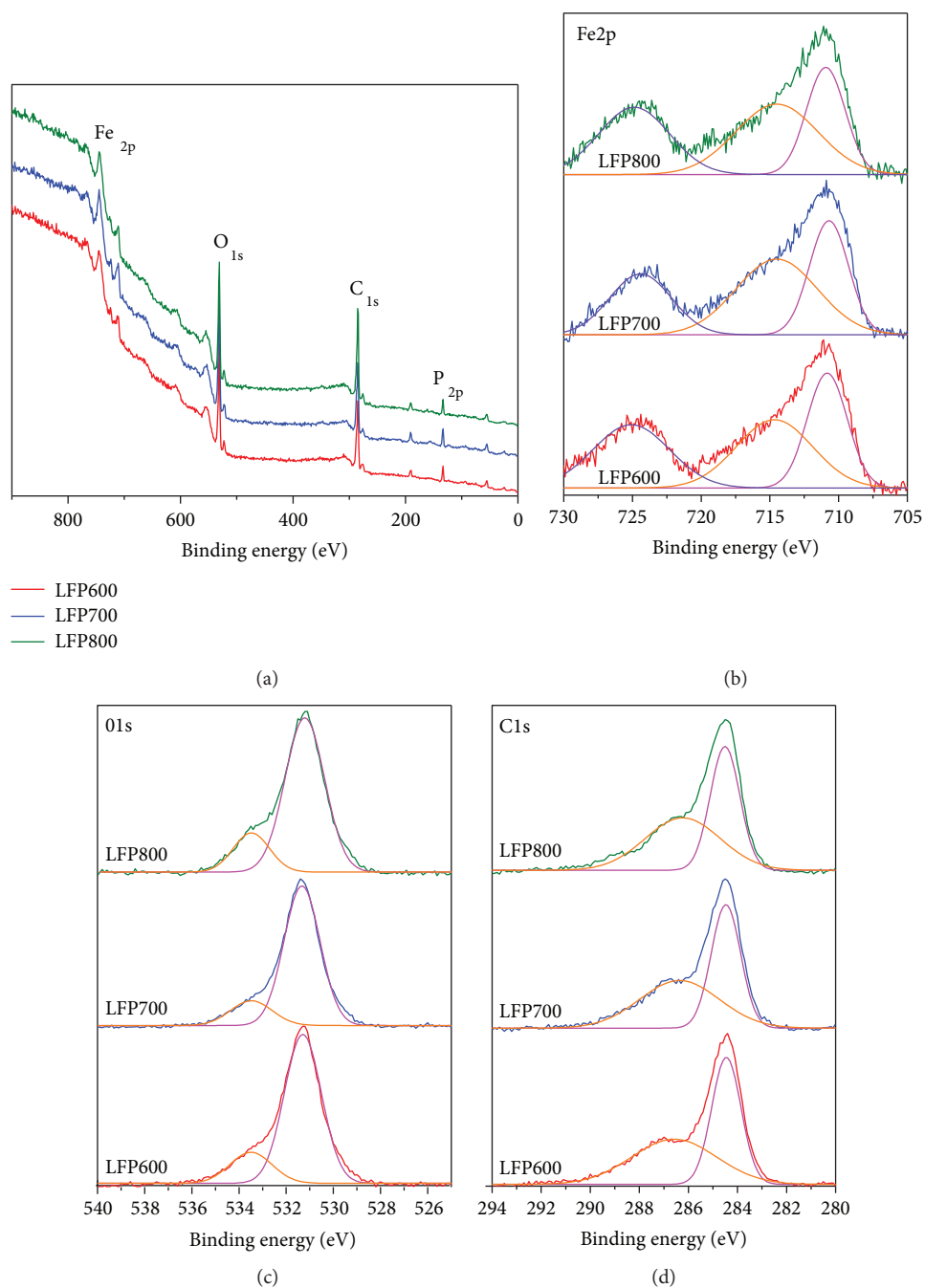


FIGURE 4: (a) Full-scan profiles of olivine samples; narrow-scan profile of Fe2p (b), O1s (c), and C1s (d).

The two peaks at BE of 531.7 eV and 533.5 eV (Figure 4(c)) can be assigned to the oxygen divalent (O1s), attributing the lattice oxygen  $O^{2-}$  in P–O bond at the normal sites of the orthorhombic structure. The C1s peak (Figure 4(d)) at BE of 284 eV corresponds to the carbon coating on the surface of olivine powders. The peak at BE of 133 eV is related to the  $P^{5+}$  valent (P1s) in  $PO_4^{3-}$  group [23, 28–30]. Both results of Raman spectroscopy and XPS confirm the pure olivine phase as well as the successful carbon coating on the surface of olivines' powders.

TGA were operated on the olivine powders to determine the amount of carbon coating under flow of air

and with heating rate of  $10^\circ\text{C}/\text{min}$ . The TGA curves demonstrate a similar trend as shown on Figure 5. Below  $200^\circ\text{C}$ , a slight weight loss was observed due to evaporation of adsorbed water on particle surface; above  $200^\circ\text{C}$ , a weight gain was observed which was supposed to be the result of oxidation of  $LiFePO_4$  in air and a theoretical weight gain of 5.07% [31]. Meanwhile, in the same temperature range, the carbon coated on nanoparticles is also oxidized into carbon dioxide and leads to a decrease in weight. Hence, taking the initial weight loss due to evaporated water, the amount of coated carbon can be presumed in Table 4.

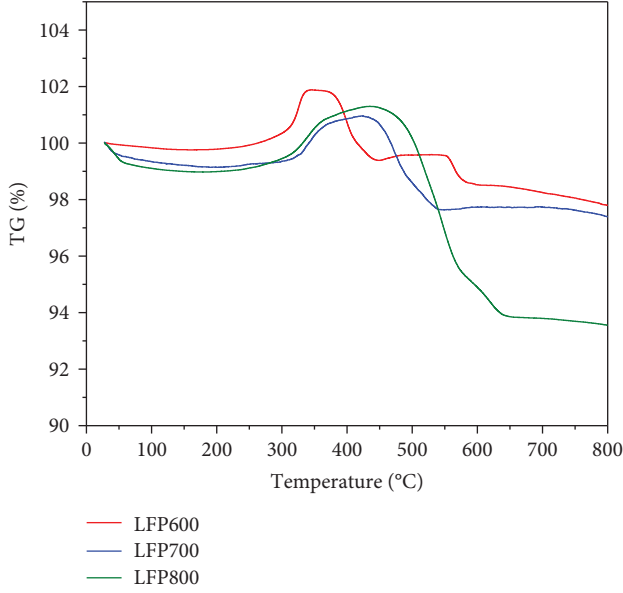


FIGURE 5: TGA curves of LFP600, LFP700, and LFP800.

TABLE 4: Amount of carbon coating on  $\text{LiFePO}_4$ .

Sample	LFP600	LFP700	LFP800
Carbon coating (%)	3	4	3.5

**3.2. Electrochemical Performance.** Electrochemical properties of the olivine samples were performed by cyclic voltammetry (CV) and galvanostatic cycling test between 3 and 4 V (vs.  $\text{Li}^+/\text{Li}$ ). Figures 6(a)–6(c) illustrate the CV profiles of olivines LFP600, LFP700, and LFP800 in scan rate from  $5 \mu\text{V/s}$  to  $60 \mu\text{V/s}$ . In each scan rate, the CV curve possessed one unique anodic peak as well as cathodic peak. The CV curves abided by the motif of two-phase mechanism that means the Li migration occurs through regions  $\text{LiFePO}_4$  and  $\text{FePO}_4$ , indicated by a reversible redox couple  $\text{Fe}^{3+}/\text{Fe}^{2+}$ . Following the increase of scan rate, the anode peaks shifted gradually towards positive direction while the cathode peaks also step backwards in a negative direction. The reverse shift between anodic peaks and cathodic peaks gave a signal of polarization in galvanostatic charge-discharge test at high rates.

The diffusion coefficient of lithium ion ( $D_{\text{Li}}$ ) can be calculated by Randles-Sevcik equation due to the reversible reaction of redox couple  $\text{Fe}^{3+}/\text{Fe}^{2+}$ , which is showed by the relationship between the cathodic peak current and the square root of scan rates.

$$i_p = 0.4463nFAC \left( \frac{nFvD}{RT} \right)^{1/2}, \quad (1)$$

whereas  $i_p$  (A) is cathodic peak current,  $n$  is the number of electron transfer in redox reaction ( $n=1$  for  $\text{LiFePO}_4$ ),  $F$  (C/mol) is the Faraday constant,  $A$  is electrode area ( $0.785 \text{ cm}^2$ ),  $C$  (mol/cm<sup>3</sup>) is concentration of mobility ion in structure,  $v$  (V/s) is scan rate,  $D$  (cm<sup>2</sup>/s) is diffusion

coefficient,  $R$  (J/K.mol) is the gas constant, and  $T$  (K) is temperature.

Figure 6(d) shows the significant linear relationship between the cathodic peak current and the square root of scan rates of olivine samples. The slope of LFP700 was higher than those of LFP600 and LFP800, suggesting the fast Li transportation of LFP700. The  $D_{\text{Li}}$  were found out  $1.09 \times 10^{-12} \text{ cm}^2/\text{s}$  for LFP600,  $2.28 \times 10^{-11} \text{ cm}^2/\text{s}$  for LFP700, and  $3.27 \times 10^{-12} \text{ cm}^2/\text{s}$  for LFP800; these results were higher than the results determined by CV, GITT, and EIS methods [6, 8]. Moreover, the Li diffusion of LFP700 was one order of magnitude larger than those of LFP600 and LFP800 due to the high amount as well as the high quality of carbon coating.

The Li insertion into olivine phase of  $\text{LiFePO}_4$  can be described by a domino-cascade mechanism with a reciprocal phase transition between  $\text{LiFePO}_4$  and  $\text{FePO}_4$ ; the Li insertion pathway is routed through channels of (010) plane. The galvanostatic curve of  $\text{LiFePO}_4$  is characterized by two long plateaux at 3.40 V for reduction process and 3.45 V for oxidation process, corresponding to the reversible redox peaks in CV curve. The cycling tests of olivines were conducted at rate C/10 (17 mA/g). The typical charge-discharge curves of LFP700 in Figure 7(a) illustrate a low polarization of 70 mV between the mid-discharge potential and the midcharge potential; moreover, the middischarge potential is not influenced upon cycling test. That confirms the structural stability during the Li migration.

Figure 7(b) shows the cycling performance of synthesized olivines upon 120 cycles. We observed the increase of capacities during the first twenty cycles due to the initial surface activation on the electrode  $\text{LiFePO}_4$  [32]. The olivines pointed out the quite stable performance in cycling test at rate C/10. The capacities reached 145 mAh/g for LFP600, 170 mAh/g for LFP700, and 160 mAh/g for LFP800. The better performance of LFP700 than LFP600 and LFP800 can be explained by the high amount of carbon coating, the well-crystalline grains, and the fast kinetic of Li transportation. Our cycling results are comparable to the previous report in context of electrode composite  $\text{LiFePO}_4$ @carbon for Li-ion batteries [7, 15, 33, 34].

Figure 8(a) demonstrates the typical charge-discharge profiles of LFP700 at rate capability performance. We observed a low middischarge potential difference (70 mV) until rate 2C while a drastic difference of 200 mV is obtained at 5C. The middischarge potential difference is depended on the electrode polarization that leads the fading capacity in high rate test. A significant capacity declined when the current density increased: from 170 mAh/g at C/10 to 160 mAh/g at C/5, 151 mAh/g at C/2, 142 mAh/g at 1C, 125 mAh/g at 2C, and 105 mAh/g at 5C. The performance at high rate would be further improved by forming the composite electrodes between active material and high-conductive carbonaceous-like CNTs or graphene. Our recent report showed that the additional CNTs in LFP's electrodes could benefit the long-term performance upon 200 cycles with 200 mAh/g at rate C/10 and a remarkable capacity of 120 mAh/g at rate 10C [35].

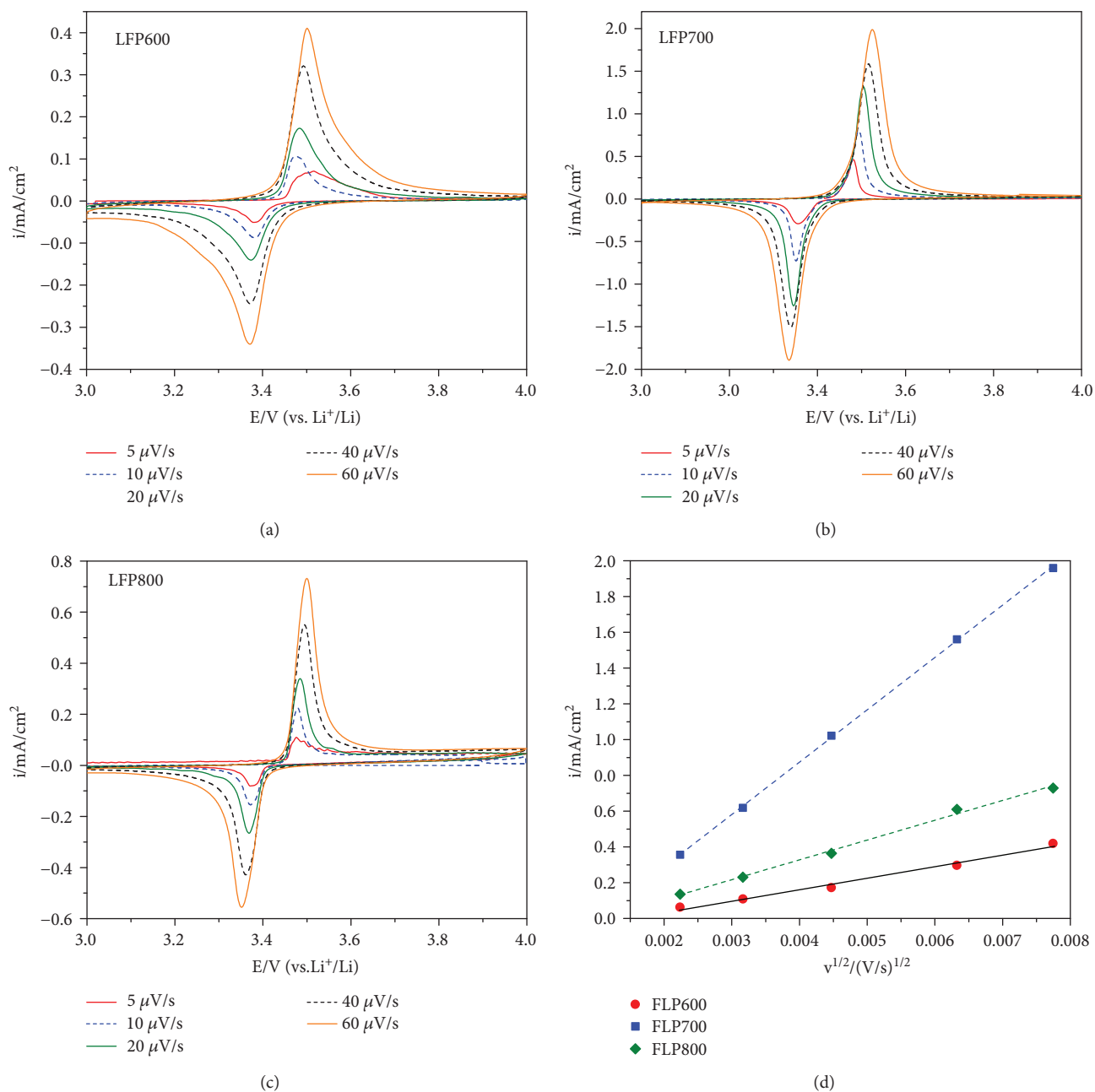


FIGURE 6: CV curves of (a) LFP600, (b) LFP700, and (c) LFP800 in scan rate 5–60  $\mu\text{V}/\text{s}$  and (d)  $i_{pc}$  as a function of the square root of the scan rate ( $v^{1/2}$ ) of electrodes LFP600, LFP700, and LFP800.

Figure 8(b) compares the rate capability performance of olivine samples; the current densities were applied from C/10 (17 mA/g) to 5C (85 mA/g) after performing 20 cycles at C/10 to activate the electrode's surface. The cycling stability was obtained at all rates; after switching back to lowest rate C/10, the capacities can be almost fully recovered. As mentioned in cycling test at monorate C/10, the cycling test of LFP700 at rate capability also pointed out the better performance than LFP600 and LFP800. Until rate 2C, LFP800 presented a low difference of capacities around 8 mAh/g but LFP600 presented a large difference of capacities more than 30 mAh/g. For example, at rate 1C (170 mAh/g), the

capacities found out 104 mAh/g for LFP600, 141 mAh/g for LFP700, and 133 mAh/g for LFP800. At the highest rate 5C (85 mAh/g), the capacities reached 72 mAh/g for LFP600, 105 mAh/g for LFP700, and 92 mAh/g for LFP800.

#### 4. Conclusion

In summary, our work prepared electrode composite  $\text{LiFePO}_4$ @carbon by hydrothermal. The temperature of calcination process affected the morphologies, the quality of carbon coating, and the electrochemical properties. The olivine LFP700 possessed a high graphitization of carbon

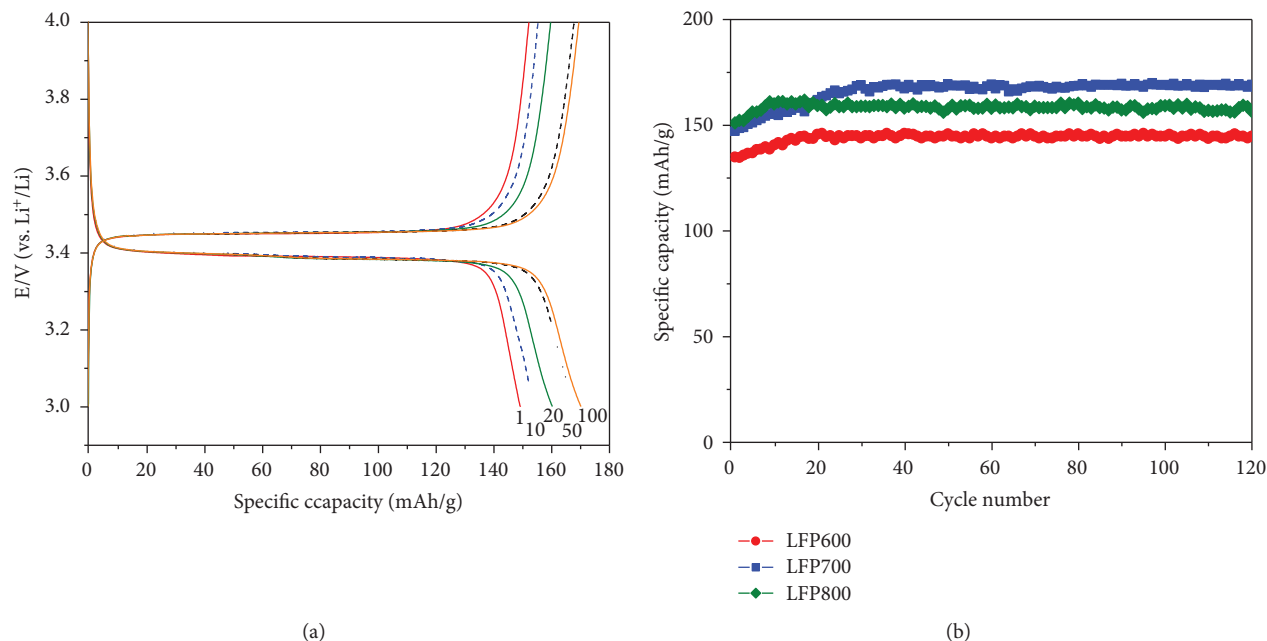


FIGURE 7: (a) Charge-discharge profile of LFP700 and (b) cycling stability of olivine samples at rate C/10.

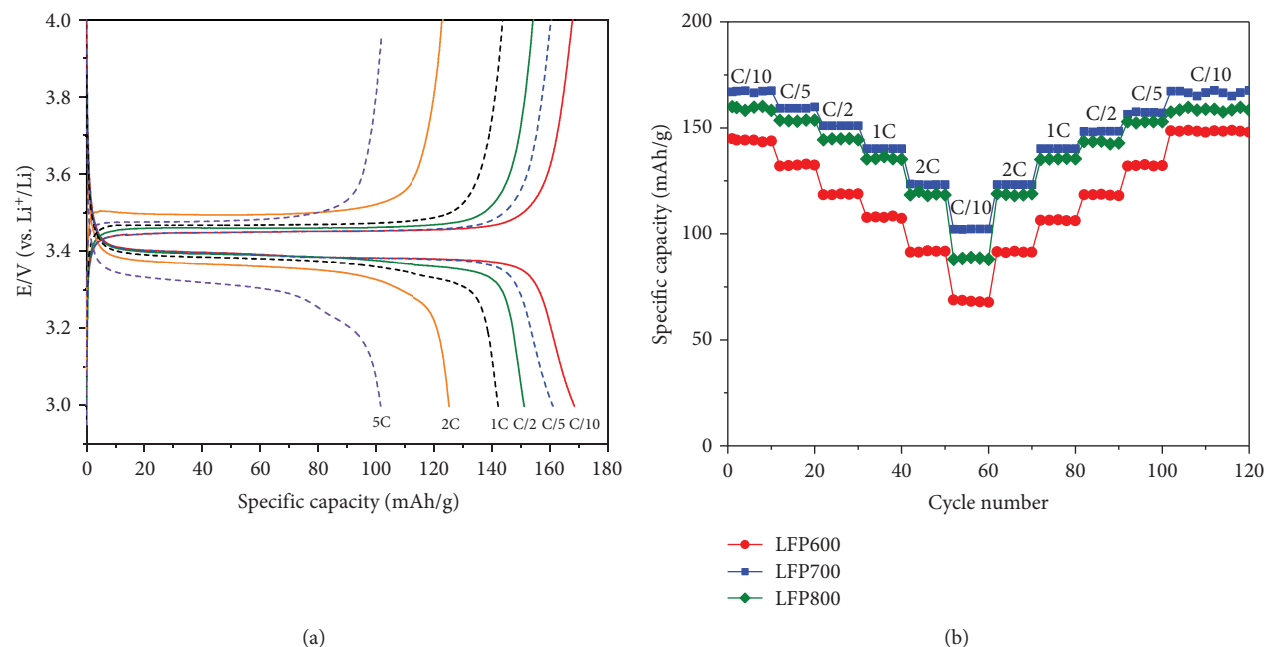


FIGURE 8: (a) Typical charge-discharge curves of LFP700 and (b) capacity stability at rate capability.

coating that lead a fast Li transportation; the Li diffusion of LFP700 was one order of magnitude larger than those of LFP600 and LFP800. The galvanostatic performances of three synthesized olivines showed an excellent cycling stability upon 120 cycles at monorate C/10 as well as rate capability from C/10 to 5C.

### Data Availability

The data used to support the findings of this study are included within the article.

### Conflicts of Interest

The authors declare that there is no conflict of interest regarding the publication of this paper.

### Acknowledgments

This research is funded by Viet Nam National University Ho Chi Minh (VNUHCM) under grant C2018-18-11 and Department of Science and Technology Ho Chi Minh City by contract 107/2016/HĐ-SKHCN.

## References

- [1] A. K. Padhi, K. S. Nanjundaswamy, and J. B. Goodenough, "Phospho-olivines as positive-electrode materials for rechargeable lithium batteries," *Journal of the Electrochemical Society*, vol. 144, no. 4, pp. 1188–1194, 1997.
- [2] M. S. Whittingham, Y. Song, S. Lutta, P. Y. Zavalij, and N. A. Chernova, "Some transition metal (oxy)phosphates and vanadium oxides for lithium batteries," *Journal of Materials Chemistry*, vol. 15, no. 33, p. 3362, 2005.
- [3] V. A. Streltsov, E. L. Belokoneva, V. G. Tsirelson, and N. K. Hansen, "Multipole analysis of the electron density in triphylite,  $\text{LiFePO}_4$ , using X-ray diffraction data," *Acta Crystallographica Section B*, vol. B49, no. 2, pp. 147–153, 1993.
- [4] S.-Y. Chung, J. T. Bloking, and Y.-M. Chiang, "Electronically conductive phospho-olivines as lithium storage electrodes," *Nature Materials*, vol. 1, no. 2, pp. 123–128, 2002.
- [5] Y.-N. Xu, S. Y. Chung, J. T. Bloking, Y. M. Chiang, and W. Y. Ching, "Electronic structure and electrical conductivity of undoped  $\text{LiFePO}_4$ ," *Electrochemical and Solid-State Letters*, vol. 7, no. 6, pp. A131–A134, 2004.
- [6] D. Y. W. Yu, C. Fietzek, W. Weydanz et al., "Study of  $\text{LiFePO}_4$  by cyclic voltammetry," *Journal of the Electrochemical Society*, vol. 154, no. 4, pp. A253–A257, 2007.
- [7] P. Axmann, C. Stinner, M. Wohlfahrt-Mehrens, A. Mauger, F. Gendron, and C. M. Julien, "Nonstoichiometric  $\text{LiFePO}_4$ : defects and related properties," *Chemistry of Materials*, vol. 21, no. 8, pp. 1636–1644, 2009.
- [8] K. Tang, X. Yu, J. Sun, H. Li, and X. Huang, "Kinetic analysis on  $\text{LiFePO}_4$  thin films by CV, GITT, and EIS," *Electrochimica Acta*, vol. 56, no. 13, pp. 4869–4875, 2011.
- [9] L. Castro, R. Dedryvère, M. El Khalifi et al., "The spin-polarized electronic structure of  $\text{LiFePO}_4$  and  $\text{FePO}_4$  evidenced by in-Lab XPS," *Journal of Physical Chemistry C*, vol. 114, no. 41, pp. 17995–18000, 2010.
- [10] L. Li, L. Wu, F. Wu et al., "Review—recent research progress in surface modification of  $\text{LiFePO}_4$  cathode materials," *Journal of the Electrochemical Society*, vol. 164, no. 9, pp. A2138–A2150, 2017.
- [11] A. Eftekhari, " $\text{LiFePO}_4/\text{C}$  nanocomposites for lithium-ion batteries," *Journal of Power Sources*, vol. 343, pp. 395–411, 2017.
- [12] R. Amin, J. Maier, P. Balaya, D. P. Chen, and C. T. Lin, "Ionic and electronic transport in single crystalline  $\text{LiFePO}_4$  grown by optical floating zone technique," *Solid State Ionics*, vol. 179, no. 27–32, pp. 1683–1687, 2008.
- [13] F. Brochu, A. Guerfi, J. Trottier et al., "Structure and electrochemistry of scaling nano  $\text{C-LiFePO}_4$  synthesized by hydrothermal route: complexing agent effect," *Journal of Power Sources*, vol. 214, pp. 1–6, 2012.
- [14] J. Chen, M. J. Vacchio, S. Wang, N. Chernova, P. Y. Zavalij, and M. S. Whittingham, "The hydrothermal synthesis and characterization of olivines and related compounds for electrochemical applications," *Solid State Ionics*, vol. 178, no. 31–32, pp. 1676–1693, 2008.
- [15] J. Lim, J. Gim, S.-W. Kang, S. Baek, H. Jeong, and J. Kim, "Synthesis of  $\text{LiFePO}_4$  nanoparticles and crystal formation mechanism during solvothermal reaction," *Journal of the Electrochemical Society*, vol. 159, no. 4, pp. A479–A484, 2012.
- [16] W. Jiang, M. Wu, F. Liu, J. Yang, and T. Feng, "Variation of carbon coatings on the electrochemical performance of  $\text{LiFePO}_4$  cathodes for lithium ionic batteries," *RSC Advances*, vol. 7, no. 70, pp. 44296–44302, 2017.
- [17] T. T. Zhan, W. F. Jiang, C. Li et al., "High performed composites of  $\text{LiFePO}_4/3\text{DG}/\text{C}$  based on  $\text{FePO}_4$  by hydrothermal method," *Electrochimica Acta*, vol. 246, pp. 322–328, 2017.
- [18] H. M. Rietveld, "A profile refinement method for nuclear and magnetic structures," *Journal of Applied Crystallography*, vol. 2, no. 2, pp. 65–71, 1969.
- [19] P. Coelho, *Topas Technical Reference Manual*, Bruker AXS, 2005.
- [20] B. J. Paul, S.-W. Kang, J. Gim et al., "Nucleation and growth controlled polyol synthesis of size-focused nanocrystalline  $\text{LiFePO}_4$  cathode for high performance Li-ion batteries," *Journal of the Electrochemical Society*, vol. 161, no. 9, pp. A1468–A1473, 2014.
- [21] M. M. Doeff, Y. Hu, F. McLarnon, and R. Kostecki, "Effect of surface carbon structure on the electrochemical performance of  $\text{LiFePO}_4$ ," *Electrochemical and Solid-State Letters*, vol. 6, no. 10, pp. A207–A209, 2003.
- [22] J. Hong, C. Wang, N. J. Dudney, and M. J. Lance, "Characterization and performance of  $\text{LiFePO}_4$  thin-film cathodes prepared with radio-frequency magnetron-sputter deposition," *Journal of the Electrochemical Society*, vol. 154, no. 8, pp. A805–A809, 2007.
- [23] R. Dedryvère, M. Maccario, L. Croguennec, F. Le Cras, C. Delmas, and D. Gonbeau, "X-ray photoelectron spectroscopy investigations of carbon-coated  $\text{Li}_x\text{FePO}_4$  materials," *Chemistry of Materials*, vol. 20, no. 22, pp. 7164–7170, 2008.
- [24] V. Mathew, J. Gim, E. Kim et al., "A rapid polyol combustion strategy towards scalable synthesis of nanostructured  $\text{LiFePO}_4/\text{C}$  cathodes for Li-ion batteries," *Journal of Solid State Electrochemistry*, vol. 18, no. 6, pp. 1557–1567, 2014.
- [25] N. Zhang, L. Lin, and Z. Xu, "Effect of synthesis temperature, time, and carbon content on the properties and lithium-ion diffusion of  $\text{LiFePO}_4/\text{C}$  composites," *Journal of Solid State Electrochemistry*, vol. 18, no. 9, pp. 2401–2410, 2014.
- [26] R.-R. Zhao, B.-Y. Lan, H.-Y. Chen, and G.-Z. Ma, "Hydrothermal synthesis and properties of manganese-doped  $\text{LiFePO}_4$ ," *Ionics*, vol. 18, no. 9, pp. 873–879, 2012.
- [27] Y.-H. Rho, L. F. Nazar, L. Perry, and D. Ryan, "Surface chemistry of  $\text{LiFePO}_4$  studied by Mössbauer and X-ray photoelectron spectroscopy and its effect on electrochemical properties," *Journal of the Electrochemical Society*, vol. 154, no. 4, p. A283, 2007.
- [28] H. Liu, H. Yang, and J. Li, "A novel method for preparing  $\text{LiFePO}_4$  nanorods as a cathode material for lithium-ion power batteries," *Electrochimica Acta*, vol. 55, no. 5, pp. 1626–1629, 2010.
- [29] M. Nocuñ, "Structural studies of phosphate glasses with high ionic conductivity," *Journal of Non-Crystalline Solids*, vol. 333, no. 1, pp. 90–94, 2004.
- [30] C. V. Ramana, A. Ait-Salah, S. Utsunomiya et al., "Spectroscopic and chemical imaging analysis of lithium iron triphosphate," *Journal of Physical Chemistry C*, vol. 111, no. 2, pp. 1049–1054, 2007.
- [31] I. Belharouak, C. Johnson, and K. Amine, "Synthesis and electrochemical analysis of vapor-deposited carbon-coated  $\text{LiFePO}_4$ ," *Electrochemistry Communications*, vol. 7, no. 10, pp. 983–988, 2005.
- [32] A. Varzi, D. Bresser, J. von Zamory, F. Müller, and S. Passerini, " $\text{ZnFe}_2\text{O}_4\text{-C}/\text{LiFePO}_4\text{-CNT}$ : a novel high-power lithium-ion

- battery with excellent cycling performance,” *Advanced Energy Materials*, vol. 4, no. 10, article 1400054, 2014.
- [33] W.-J. Zhang, “Structure and performance of  $\text{LiFePO}_4$  cathode materials: a review,” *Journal of Power Sources*, vol. 196, no. 6, pp. 2962–2970, 2011.
- [34] X. Ma, G. Chen, Q. Liu, G. Zeng, and T. Wu, “Synthesis of  $\text{LiFePO}_4$ /graphene nanocomposite and its electrochemical properties as cathode material for Li-ion batteries,” *Journal of Nanomaterials*, vol. 2015, Article ID 301731, 6 pages, 2015.
- [35] L. T. N. Huynh, T. T. D. Tran, H. H. A. Nguyen et al., “Carbon-coated  $\text{LiFePO}_4$ -carbon nanotube electrodes for high-rate Li-ion battery,” *Journal of Solid State Electrochemistry*, vol. 22, no. 7, pp. 2247–2254, 2018.

## Research Article

# Decreased Surface Photovoltage of ZnO Photoanode Films via Optimal Annealing Temperature for Enhanced Photoelectrochemical Performance

Yichong Liu,<sup>1</sup> Bohuai Xiao,<sup>1</sup> Haijian Chen,<sup>1</sup> Yunchuan Li <sup>1</sup>, and Shuai Chang <sup>1,2</sup>

<sup>1</sup>The State Key Laboratory of Refractories and Metallurgy, Wuhan University of Science and Technology, Wuhan 430081, China

<sup>2</sup>Institute of Advanced Materials and Nanotechnology, Wuhan University of Science and Technology, Wuhan 430081, China

Correspondence should be addressed to Yunchuan Li; 844290658@qq.com and Shuai Chang; schang23@wust.edu.cn

Received 9 May 2018; Revised 9 August 2018; Accepted 2 October 2018; Published 27 January 2019

Guest Editor: Mohammed H. Abdul Jabbar

Copyright © 2019 Yichong Liu et al. This is an open access article distributed under the Creative Commons Attribution License, which permits unrestricted use, distribution, and reproduction in any medium, provided the original work is properly cited.

The electronic structure of semiconducting materials at the electrode/electrolyte interface plays a vital role in the process of photoelectrochemical (PEC) water splitting. In this work, we could reliably tune the surface defect density of ZnO films through changing the annealing temperature, thereby optimizing the PEC performance. The surface photovoltage (SPV) of ZnO films could be obtained by Kelvin probe force microscopy and compared to insightfully understand the effect of the annealing temperature on the performance of the electrode in PEC water splitting. The minimum SPV annealed at 450°C indicated low surface defect density, eventually resulting in an enhanced photoelectrochemical performance. The applied bias photo-current efficiency of ZnO films annealed at 450°C reached 0.237%, about 7.4 times that of unannealed ZnO photoanode. This work provides an effective method for the rational fabrication of efficient photoelectrodes for the realization of high-performance photoelectrochemical water splitting.

## 1. Introduction

Hydrogen generated from photoelectrochemical (PEC) water splitting has shown significant potential for solar energy conversion to meet the steady increase of energy demands [1]. In principle, the efficiency of PEC water splitting mainly depends on the following factors: (1) light absorption, (2) photogenerated charge separation and transport, and (3) surface chemical reaction [2, 3]. For a PEC system, the light absorption is determined by the bandgap of photoelectrodes, and the driving force of charge separation originates from the electric field in the depletion region at the photoelectrode/electrolyte interface. Thus, the interfacial electronic structure of semiconducting materials plays a vital role in the process of photoelectrochemical water splitting [4]. Therefore, the understanding of the change in electronic structure of semiconductor materials is favourable for the rational design of efficient photoanode. Thus, the key in a PEC system is the selection of high-performance photoelectrodes.

Although narrow-bandgap semiconductors, such as silicon and III–IV group of composites, show high light harvesting efficiency, the surface corrosion hinders their lifetime even in a sacrificial electrolyte [5, 6]. Among various N-type metal oxides [7–12], zinc oxide (ZnO) has been extensively investigated as photoanode for photoelectrochemical water splitting ascribed to its low cost, excellent electron mobility ( $115\text{--}155\text{ cm}^2\cdot\text{V}^{-1}\cdot\text{s}^{-1}$ ), and appropriate conduction/valence band edges for water splitting [13–17]. As a postprocessing method, annealing has been proved to be a valid method to change the interfacial electronic structure, resulting in a significant impact on the properties of ZnO nanomaterials [18, 19]. Wu et al. [20] demonstrated that the work function of ZnO nanorod arrays exhibited a gradual increase after a decrease with the increase in the annealing temperature. Wang et al. [21] found that the improved PEC performance of ZnO nanowires (NWs) was mainly attributed to the larger depleted width in ZnO NWs caused by annealing. Further, the carrier concentration of ZnO films by electron beam

annealing is about 2~3 orders of magnitude higher than that of unannealed ZnO thin films [22]. However, there is still a lack of in-depth understanding about the change in interfacial electronic structure for the enhanced PEC performance caused by different annealing temperatures.

Previously, we have constructed various photoanodes based on ZnO nanomaterials. And surface modification materials, doping, and structure optimization were sequentially taken into combination to form ZnO-based composite nanostructures, in which each component worked synergistically to compensate each other [13–16]. In conclusion, there are some significant differences between previous works and current work as for the following aspects. Previous works put emphasis on the realization of highly efficient photoanode based on ZnO nanomaterials to raise the light harvesting efficiency, reduce the charge recombination, and accelerate the surface reaction. However, multistep and complex processes are always introduced into these strategies. Thus, this work adopts a one-step process and posttreatment to tune the PEC performance, and we mainly focused on the change of interfacial electronic structure by the KPFM. The surface photovoltage (SPV) of ZnO films under different annealing temperatures was obtained through calculating the difference between the surface potentials under UV illumination and in the dark measured by KPFM. After annealing at 450°C, the minimum SPV of ZnO films indicated low defect density, which contributed to the improved photocurrent density and enhanced photoelectrochemical performance. This simple and novel method also allows us to have more fundamental understanding of the effects of ZnO itself on the PEC performance.

## 2. Materials and Methods

Commercially available indium tin oxide- (ITO-) coated glass ( $2 \times 2 \text{ cm}^2$ ) was used as the substrate. ITO substrates were sequentially sonicated in acetone, isopropanol, ethanol, and deionized water, each for 10 minutes, and then dried with nitrogen gas flow. The ZnO film was deposited on the ITO substrate via the radiofrequency (RF) magnetron sputtering method as reported [23]. After deposition, ZnO films were annealed in a vacuum drying oven at 350°C, 450°C, and 550°C for 2 hours, respectively. The corresponding samples were named ZnO-350, ZnO-450, and ZnO-550.

The morphology and crystalline structure of the ZnO film were characterized by field-emission scanning electron microscopy (FESEM, FEI QUANTA 3D) and X-ray diffraction (XRD) (Rigaku DMAX-RB with Cu K $\alpha$  radiation), respectively. The light absorption and photoluminescence spectrum were recorded by a UV-vis spectrophotometer (UV-2500, Shimadzu, Japan) and a continuous He-Cd (325 nm) laser as an excitation source, respectively. KPFM measurements were tested under a commercially available atomic force microscope (ICON, Bruker Inc.) in lift mode at about 25°C. PtIr-coated silicon cantilevers (Olympus, OSCM-PIT) with a nominal resonance frequency of 75 kHz were used as conductive probes.

A copper wire was secured on the exposed conductive parts of ITO with a silver conducting paint, and the rest of

the substrate was subsequently encapsulated with epoxy resin except the active working area, confirming the successful preparation of the photoanode. A three-electrode system used for various electrochemical measurements on an electrochemical workstation (Solartron SI 1287/SI 1260) consists of a photoanode as the working electrode, a coiled Pt wire as the counter electrode, and an Ag/AgCl reference electrode. Neutral aqueous Na<sub>2</sub>SO<sub>4</sub> solution (0.5 M) was chosen as the electrolyte. The simulated sunlight provided by a solar simulator (Oriel, 91159A) is incident from the front of the photoanode, and the intensity of the simulated sunlight was 60 mW/cm<sup>2</sup> measured by a Si diode (Newport). The applied bias photo-to-current efficiency ( $\eta_{\text{ABPE}}$ ) was calculated from  $J_{\text{ph}} - V$  curves, assuming 100% faradaic efficiency through the following equation [24]:

$$\eta_{\text{ABPE}} = \frac{I(1.23 - V_{\text{app}})}{P_{\text{light}}}, \quad (1)$$

where  $V_{\text{app}}$  is the applied external potential versus the reversible hydrogen electrode (RHE).  $I$  is the externally measured current density at  $V_{\text{app}}$ .  $P_{\text{light}}$  is the power density of the incident light. The potentials were measured versus the Ag/AgCl reference electrode and converted to the RHE scale using the Nernst function:

$$E_{\text{RHE}} = E_{\text{Ag/AgCl}} + E_{\text{Ag/AgCl}}^{\circ} + 0.059\text{pH}, \quad (2)$$

where  $E_{\text{RHE}}$  is the converted potential versus RHE.  $E_{\text{Ag/AgCl}}$  is the external potential measured against the Ag/AgCl reference electrode.  $E_{\text{Ag/AgCl}}^{\circ}$  is the standard electrode potential of the Ag/AgCl reference electrode (0.1976 V versus RHE at 25°C).

## 3. Results and Discussion

Figure 1(a) exhibits a representative cross-sectional scanning electron microscope (SEM) image of the ZnO film on the ITO prior to annealing, indicating that the film is composed of multiple ZnO columnar grains. The grain size calculated from the top view image in the inset of Figure 1(a) is in the range of 30–100 nm. Furthermore, the corresponding XRD pattern is used to characterize the structure of an unannealed ZnO film. As shown in Figure 1(b), XRD of ZnO films exhibits that all diffraction peaks can be corresponded to the planes of highly crystalline ZnO (JCPDS file no. 36-1451). And the apparent diffraction peak of (002) at 34.4° demonstrates that the ZnO film is grown preferentially along *c*-axis direction on the ITO [25].

The schematic illustration of the ZnO film on the ITO upon the bandgap illumination is shown in Figure 2(a). Under simulated sunlight, electrons and holes are generated in the conduction band ( $E_{\text{CB}}$ ) and valence band ( $E_{\text{VB}}$ ), respectively. The photogenerated electrons transfer to the Pt electrode for the hydrogen evolution in the PEC cell device. On the other hand, the photogenerated holes in  $E_{\text{VB}}$

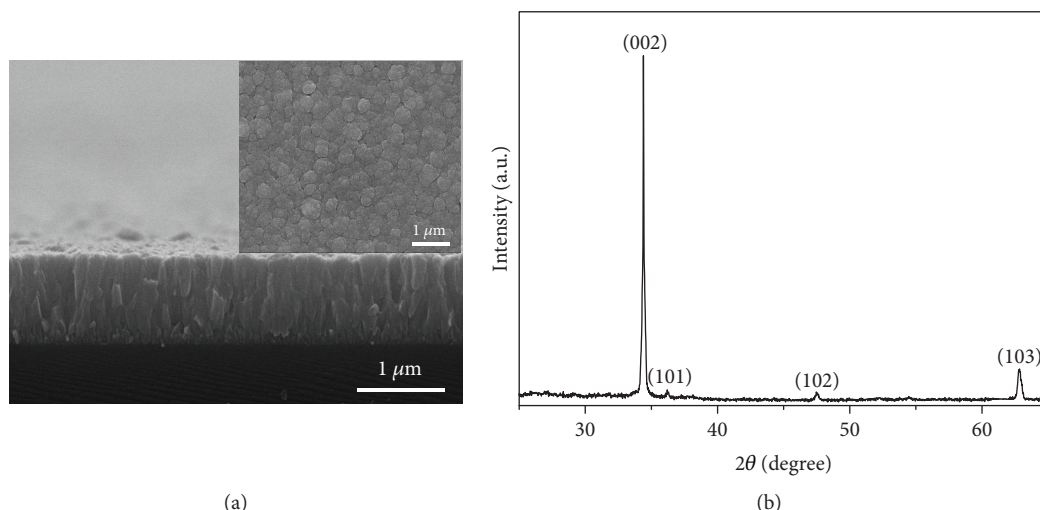


FIGURE 1: (a) Cross-sectional SEM image of the RF-sputtered ZnO film on the ITO prior to annealing. The inset is the top view image. (b) The corresponding XRD pattern of the deposited film.

of ZnO participate in the oxidation evolution to finish the whole process.

In order to study the photoelectrochemical properties of the prepared photoanodes, the PEC measurements of various as-prepared photoanodes were characterized by linear sweep voltammetry (LSV) curves in the dark and under simulated sunlight illumination. A very small dark photocurrent in the scale of  $10^{-3}$  mA/cm<sup>2</sup> is shown in Figure 2(b), implying that the observed photocurrent is related to the photogenerated charge carriers. Under illumination, a significant increase in photocurrent density was observed, and the ZnO-450 photoanode exhibited the highest photocurrent density in the whole investigated potential range, ascribed to the lowest density of trap states at the surface among those of other samples. The photocurrent density of unannealed ZnO, ZnO-350, ZnO-450, and ZnO-550 reached 0.19, 0.559, 0.586, and 0.457 mA/cm<sup>2</sup> at 1 V vs. Ag/AgCl, respectively. According to (1) and (2), the ABPE of different photoanodes was calculated from the LSV curve. As shown in Figure 3(c), the ZnO-450 photoanode exhibited the highest efficiency of 0.237%, about 7.4 times that of the unannealed ZnO photoanode (0.032%).

To attain a deep understanding of the PEC performance, electrochemical impedance spectroscopy (EIS) was used to explore the electrochemical behavior at the photoelectrode/electrolyte interface at 0 V vs. Ag/AgCl under white light illumination. Figure 2(d) reveals the typical EIS Nyquist plots for four different photoanodes, and the equivalent circuit in Figure 2(d) was used to fit the Nyquist plots, in which  $R_s$ ,  $R_{ct}$ , and CPE represented series resistance, interfacial charge-transfer resistance at the photoelectrode/electrolyte interface, and constant phase angle element, respectively. The smaller size of the arc in an EIS Nyquist plot indicated a faster charge transfer and less recombination at the photoelectrode/electrolyte interface. The results obtained by fitting revealed that the corresponding  $R_{ct}$  of unannealed ZnO, ZnO-350, ZnO-450, and ZnO-550 was 5.18, 2.6, 2.18, and

3.98 kΩ, respectively. The smallest  $R_{ct}$  of the ZnO-450 photoanode could result in the highest photocurrent density and ABPE consistent with the LSV and ABPE curve shown in Figures 2(b) and 2(c).

To explore the photocurrent improvement, light absorption properties of ZnO films annealed under different temperatures were investigated by the UV-vis absorbance spectra. As shown in Figure 4(a), all the samples showed similar optical absorption in the UV region. As the annealing temperature increases, the optical absorption edges showed a slight red shift. Further, the optical bandgap of different samples was estimated based on the following equation [26]:

$$(\alpha h\nu)^n = A(h\nu - E_g), \quad (3)$$

where  $\alpha$  is the absorption coefficient of the material,  $h\nu$  is the energy of photon,  $n$  represents the index which depends on the electronic transition of the semiconductor (for direct bandgap semiconductor ZnO,  $n = 2$ ), and  $A$  is the proportionality constant related to the material. Therefore, the bandgap energy could be obtained from the intercept of the tangent line in the plot of  $(\alpha h\nu)^2$  versus energy. As shown in Figure 4(b), the optical bandgap decreased from 3.11 eV to 3.09 eV as the annealing temperature increased. Thus, the negligible deviation ( $\sim 0.02$  eV) meant that the light absorption is not the dominating reason for the improvement of the photocurrent.

To reveal the effect of annealing temperature on the charge separation, the room temperature photoluminescence (PL) spectra were investigated to study the change of the surface defect density of ZnO films annealed at different temperatures. As shown in Figure 4(c), the samples showed two main peaks: the sharp one around 390 nm was ascribed to the near-band-edge (NBE) emission and the other broad one was in the range of 440–660 nm corresponding to the intrinsic defect-related energy [27, 28]. In Figure 4(d), a red

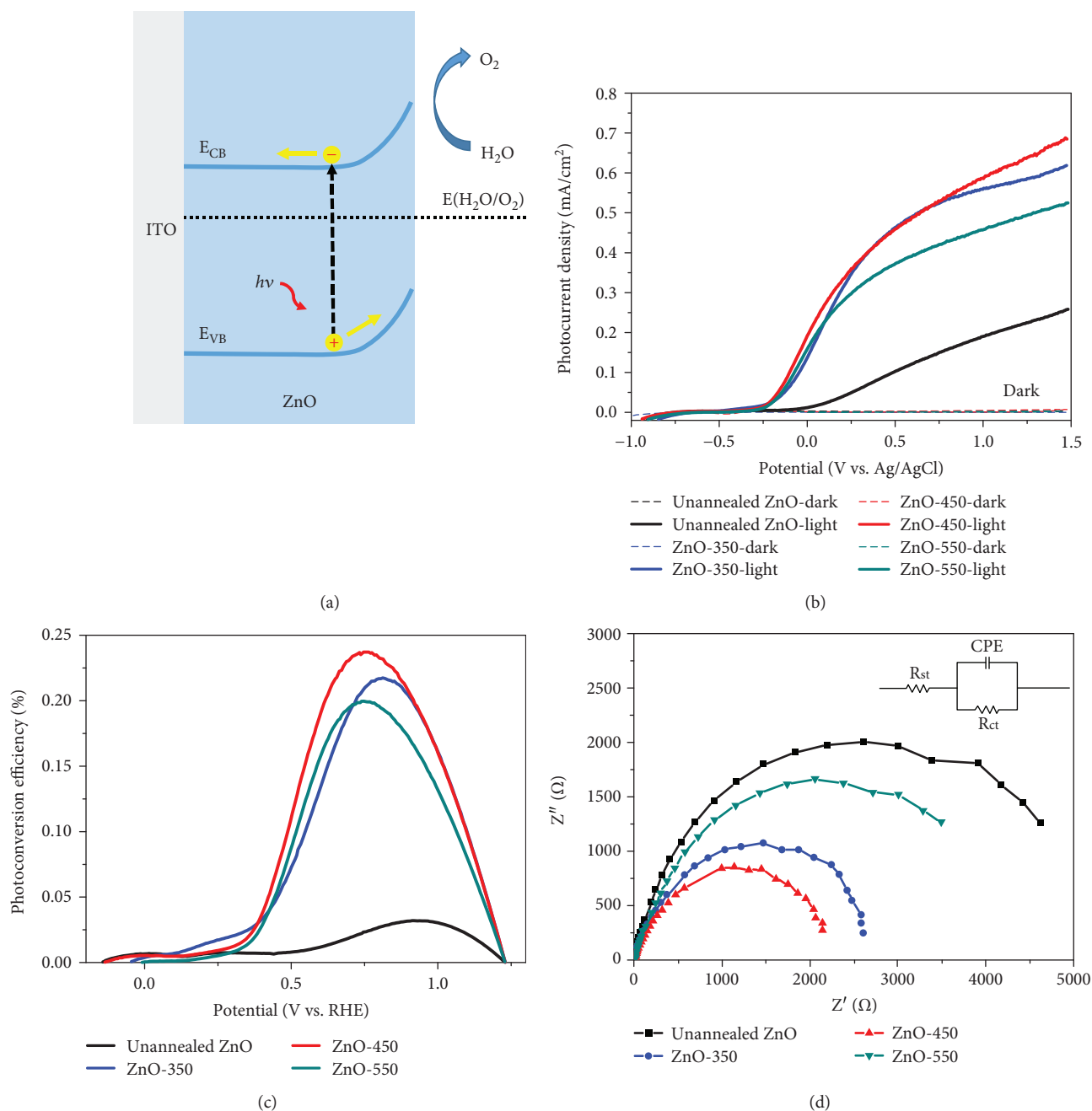


FIGURE 2: (a) Cross-sectional schematic and energy band alignment of the ZnO photoanode for water splitting. Comparisons of PEC properties of four different photoanodes: unannealed ZnO (black), ZnO-350 (blue), ZnO-450 (red), and ZnO-550 (cyan). (b) Linear sweep voltammetry measurements in the dark and under illumination, (c) the corresponding applied bias photo-to-current efficiency as a function of applied potential vs. RHE, and (d) Nyquist plots measured at an applied potential of 0 V vs. Ag/AgCl under illumination. The inset is the equivalent circuit used to fit the Nyquist plots.

shift of NBE emission peak was observed with the increase in annealing temperature, which is consistent with the change of optical bandgap in Figure 4(b). When the annealing temperature was no more than 450°C, the intensity of broad deep-level (DL) emission decreased ascribed to the improved crystalline quality after annealing. However, when the annealing temperature reached 550°C, the intensity of DL emission revealed a significant increase due to the increased probability of the radiative recombination which is

associated with the deep-level emission. Therefore, the low intensity of DL emission of ZnO-450 indicated reduced electron-hole recombination.

To further characterize the surface defect density of ZnO films annealed at different temperatures, Kelvin probe force microscopy (KPFM) was employed under dark and light conditions to measure the surface potential difference [29–31]. As shown in Figure S1 in Supplementary Materials, the contact potential difference ( $V_{CPD}$ ) between a sample and

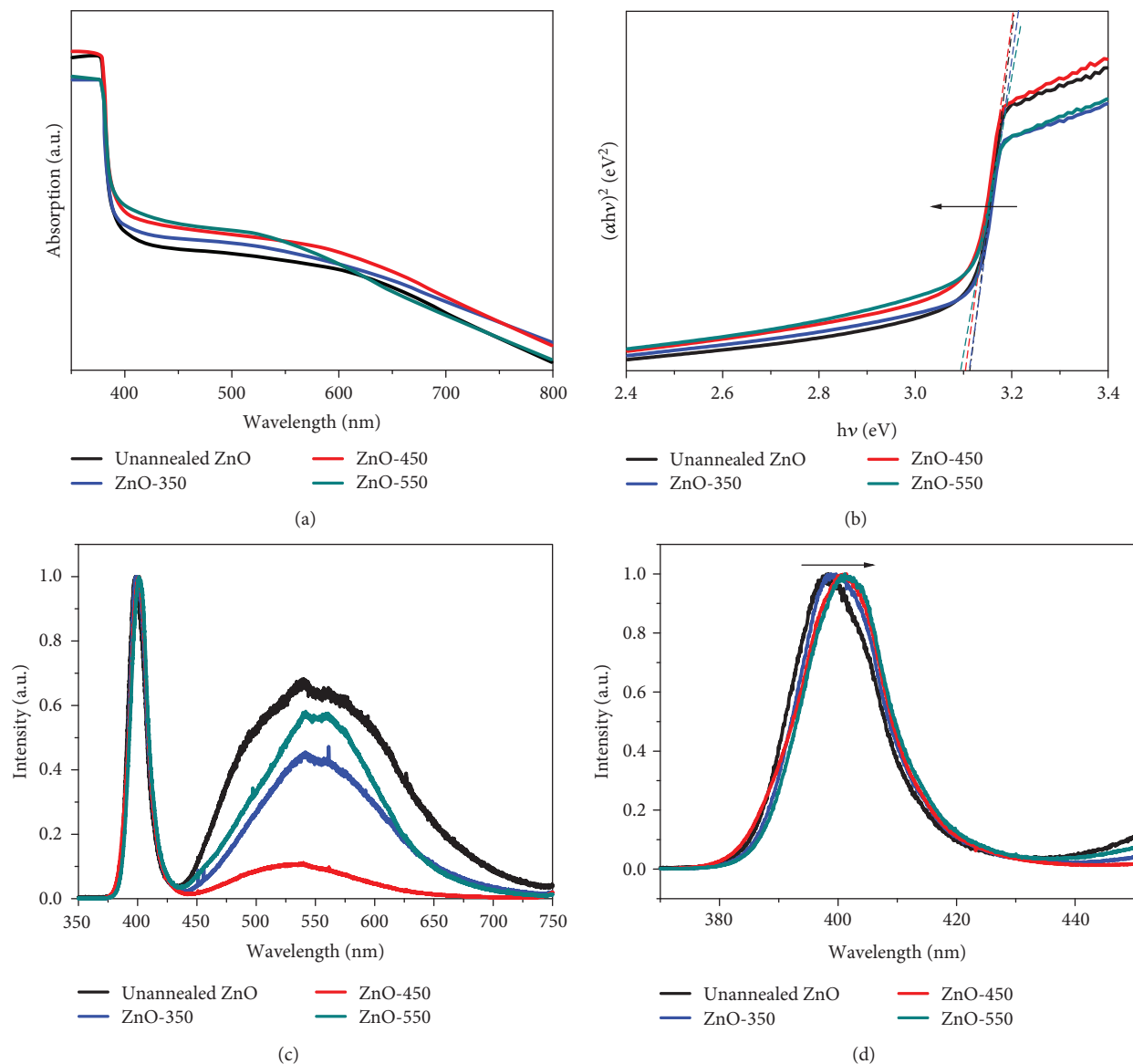


FIGURE 3: (a) UV-vis absorption spectra and (b) the corresponding  $(\alpha h\nu)^2$  vs.  $h\nu$  curves of unannealed ZnO, ZnO-350, ZnO-450, and ZnO-550. Photoluminescence (PL) spectra of unannealed ZnO, ZnO-350, ZnO-450, and ZnO-550: (c) 300~720 nm and (d) 370~450 nm.

a tip was acquired for different samples in the dark and under UV illumination, respectively, and the corresponding average  $V_{\text{CPD}}$  was statistically analysed as shown in Figures 3(a)–3(d). As shown in Figure 4(f), the difference in work function in the dark and under UV illumination is defined as the surface photovoltage (SPV), which could be acquired based on the following equations [4, 32, 33]:

$$V_{\text{CPD}} = \frac{\varphi_{\text{tip}} - \varphi_{\text{sample}}}{q}, \quad (4)$$

$$\begin{aligned} \text{SPV} &= \varphi_{\text{sample-dark}} - \varphi_{\text{sample-light}} \\ &= q(V_{\text{CPD-light}} - V_{\text{CPD-dark}}), \end{aligned} \quad (5)$$

where  $\varphi_{\text{tip}}$  and  $\varphi_{\text{sample}}$  are the work functions of the tip and sample, respectively, and  $q$  is the electronic charge.

Figure 4(e) exhibits the average  $V_{\text{CPD}}$  and SPV of different samples, and the SPV of unannealed ZnO, ZnO-350, ZnO-450, and ZnO-550 was 95.8 mV, 73.3 mV, 71.6 mV, and 89.9 mV, respectively. As the SPV was used to demonstrate the change of the band bending at the photoelectrode/electrolyte surface, the SPV could be used to indicate the density of surface states [30, 34]. Thus, the minimum SPV value of ZnO-450 suggested the low density of trap states at the surface, which was in agreement with the results of photoluminescence spectra in Figure 4(c) and contributed to the enhancement of the PEC performance.

## 4. Conclusions

In summary, the photoelectrochemical performances of ZnO films on the ITO substrate were investigated through the work function study at the electrode/electrolyte interface

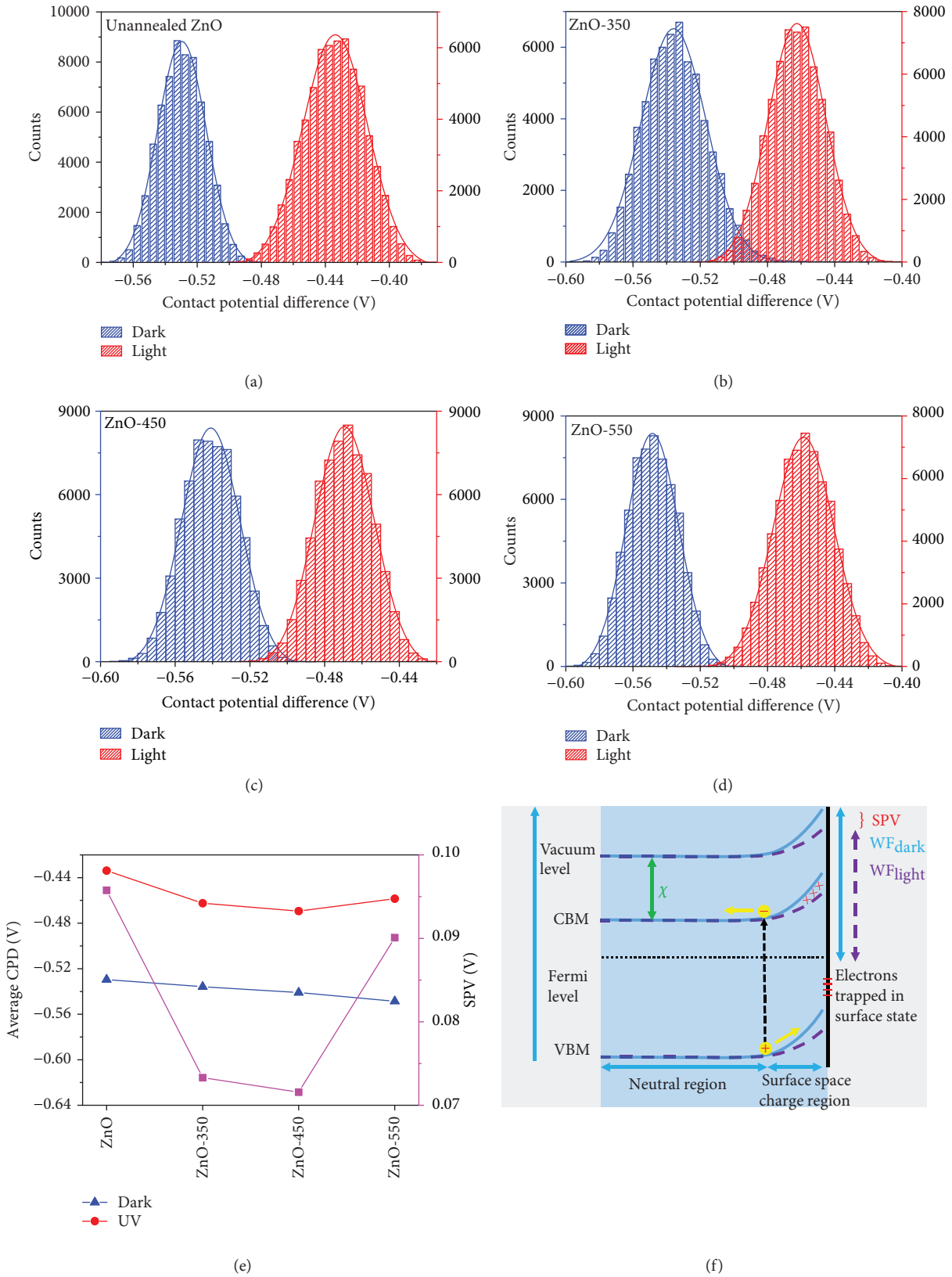


FIGURE 4: The statistical CPD acquired from KPFM mapping in the dark and under illumination: (a) unannealed ZnO, (b) ZnO-350, (c) ZnO-450, and (d) ZnO-550, respectively. (e) Average CPD in the dark and under illumination to the left scale and SPV of different samples to the right scale. (f) Schematic energy band diagram for the generation of surface photovoltage (SPV) at the ZnO surface (CBM: conduction band minimum; VBM: valence band maximum;  $\chi$ : electron affinity). The solid lines and the dotted lines represent the condition in the dark and light, respectively.

under different annealing temperatures. After annealing at 450°C, the minimum SPV of ZnO films indicated low defect density, which contributed to the improved photocurrent density and enhanced photoelectrochemical performance. The ZnO films annealed under 450°C exhibited an efficiency of 0.237%, which was much higher than that of unannealed ZnO films (0.032%). As a whole, this work provided a potential method to design innovative photoanodes for photoelectrochemical water splitting.

## Data Availability

The data used to support the findings of this study are available from the corresponding author upon request.

## Conflicts of Interest

There is no conflict of interest regarding the publication of this paper.

## Acknowledgments

The authors acknowledge the funding support from the Project of Thousand Youth Talents and National Natural Science Foundation of China (NNSFC) (21705122).

## Supplementary Materials

The images of contact potential differences in the dark and under UV illumination measured by KPFM are provided. (*Supplementary Materials*)

## References

- [1] S. K. Saraswat, D. D. Rodene, and R. B. Gupta, "Recent advancements in semiconductor materials for photoelectrochemical water splitting for hydrogen production using visible light," *Renewable & Sustainable Energy Reviews*, vol. 89, pp. 228–248, 2018.
- [2] Z. Chen, T. F. Jaramillo, T. G. Deutsch et al., "Accelerating materials development for photoelectrochemical hydrogen production: standards for methods, definitions, and reporting protocols," *Journal of Materials Research*, vol. 25, no. 01, pp. 3–16, 2011.
- [3] S. J. A. Moniz, S. A. Shevlin, D. J. Martin, Z. X. Guo, and J. Tang, "Visible-light driven heterojunction photocatalysts for water splitting – a critical review," *Energy & Environmental Science*, vol. 8, no. 3, pp. 731–759, 2015.
- [4] W.-H. Lin, J. J. Wu, M. M. C. Chou, Y. M. Chang, and M. Yoshimura, "Charge transfer in Au nanoparticle–nonpolar ZnO photocatalysts illustrated by surface-potential-derived three-dimensional band diagram," *The Journal of Physical Chemistry C*, vol. 118, no. 34, pp. 19814–19821, 2014.
- [5] M. G. Walter, E. L. Warren, J. R. McKone et al., "Solar water splitting cells," *Chemical Reviews*, vol. 110, no. 11, pp. 6446–6473, 2010.
- [6] A. Fujishima and K. Honda, "Electrochemical photolysis of water at a semiconductor electrode," *Nature*, vol. 238, no. 5358, pp. 37–38, 1972.
- [7] I. S. Cho, Z. Chen, A. J. Forman et al., "Branched TiO<sub>2</sub> nanorods for photoelectrochemical hydrogen production," *Nano Letters*, vol. 11, no. 11, pp. 4978–4984, 2011.
- [8] G. Wang, Y. Ling, D. A. Wheeler et al., "Facile synthesis of highly photoactive  $\alpha$ -Fe<sub>2</sub>O<sub>3</sub>-based films for water oxidation," *Nano Letters*, vol. 11, no. 8, pp. 3503–3509, 2011.
- [9] D. A. Wheeler, G. Wang, Y. Ling, Y. Li, and J. Z. Zhang, "Nanostructured hematite: synthesis, characterization, charge carrier dynamics, and photoelectrochemical properties," *Energy & Environmental Science*, vol. 5, no. 5, article 6682, 2012.
- [10] Y. J. Hwang, C. Hahn, B. Liu, and P. Yang, "Photoelectrochemical properties of TiO<sub>2</sub> nanowire arrays: a study of the dependence on length and atomic layer deposition coating," *ACS Nano*, vol. 6, no. 6, pp. 5060–5069, 2012.
- [11] H. Han, S. Kment, F. Karlicky et al., "Sb-doped SnO<sub>2</sub> nanorods underlayer effect to the  $\alpha$ -Fe<sub>2</sub>O<sub>3</sub> nanorods sheathed with TiO<sub>2</sub> for enhanced photoelectrochemical water splitting," *Small*, vol. 14, no. 19, article 1703860, 2018.
- [12] S. Wang, P. Chen, Y. Bai, J. H. Yun, G. Liu, and L. Wang, "New BiVO<sub>4</sub> dual photoanodes with enriched oxygen vacancies for efficient solar-driven water splitting," *Advanced Materials*, vol. 30, no. 20, article 1800486, 2018.
- [13] Y. Liu, Y. Gu, X. Yan et al., "Design of sandwich-structured ZnO/ZnS/Au photoanode for enhanced efficiency of photoelectrochemical water splitting," *Nano Research*, vol. 8, no. 9, pp. 2891–2900, 2015.
- [14] Y. Liu, X. Yan, Z. Kang et al., "Synergistic effect of surface plasmonic particles and surface passivation layer on ZnO nanorods array for improved photoelectrochemical water splitting," *Scientific Reports*, vol. 6, no. 1, article 29907, 2016.
- [15] Y. Liu, Z. Kang, H. Si et al., "Cactus-like hierarchical nanorod-nanosheet mixed dimensional photoanode for efficient and stable water splitting," *Nano Energy*, vol. 35, pp. 189–198, 2017.
- [16] Y. Liu, Z. Kang, S. Zhang et al., "Ferroelectric polarization-enhanced charge separation in a vanadium-doped ZnO photoelectrochemical system," *Inorganic Chemistry Frontiers*, vol. 5, no. 7, pp. 1533–1539, 2018.
- [17] C. Zhang, M. Shao, F. Ning et al., "Au nanoparticles sensitized ZnO nanorod@nanoplatelet core-shell arrays for enhanced photoelectrochemical water splitting," *Nano Energy*, vol. 12, pp. 231–239, 2015.
- [18] J. K. Cooper, Y. Ling, C. Longo, Y. Li, and J. Z. Zhang, "Effects of hydrogen treatment and air annealing on ultrafast charge carrier dynamics in ZnO nanowires under in situ photoelectrochemical conditions," *The Journal of Physical Chemistry C*, vol. 116, no. 33, pp. 17360–17368, 2012.
- [19] M. Baek, D. Kim, and K. Yong, "Simple but effective way to enhance photoelectrochemical solar-water-splitting performance of ZnO nanorod arrays: charge-trapping Zn(OH)<sub>2</sub> annihilation and oxygen vacancy generation by vacuum annealing," *ACS Applied Materials & Interfaces*, vol. 9, no. 3, pp. 2317–2325, 2017.
- [20] H. Wu, M. Xue, J. Ou, F. Wang, and W. Li, "Effect of annealing temperature on surface morphology and work function of ZnO nanorod arrays," *Journal of Alloys and Compounds*, vol. 565, pp. 85–89, 2013.
- [21] L. Wang, X. Gu, Y. Zhao, and Y. Qiang, "Enhanced photoelectrochemical properties of ZnO nanowire arrays annealed in air," *Journal of Materials Science: Materials in Electronics*, vol. 29, no. 5, pp. 4058–4064, 2018.

- [22] Y. Li, Y. Men, X. Kong, Z. Gao, L. Han, and X. Li, "Enhanced electrical properties of ZnO transparent conducting films prepared by electron beam annealing," *Applied Surface Science*, vol. 428, pp. 191–198, 2018.
- [23] P. Lin, X. Yan, Y. Liu, P. Li, S. Lu, and Y. Zhang, "A tunable ZnO/electrolyte heterojunction for a self-powered photodetector," *Physical Chemistry Chemical Physics*, vol. 16, no. 48, pp. 26697–26700, 2014.
- [24] J. W. Ager, M. R. Shaner, K. A. Walczak, I. D. Sharp, and S. Ardo, "Experimental demonstrations of spontaneous, solar-driven photoelectrochemical water splitting," *Energy & Environmental Science*, vol. 8, no. 10, pp. 2811–2824, 2015.
- [25] A. U. Pawar, C. W. Kim, M. J. Kang, and Y. S. Kang, "Crystal facet engineering of ZnO photoanode for the higher water splitting efficiency with proton transferable Nafion film," *Nano Energy*, vol. 20, pp. 156–167, 2016.
- [26] S. J. A. Moniz, J. Zhu, and J. Tang, "1D Co-Pi modified BiVO<sub>4</sub>/ZnO junction cascade for efficient photoelectrochemical water cleavage," *Advanced Energy Materials*, vol. 4, no. 10, p. 1301590, 2014.
- [27] X. Peng, J. Xu, H. Zang, B. Wang, and Z. Wang, "Structural and PL properties of Cu-doped ZnO films," *Journal of Luminescence*, vol. 128, no. 3, pp. 297–300, 2008.
- [28] P. T. Hsieh, Y. C. Chen, C. M. Wang, Y. Z. Tsai, and C. C. Hu, "Structural and photoluminescence characteristics of ZnO films by room temperature sputtering and rapid thermal annealing process," *Applied Physics A*, vol. 84, no. 3, pp. 345–349, 2006.
- [29] S. Lu, Q. Liao, J. Qi et al., "The enhanced performance of piezoelectric nanogenerator via suppressing screening effect with Au particles/ZnO nanoarrays Schottky junction," *Nano Research*, vol. 9, no. 2, pp. 372–379, 2016.
- [30] H. Si, Q. Liao, Z. Kang et al., "Deciphering the NH<sub>4</sub>PbI<sub>3</sub> intermediate phase for simultaneous improvement on nucleation and crystal growth of perovskite," *Advanced Functional Materials*, vol. 27, no. 30, article 1701804, 2017.
- [31] W. Zhang, S. Pathak, N. Sakai et al., "Enhanced optoelectronic quality of perovskite thin films with hypophosphorous acid for planar heterojunction solar cells," *Nature Communications*, vol. 6, no. 1, article 10030, 2015.
- [32] Y. Zhang, O. Pluchery, L. Caillard et al., "Sensing the charge state of single gold nanoparticles via work function measurements," *Nano Letters*, vol. 15, no. 1, pp. 51–55, 2015.
- [33] H. Yoo, C. Bae, Y. Yang et al., "Spatial charge separation in asymmetric structure of Au nanoparticle on TiO<sub>2</sub> nanotube by light-induced surface potential imaging," *Nano Letters*, vol. 14, no. 8, pp. 4413–4417, 2014.
- [34] S. M. Jain, Z. Qiu, L. Häggman et al., "Frustrated Lewis pair-mediated recrystallization of CH<sub>3</sub>NH<sub>3</sub>PbI<sub>3</sub> for improved optoelectronic quality and high voltage planar perovskite solar cells," *Energy & Environmental Science*, vol. 9, no. 12, pp. 3770–3782, 2016.

## Research Article

# Determination of Cyclability of Li/FeS<sub>2</sub> Batteries Based on Measurement of Coulombic Efficiency

Paul Maldonado Nogales, Hee-Youb Song, and Soon-Ki Jeong 

Department of Chemical Engineering, Soonchunhyang University, Asan, Chungcheongnam 31536, Republic of Korea

Correspondence should be addressed to Soon-Ki Jeong; hamin611@sch.ac.kr

Received 8 May 2018; Revised 29 July 2018; Accepted 19 August 2018; Published 20 September 2018

Academic Editor: Manab Kundu

Copyright © 2018 Paul Maldonado Nogales et al. This is an open access article distributed under the Creative Commons Attribution License, which permits unrestricted use, distribution, and reproduction in any medium, provided the original work is properly cited.

The electrochemical performance of negative electrodes based on different FeS<sub>2</sub> samples was investigated. The study demonstrated a correlation between the coulombic efficiency obtained over 60 cycles and the capacity loss rate evaluated over 15 cycles. The accuracy of the coulombic efficiency and capacity loss rate measurements was advantageous for predicting the aging behavior of half-cells over a short-term test. A suggested classification of the coulombic efficiency and verification via a numerical analysis were proposed to determine the fading rate of batteries during the galvanostatic test.

## 1. Introduction

Recently, lithium-ion batteries (LIBs) as a power source have been widely used in electrical devices, electric vehicles, energy storage systems, etc. In addition, there are a growing number of their applications that require excellent cyclability with high capacity. Hence, verifying the reliability of LIBs has become an important issue in recent years.

One of the most impressive studies on aging in LIBs tracks cells during cycling and storage for up to two years to quantitatively measure the lifetime of the battery based on electrode composition [1]. However, the evaluation of the cycle performance over a long time can be problematic if it takes days or months. Therefore, new techniques are needed for the effective aging evaluation of LIBs in a short period of time [2, 3].

The evaluation of the coulombic efficiency (CE) can be used to identify parameters that affect the normal functioning of the battery such as parasitic reactions between electrodes and electrolytes observed during discharge-charge cycling. Choi et al. [4] reported an FeS<sub>2</sub> cathode deficiency under different organic electrolytes. Their research includes calculations of the specific capacity and capacity loss rate. This kind of evaluation draws attention to special features that make it possible to determine the relation between accurate CE and capacity loss rate as a method of system

optimization, and the results can be used to rank cells according to their life expectancy without the need to use tests that take long to perform [5].

This paper presents a method that utilizes the CE and capacity loss rate to determine the cyclability with a short-term test. Firstly, we investigated the CE based on the charge-discharge cycle in a normal operating process during 60 cycles. Then, to determine the aging during the discharge-charge cycle, the capacity loss rates were investigated with different particle sizes of the FeS<sub>2</sub> electrodes. A simple comparison of CE with the capacity loss rate can be used to determine the effectiveness of the method and to validate the results using a short-term test.

## 2. Materials and Methods

**2.1. Preparation of FeS<sub>2</sub> Samples.** FeS<sub>2</sub> (99.9%, VITZRO MIL-TECH) samples were mechanically milled using a planetary ball mill (PBM) (PULVERISETTE, Fritsch) for 3 hours (3 h PBM), 6 hours (6 h PBM), and 10 hours (10 h PBM) and milled using a single ball mill (SBM) for 72 hours (72 h SBM). The working electrodes were fabricated by mixing FeS<sub>2</sub> as an active material, carbon black as a conductive additive, and polyvinylidene fluoride (PVDF) as a binder in a 60:20:20 weight ratio, respectively. The prepared slurry

was cast on a copper foil with a doctor blade and dried at 120°C in a vacuum oven for 12 h.

**2.2. Material Characterization.** The particle size distributions (PSDs) were analyzed using a particle size analyzer (Nano-Plus-1, Particulate Systems). Structural analysis of FeS<sub>2</sub> was carried out by employing X-ray diffraction (XRD), using a diffractometer (D/max-2200/PC, Rigaku Co.) equipped with a Cu K $\alpha$  source (40 kV, 40 mA), and the morphologies of the samples were studied using scanning electron microscopy (SEM) (SNE-3000M, SEC Co.).

**2.3. Electrochemical Measurements.** The electrochemical analysis was performed in a 2032-type coin cell. FeS<sub>2</sub> was used as a working electrode, and lithium foil was used as the reference electrode. The electrolyte solution was 1 mol dm<sup>-3</sup> LiClO<sub>4</sub> dissolved in a 1 : 1 (v/v) mixture of ethylene carbonate and dimethyl carbonate (battery grade, Enchem Co.). Galvanostatic measurements were performed using a battery test system (WBCS3000, WonATech Co.) between 1 and 2.8 V at constant currents of 89.2 and 892 mA g<sup>-1</sup>. All the potentials were referenced against Li/Li<sup>+</sup>.

**2.4. Measurement of Coulombic Efficiency (CE) and Capacity Loss Rate.** For a Li/FeS<sub>2</sub> half-cell, the “discharge” corresponds to the lithiation of FeS<sub>2</sub>. Based on the cycling data, the CE is measured as the ratio of the capacity of the charge Q<sub>c</sub> immediately following the previous discharge Q<sub>d</sub> [6]. The CE value is obtained using the formula CE = Q<sub>c</sub>/Q<sub>d</sub>, and changes over the number of cycles are evaluated. It is expected that CE < 1.0. The measurements obtained from all the tests performed on the samples were used to evaluate the capacity loss rate as the average of the percentage ratio of every discharge capacity and the previous capacity between the 10th and 60th cycle.

### 3. Results and Discussion

**3.1. Physical and Structural Characterization.** The XRD patterns and SEM images of the pristine, 72 h SBM, 3 h PBM, 6 h PBM, and 10 h PBM samples are shown in Figure 1. All the diffraction peaks are identical and coincide with the pattern of FeS<sub>2</sub> (PDF card no. 42-1340) in a simple cubic structure Pa3 space. Additionally, as shown in Figure 1, for the 3 h PBM, 6 h PBM, and 10 h PBM samples, the width of the peaks tended to be broader and shorter, a behavior that is not exhibited by the 72 h SBM. From another standpoint, FeS<sub>2</sub> particles are in shape of irregular fragments, not well identified by size. Thus, SEM images were not considered due to the fact that it cannot offer a quantitative description of particle size; instead, the inclusion of PSD analysis has more valuable information about particle dimension in Figure 2.

In order to obtain samples with different physical characteristics, five FeS<sub>2</sub> samples were selected to be subjected to a ball milling process before testing, because it was presumed that the reduction in particle sizes is beneficial for lithium-ion storage [7] and improves the performance of the Li/FeS<sub>2</sub> half-cell [8]. As shown in Table 1, the PSDs of milled FeS<sub>2</sub> (from Figure 2) were distributed in two regions clearly

divided according to the size and percentage in the sample; for the pristine, 72 h SBM, 3 h PBM, 6 h PBM, and 10 h PBM samples, the results obtained in the region with the highest percentage (greater than 50%) are in the range of 30–100, 15.6–50.0, 0.1–1.1, 26.1–73.7, and 0.1–0.8  $\mu$ m, respectively. Hence, the results indicate that as the ball milling time increases, the particle size decreases, but the smaller the particle size, the greater the agglomeration [7]. This behavior is exhibited by the 72 h SBM, 6 h PBM, and 10 h PBM samples with a distribution of 15.6–50.0, 26.1–73.7, and 7.0–25  $\mu$ m, respectively: the particle size was higher than that of the 3 h PBM sample under the same process conditions.

**3.2. Verification of FeS<sub>2</sub> Charge and Discharge Mechanism.** First, we verified the reduction and oxidation inside the cell. The effect of Li<sup>+</sup> diffusivity on FeS<sub>2</sub> is shown in Figure 3. The Li<sub>2</sub>Fe<sub>2</sub>S<sub>2</sub> is formed in one voltage plateau during the initial discharge, and the reaction involves a reduction in metallic Fe and Li<sub>2</sub>S at 1.4 V [9]. After discharge, a consecutive charge shows that FeS and Li<sub>2</sub>S<sub>n</sub> are formed, and these compounds are combined into a complex of polysulfides with partial oxidation to FeS<sub>2</sub> [9, 10] that represents a decrease in capacity from the 1st to the 2nd discharge and subsequent cycles [6, 11, 12] particularly because of the dissolution of intermediates such as lithium polysulfide (Li<sub>2</sub>S<sub>n</sub>, 4 < n < 8) in the liquid electrolyte [11, 13–16].

**3.3. Effect of Variation of Physical Characteristics on Coulombic Efficiency.** A CE calculation was conducted to compare the effect of the particle size on the performance of FeS<sub>2</sub>. The left side of Figure 4 shows a detailed voltage profile for the FeS<sub>2</sub> electrodes, while the right side shows the CE reached during the first four cycles.

Therefore, during the charge–discharge test, despite the shapes of the curves, the five samples show considerably identical results; the electrode created after 10 h PBM shows a discharge capacity of 540 mAh g<sup>-1</sup>, and a nearly identical discharge was obtained for the 72 h SBM, 3 h PBM, 6 h PBM, and pristine samples. An inhomogeneous particle size combination shown by the PSD test in Table 1 might be the first cause of nondifferentiation of the end discharge capacity.

Although the left part of Figure 4 shows that the discharge and charge capacities are almost identical, a detailed comparison to tell the difference between them is hardly possible. Therefore, the graph of CE on the right side indicates some characteristics that differ for each sample. First, the results corresponding to the 0.7–1 range on the coulombic efficiency axis have an acceptable accuracy showing an evident contrast between each cycle. Second, the CE of the 10 h PBM sample increases as follows: 0.752, 0.960, 0.977, and 0.980 from the 1st to the 4th cycle, respectively; no doubt, the percentage of small particle size around 64.3% shown in Table 1 is ineffective if the CE in 10 h PBM is expected to increase as shown in Figure 4. Finally, among all the electrodes, 10 h PBM has the lowest CE in every cycle.

**3.4. Numerical Analysis Evaluation over the Lifetime of the Cell.** To understand the CE better, we extended the analysis

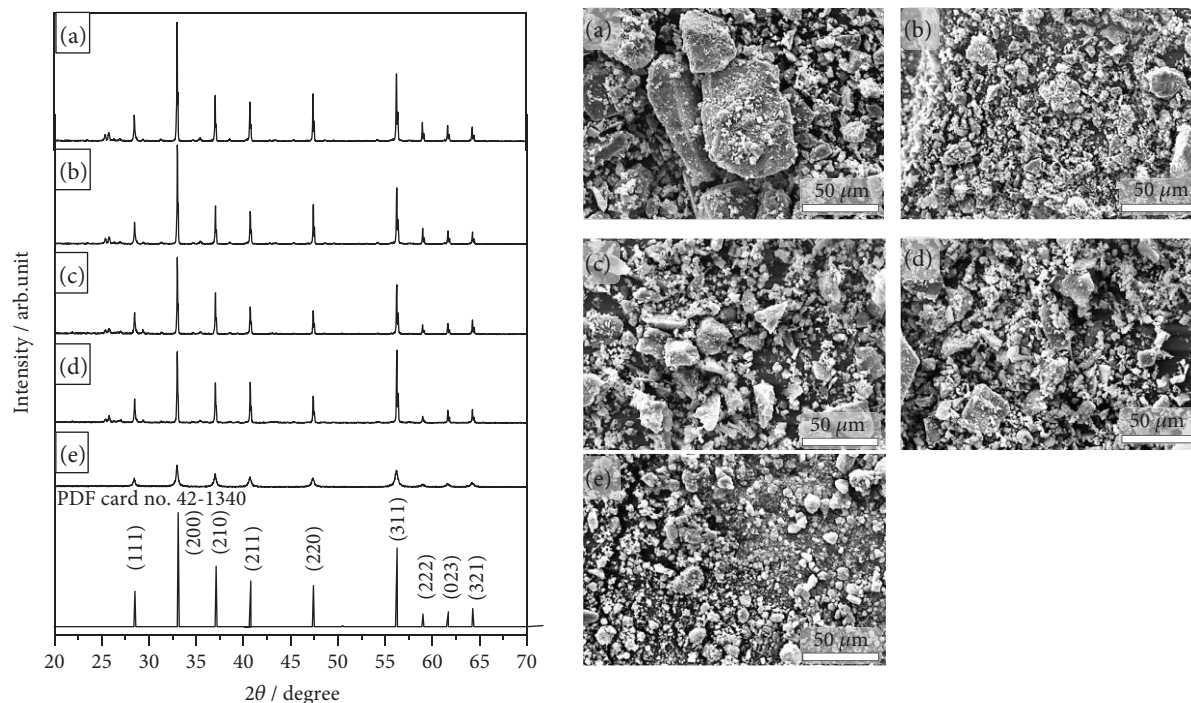


FIGURE 1: XRD patterns and SEM images of (a) pristine, (b) 72 h SBM, (c) 3 h PBM, (d) 6 h PBM, and (e) 10 h PBM.

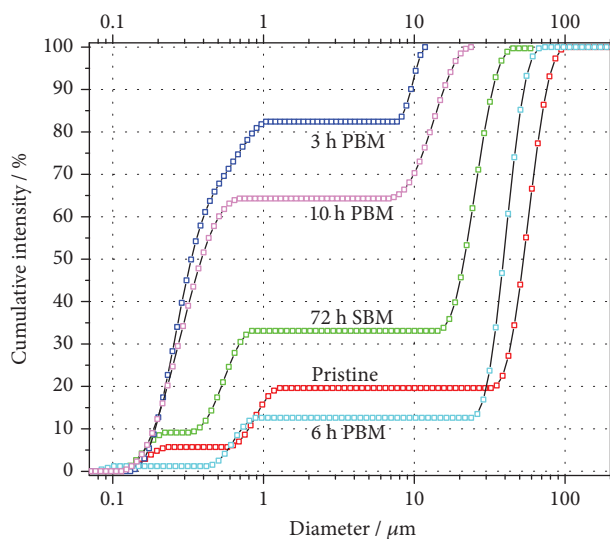


FIGURE 2: Accumulative intensity of particle size vs. diameter of particle in  $\mu\text{m}$ .

TABLE 1: Particle size distribution and percentage representation for different samples.

Sample	Particle size distribution ( $\mu\text{m}$ )	
Pristine	0.1–1.3 (20.0%)	30.0–100.0 (80.0%)
72 h SBM	0.1–0.8 (33.3%)	15.6–50.0 (66.7%)
3 h PBM	0.1–1.1 (81.0%)	8.2–11.8 (19.0%)
6 h PBM	0.6–0.9 (12.6%)	26.1–73.7 (87.4%)
10 h PBM	0.1–0.8 (64.3%)	7.0–25.0 (35.7%)

beyond the results shown in Figure 4 to study the relationship between the CE and discharge capacity against the cycle number, as shown in Figure 5. The continuous discharge–charge process is monitored from the 1st to the 15th cycle and from the 1st to the 60th cycle for short- and long-term tests, respectively. To evaluate comparable end points, the testing process follows a specific pattern during the data collection, as shown in the left side of the figure. The increase, decrease, and stabilization of the end discharge capacity points observed during the first 15 cycles can be attributed to the conditioning of the half-cells, a period that occurs after the electrolyte penetrates the electrode [17]. This increases the contact area between the electrode, electrolyte, and Cu foil, which yields an increment in the capacity. The right side of Figure 5 shows that the CE values for the 3 h PBM and pristine samples are the highest (over 0.99), followed by those of the 72 h SBM and 6 h PBM samples, whereas the CE of the 10 h PBM sample is the lowest.

After a visual comparison of the graph, numerical analysis was used to rank the electrodes and a nonlinear curve fitting analysis was used to verify the arrangement. This curve, which is obtained from the Chapman model  $y = a * (1 - \exp(-b * x))^c$ , shows the best fit to the shapes of the curves, as all the CE curve shapes are quite similar with a pronounced increase at the beginning and an asymptotic pattern around the value of 1. This adjustment makes it possible to give every electrode an adjusted  $R$ -square value over 0.99, a value that explains how close the data are to the fitted regression curve. This method was chosen because it is one of the most practical ways to approximate the model using a curve and refine the parameters via successive iterations. This analysis enables us to rank the aging.

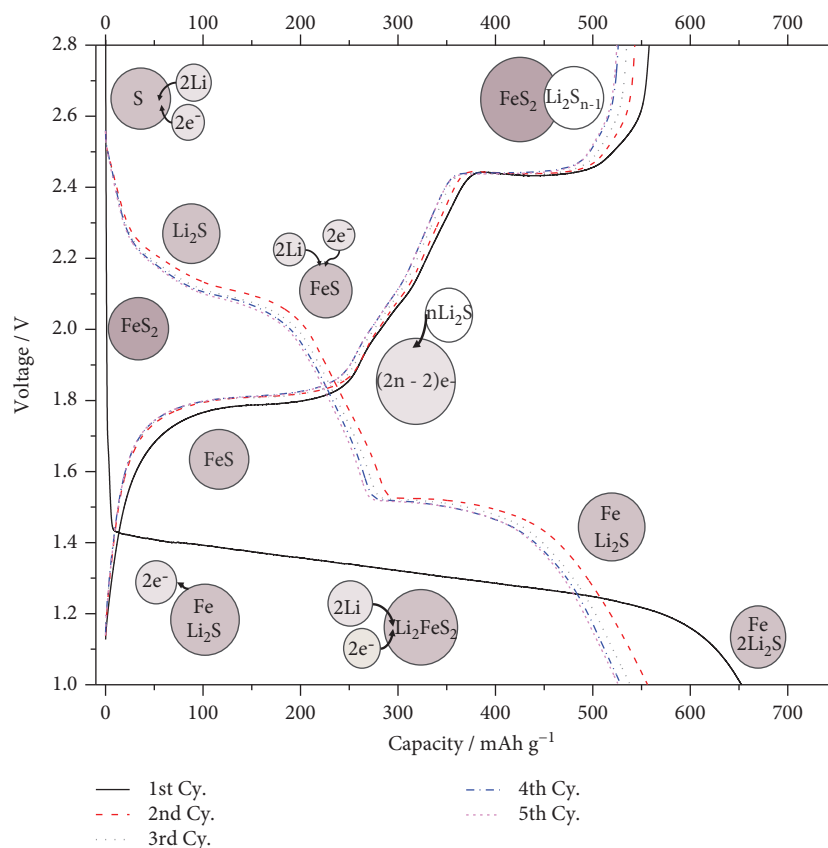


FIGURE 3: Charge and discharge mechanism of the  $\text{FeS}_2$  electrode in 1M  $\text{LiClO}_4/\text{EC}:\text{DMC}$  (1:1 v/v) at a constant current of  $89.2\text{ mA g}^{-1}$  (0.1 C).

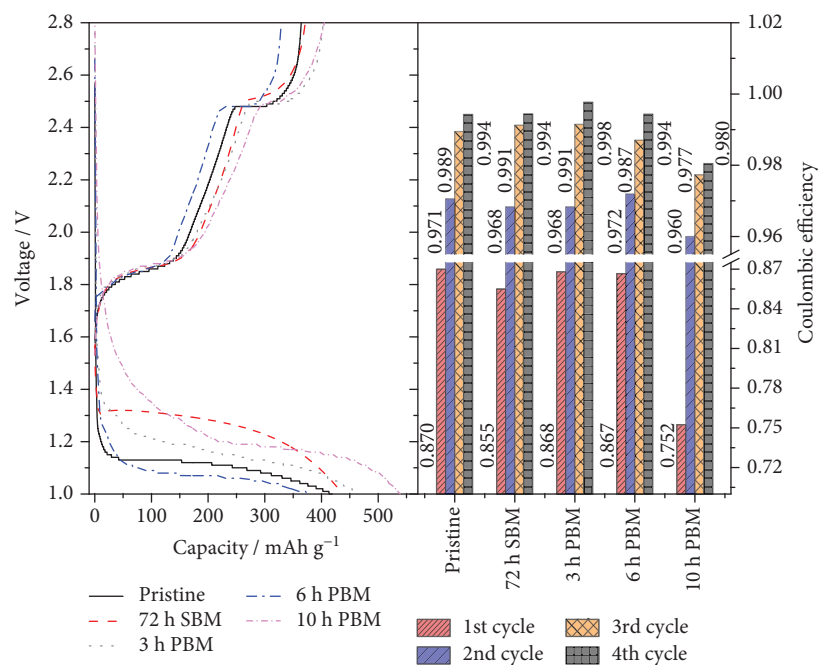


FIGURE 4: (Left) charge and discharge curves of the  $\text{FeS}_2$  electrode in 1M  $\text{LiClO}_4/\text{EC}:\text{DMC}$  (1:1 v/v) at a constant current of  $892\text{ mA g}^{-1}$  (1 C). (Right) coulombic efficiency reached during the first four cycles.

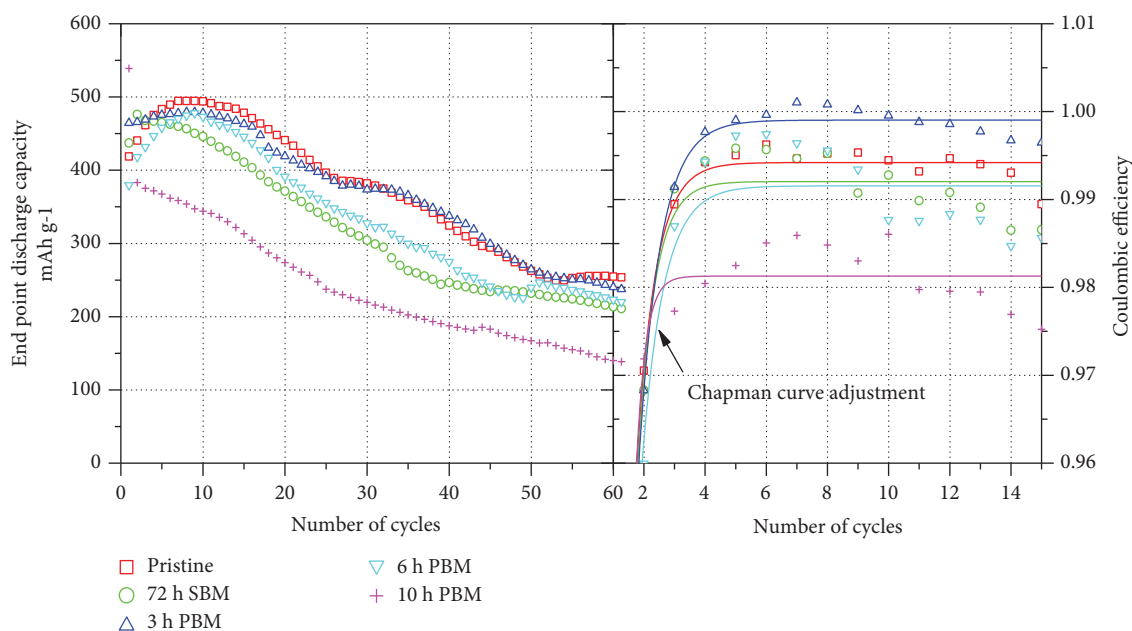


FIGURE 5: (Left) results of the coulombic efficiency vs. cycle number and (right) end point discharge capacity vs. cycle number for FeS<sub>2</sub> electrodes in 1 M LiClO<sub>4</sub>/EC : DMC (1 : 1 v/v) at a constant current of 892 mA g<sup>-1</sup>.

TABLE 2: Capacity loss rate per cycle of milled FeS<sub>2</sub> samples calculated over the last 60 cycles and nonlinear curve fitting report.

Sample	Value	Chapman R-square	Capacity loss rate per cycle (%)
3 h PBM	$a = 0.99904$	0.99830	0.97
	$b = 1.39988$		
	$c = 0.49678$		
Pristine	$a = 0.99421$	0.99727	1.62
	$b = 1.62866$		
	$c = 0.61185$		
72 h SBM	$a = 0.99204$	0.99063	1.80
	$b = 1.79919$		
	$c = 0.82355$		
6 h PBM	$a = 0.99155$	0.97778	1.83
	$b = 1.40964$		
	$c = 0.48300$		
10 h PBM	$a = 0.98128$	0.99634	2.03
	$b = 3.26758$		
	$c = 6.84182$		

Table 2 shows the Chapman model curve fitting results for a short-term test. The independent variables are denoted as “ $a$ ,” “ $b$ ,” and “ $c$ ,” where the variable “ $a$ ” represents the horizontal asymptote of 1, a value that helps us rank all the samples from the 1st to the 5th as follows: 3 h PBM, pristine, 72 h SBM, 6 h PBM, and 10 h PBM based on values of 0.99904, 0.99421, 0.99204, 0.99155, and 0.98128, respectively.

In the long-term test, the end discharge capacity behavior indicated a fading rate of the capacity, which is expressed as the “capacity loss rate per cycle” at the FeS<sub>2</sub> electrode. This capacity loss rate is also shown in Table 2. A capacity loss rate, calculated over 60 cycles, of 0.97% per cycle, is recorded for the 3 h PBM sample, which is slightly lower than the value of 1.62% obtained for the pristine electrode. This indicates a better lithiation–delithiation for the 3 h PBM electrodes. In contrast, the half-cell that contains the 10 h PBM sample has a value of 2.03%, which is the highest discharge capacity loss registered from the beginning, indicating poor lithiation in the electrode. This may be due to the difference in capacity for the first two discharge capacities, i.e., 539 and 383 mAh g<sup>-1</sup>, respectively. This behavior is expected, as explained above, where new reactions result in new compounds.

The short-term test can be used to identify and demonstrate the change in the CE in Li-ion cells during cycling, as shown in Figure 5. Hence, this test, rather than the long-term test until the end of the cell lifetime, should be able to predict a set of failures in the half-cell. There is enough evidence to confirm that this type of evaluation can be of significant use in differentiating and finding parameters that reduce the cell lifetime.

#### 4. Conclusions

We created a ranking of the deterioration between electrodes based on their CE. This method can be used for quantifying the decay of the electrodes during the cycling process using a short-term test. A careful measurement of the CE would allow the evaluation of a cell over 15 cycles via a short-term test, which is less time-consuming than long tests (over 60 cycles). We confirm that a physical particle reduction

produces a slight increase in the CE in the 3 h PBM FeS<sub>2</sub> sample, which has the highest CE among all the samples.

Although the performance obtained was not optimal, the connection between the CE and capacity loss rate was determined, which facilitates an in-depth understanding of FeS<sub>2</sub> electrodes, indicating the effectiveness of this method.

Although this test enables us to determine the effects of the polysulfides on CE, this procedure does not quantify the polysulfides in the sample. Further investigations on CE and the use of X-ray photoelectron spectroscopy would help us find a connection between the battery decay and elements that affect the Li/FeS<sub>2</sub> half-cell.

## Data Availability

The data that support the findings of this study are available from the corresponding author, Soon-Ki Jeong, upon reasonable request.

## Conflicts of Interest

The authors declare that there is no conflict of interest regarding the publication of this paper.

## Acknowledgments

This work was supported by the Korea Institute of Energy Technology Evaluation and Planning (KETEP) and the Ministry of Trade, Industry & Energy, Republic of Korea (no. 20184030202130). This work was supported by Soonchunhyang University Research Fund.

## References

- [1] S. Erik, B. Jason, C. Schmidt, and W. Howard, "A practical longevity model for lithium-ion batteries: de-coupling the time and cycle-dependence of capacity fade," *Journal of the Electrochemical Society*, vol. 140, p. 208, 2005.
- [2] J. Jiang, Z. Lin, Q. Ju, Z. Ma, C. Zheng, and Z. Wang, "Electrochemical impedance spectra for lithium-ion battery ageing considering the rate of discharge ability," *Energy Procedia*, vol. 105, pp. 844–849, 2017.
- [3] P. Keil and A. Jossen, "Calendar aging of NCA lithium-ion batteries investigated by differential voltage analysis and coulomb tracking," *Journal of the Electrochemical Society*, vol. 164, no. 1, pp. A6066–A6074, 2017.
- [4] J. W. Choi, G. Cheruvally, H. J. Ahn, K. W. Kim, and J. H. Ahn, "Electrochemical characteristics of room temperature Li/FeS<sub>2</sub> batteries with natural pyrite cathode," *Journal of Power Sources*, vol. 163, no. 1, pp. 158–165, 2006.
- [5] A. J. Smith, J. C. Burns, S. Trussler, and J. R. Dahn, "Precision measurements of the coulombic efficiency of lithium-ion batteries and of electrode materials for lithium-ion batteries," *Journal of the Electrochemical Society*, vol. 157, no. 2, p. A196, 2010.
- [6] S. S. Zhang and D. T. Tran, "Electrochemical verification of the redox mechanism of FeS<sub>2</sub> in a rechargeable lithium battery," *Electrochimica Acta*, vol. 176, pp. 784–789, 2015.
- [7] D. Zhang, J. P. Tu, J. Y. Xiang et al., "Influence of particle size on electrochemical performances of pyrite FeS<sub>2</sub> for Li-ion batteries," *Electrochimica Acta*, vol. 56, no. 27, pp. 9980–9985, 2011.
- [8] Y. Shao-Horn, S. Osmialowski, and Q. C. Horn, "Nano-FeS<sub>2</sub> for commercial Li / FeS<sub>2</sub> primary batteries," *Journal of the Electrochemical Society*, vol. 149, no. 11, article A1499, 2002.
- [9] T. Evans, D. M. Piper, S. C. Kim et al., "Ionic liquid enabled FeS<sub>2</sub> for high-energy-density lithium-ion batteries," *Advanced Materials*, vol. 26, no. 43, pp. 7386–7392, 2014.
- [10] Q. Wang and Y. Wang, "Overcoming the limiting step of Fe<sub>2</sub>O<sub>3</sub> reduction via in situ sulfide modification," *ACS Applied Materials and Interfaces*, vol. 8, no. 16, pp. 10334–10342, 2016.
- [11] S. S. Zhang, "The redox mechanism of FeS<sub>2</sub> in non-aqueous electrolytes for lithium and sodium batteries," *Journal of Materials Chemistry A*, vol. 3, no. 15, pp. 7689–7694, 2015.
- [12] X. B. Cheng, J. Q. Huang, H. J. Peng et al., "Polysulfide shuttle control: towards a lithium-sulfur battery with superior capacity performance up to 1000 cycles by matching the sulfur/electrolyte loading," *Journal of Power Sources*, vol. 253, pp. 263–268, 2014.
- [13] T. Mori, Y. Orikasa, K. Nakanishi et al., "Discharge/charge reaction mechanisms of FeS<sub>2</sub> cathode material for aluminum rechargeable batteries at 55°C," *Journal of Power Sources*, vol. 313, pp. 9–14, 2016.
- [14] J. Yang, M. Liu, Z. Wei et al., "Controlling electrochemical lithiation/delithiation reaction paths for long-cycle life nanochain-structured FeS<sub>2</sub> electrodes," *Electrochimica Acta*, vol. 211, pp. 671–678, 2016.
- [15] F. Zhang, C. Wang, G. Huang, D. Yin, and L. Wang, "FeS<sub>2</sub>@C nanowires derived from organic-inorganic hybrid nanowires for high-rate and long-life lithium-ion batteries," *Journal of Power Sources*, vol. 328, pp. 56–64, 2016.
- [16] V. Pele, F. Flamary, L. Bourgeois, B. Pecquenard, and F. Le Cras, "Perfect reversibility of the lithium insertion in FeS<sub>2</sub>: the combined effects of all-solid-state and thin film cell configurations," *Electrochemistry Communications*, vol. 51, pp. 81–84, 2015.
- [17] K. Sun, Q. Zhang, D. C. Bock et al., "Interaction of TiS<sub>2</sub> and sulfur in Li-S battery system," *Journal of the Electrochemical Society*, vol. 164, no. 6, pp. A1291–A1297, 2017.

## Research Article

# Experimental Study of Al<sub>2</sub>O<sub>3</sub> Nanofluids on the Thermal Efficiency of Curved Heat Pipe at Different Tilt Angle

S. Razvarz <sup>1</sup> and R. Jafari <sup>2</sup>

<sup>1</sup>Departamento de Control Automatico CINVESTAV-IPN (National Polytechnic Institute), Mexico City, MEX, Mexico

<sup>2</sup>Centere for Artificial Intelligence Research (CAIR), University of Agder, 4879 Grimstad, Norway

Correspondence should be addressed to S. Razvarz; srazvarz@yahoo.com

Received 20 January 2018; Revised 8 June 2018; Accepted 1 August 2018; Published 2 September 2018

Academic Editor: S. N. Karthick

Copyright © 2018 S. Razvarz and R. Jafari. This is an open access article distributed under the Creative Commons Attribution License, which permits unrestricted use, distribution, and reproduction in any medium, provided the original work is properly cited.

This paper represents an experimental study about the effect of curves related to thermosyphons and heat pipes with different active fluids and inclination angle at the thermal efficiency. The nanofluid utilized in this work is an aqueous soluble of Al<sub>2</sub>O<sub>3</sub> nanoparticles with 35 nm diameter in pure water. The test saturation level of nanoparticles is 0%, 1%, and 3%wt. All the experiments were conducted and repeated at inclination angle of 30°, 60°, and 90° (vertical). The article presents the gravity impacts on the heat transfer characteristics in different angles and the effects of working fluids and tilt angle of heat pipe tube by the addition of nanoparticles and weight fractions on the thermal efficiency of heat pipe at different inclination. According to the experimental results, the heat pipe at the tilt angle of 60° generates the superior results. At a particle volume concentration of 1%, the use of Al<sub>2</sub>O<sub>3</sub>/water nanofluid gives significantly higher heat transfer.

## 1. Introduction

Recently, the problem of heat dissipation from the electronic equipment is taken into consideration by using a new heat transfer devices such as heat pipe. Thermosyphons as well as heat pipes have been utilized in various applications related to the electronics industry which contains a superior speed and a high level of heat generation. Heat pipes are capable of transferring and removing the heat from a heat source over long distances. Heat pipes use the latent heat of vaporization of a working fluid to transfer heat.

Wei et al. [1] experimentally analysed the enhancement of thermal efficiency of grooved heat pipe charged with the silver nanoparticles and deionized water. Lin et al. [2] studied a research focusing on heat transfer of R141b and multiphase flow in a tube. Gao et al. [3] developed high efficiency in small heat pipes for high heat flux cooling. Ma et al. [4, 5] investigated the pulsating heat pipe charged with diamond nanofluids. In [6, 7], the authors have studied the results of axial rotational speed in heat pipes under steady-state operation. In [8, 9], the impacts of anisotropic shape and gravity of

the conducting nanoparticle in nanofluid thermal conductivity have been studied. Liu et al. [10] considered the effects of vapor pressure at the critical values of the evaporator boundaries and length. In [11, 12], the positive effect over the nanofluid specifications based on the betterment of the thermal conductivity of liquids is considered and the effects of nanoparticle mean diameter on the heat transfer have been studied. Jang and Choi [13] checked numerically the cooling performance of a microchannel heat sink with nanofluid. Nguyen et al. [14] studied the increment of a particular nanofluid for cooling electronic components. Atmar and Zeinab [15] investigated extraction from clarified rumen fluid by modified magnetic nanoparticles. Nguyen et al. [16] evaluated the heat transfer behaviour of the water—Al<sub>2</sub>O<sub>3</sub> and ethylene glycol—Al<sub>2</sub>O<sub>3</sub> nanofluids in a heated tube. Hwang et al. [17, 18] measured kinematic viscosity, thermal conductivity, and thermophysical properties of nanofluids in heat transfer of the heat pipe. Kang et al. [19] added Ag pure water nanofluids in 1 mm wick-thickness sintered circular pipe to study the heat transfer performance of the heat pipe. He et al. [20] studied the methodology of heat-transfer phenomena and

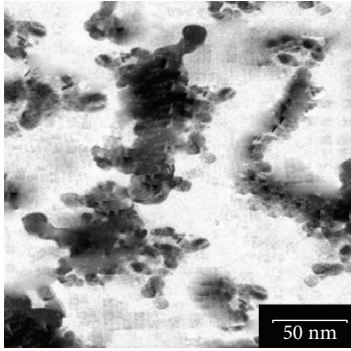


FIGURE 1: TEM photograph of  $\text{Al}_2\text{O}_3$  particles.

flow behaviour of  $\text{TiO}_2$  nanofluid with different particle sizes and concentrations upon upward flow through a vertical pipe. Moraveji and Razvarz [21] investigated on the outcome of  $\text{Al}_2\text{O}_3$  nanofluids related to the thermal performance of the heat pipe; also, they demonstrated that more nanoparticles will cause a better performance in the heat pipe. Their results indicate that increasing the nanoparticle concentration and temperature could enhance the convective heat transfer coefficient of nanofluid. Saha et al. [22] studied the effect of process variables on the heat pipe; also, the observation reveals different operating ranges which depends on the loop orientation, filling ratio as well as input power. Asirvatham et al. [23] studied silver nanoparticles by dispersing in deionized water to improve heat transfer performance of a heat pipe. Xue and Qu [24] experimentally examined the effects of inclination angles to ammonia heat pipe and observed the thermal resistance increment or decrement. Batmani et al. [25] measured the effects of  $\text{Al}_2\text{O}_3$  nanoparticle on the compression flow curve of AZ11 magnesium alloy and they showed that the nano- $\text{Al}_2\text{O}_3$  particulates improves the compressive yield strength of AZ11 magnesium alloy. Various researchers has been done studies principal measurement of thermal conductivity of nanofluids large number of exploratory and hypothetical [26, 27].

In the present study, the experimental results of the influence of  $\text{Al}_2\text{O}_3$  nanofluid on grooved and curved heat pipes are studied. Furthermore, the comparison of the thermal performance of  $\text{Al}_2\text{O}_3$  nanofluid with pure water is investigated. In continuation, the effects of nanoparticle volume percentage concentration and the gravitational effect is studied by placing evaporator at different orientation. As mentioned above, this paper presents the study on heat transfer in the curved heat pipe in an adiabatic section and the effect of heat pipe tilt angle that have rarely been reported. The results of this paper will be helpful in logical choice of acceptable percentage of nanoparticle in heat transfer.

## 2. Experimental Setup and Procedure

### 2.1. Characterization and Preparation of $\text{Al}_2\text{O}_3$ Nanofluids.

The base working fluid is pure water in this experiment, and  $\text{Al}_2\text{O}_3$  nanoparticles are the most common nanoparticles used with 30 nm and 45 nm in size measured by transmission electron microscopy (TEM). Figure 1 is the TEM photograph

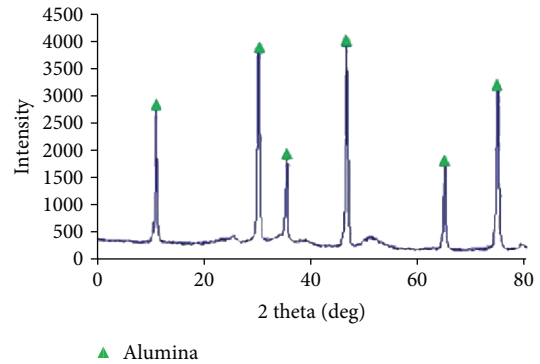


FIGURE 2: XRD Pattern of as-sprayed alumina nanoparticles.

of  $\text{Al}_2\text{O}_3$  nanoparticles with particle size about 35 nm which were added to pure water. The nanofluid used in this experiment is made of 99.0% pure aluminium oxide with an average particle size of 35 nm predispersed in water, and the precursors for its thermal deposition are trimethylaluminum (TMA) and water. XRD studies were also conducted to trace the conversion of  $\text{Al}_2\text{O}_3$ . Figure 2 shows the XRD pattern of the flame-sprayed nanoparticles. It can be seen from Figure 2 that  $\text{Al}_2\text{O}_3$  were found in the as-sprayed nanoparticles.  $\text{Al}_2\text{O}_3$  particles' true density is  $3880 \text{ kg/m}^3$ , which can be converted to weight fraction and volume fraction. The nanoparticles and pure water are mixed by utilizing an ultrasonic homogenizer with the concentration of 0, 1%, and 3% by weight.  $\text{Al}_2\text{O}_3$  nanoparticles are generated by using a catalytic chemical vapor deposition technique. Aluminium oxide nanomaterials have been synthesized using precursors such as methane, acetylene, toluene, xylene, and benzene. As a matter of fact, one could use any type of hydrocarbon or carbonaceous materials for the synthesis of aluminium oxide nanomaterials.

**2.2. Experimental Setup.** The schematic diagram of the heat pipe under consideration is shown in Figure 3. The loop consists of a test section, cool water loop, and data recording system. The water flow at a constant rate is 1.7 L/min. The inlet temperature of the water is controlled and set at the temperature of  $20 \pm 0.5^\circ\text{C}$  by using a thermostatic bath in order to achieve a constant working temperature while the heat input increases. The closed loop of the evaporator contains cold water inside the storage tank having  $0.125 \text{ m}^3$  volume and water pump. Experiments are carried out at various heat fluxes and three different tilt angles. The position of the heat pipe tilt angle is shown in Figure 4. The laboratory temperature is controlled at  $25 \pm 1^\circ\text{C}$ . The heat pipe involved in the experiment is a straight copper tube with an outer diameter of 8 mm and a length of 190 mm that contains 1 mm wick-thickness copper powder (140–200 nm) sintered wicked. The studied heat pipe consists of three sections such as an evaporator, an adiabatic section, and a condenser. The condenser section of the flat heat pipe is inserted vertically into the cooling chamber to remove heat from the condenser section by forced convection to a constant temperature bath. For heating the evaporator section, a 0–220 V AC electric

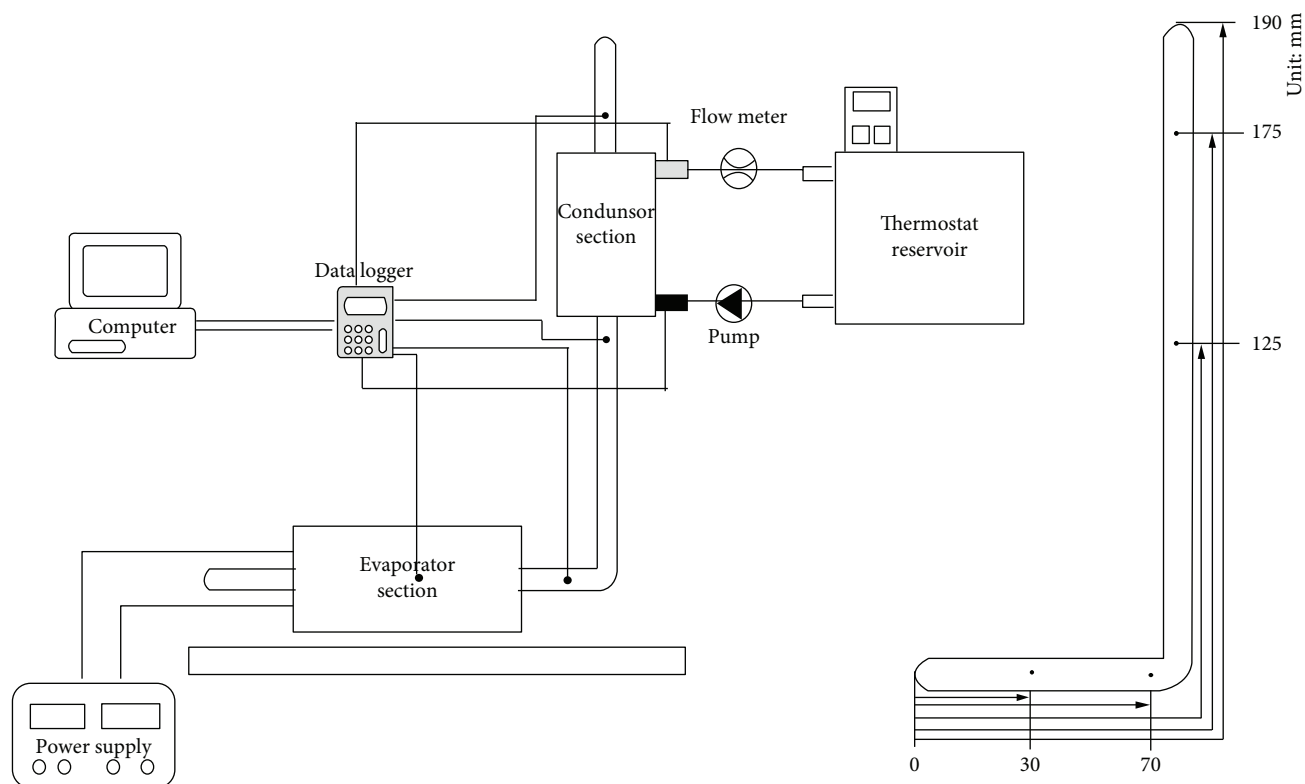


FIGURE 3: Schematics of the test setup.

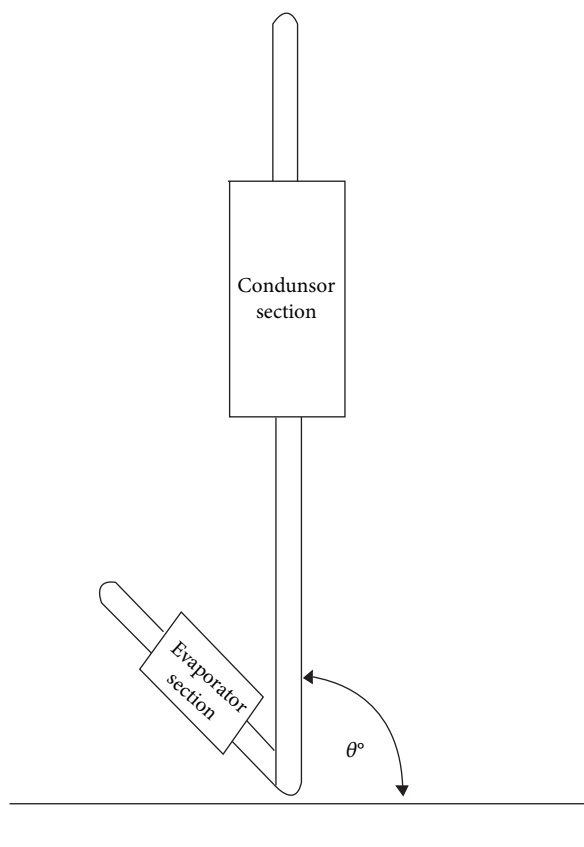


FIGURE 4: Position of tilt angle of the heat pipe.

heater is used. Electric power is obtained by measuring the current supplied to the electric heater and the voltage across the heating resistor. The electrical heater is glued with thermal grease master cooler HTX3-GL to decrease the contact thermal resistance between the heater and the heat pipe.

**2.3. Test Procedure.** The power supply is switched on initially, and then the power is increased. The tests require approximately 15–25 minutes to reach the steady state. In each step, the temperatures and other experimental parameters are recorded at the steady state conditions. Afterwards, the power input is increased, and so the process is iterated until the occurrence of dry out as found out by rapid spikes in the evaporator thermal couple which is far from the condenser. Once dry out is attained, difference between temperature of the evaporator and condenser increases rapidly.

The local temperature is measured by using four isolated type T thermocouples. Thermocouple signals are recorded by a data logger (Fluke, Hydra Series II) with the uncertainty lower than  $0.1^{\circ}\text{C}$ . Thermocouples are distributed along the surfaces of the heat pipe section as follows: one thermocouple is attached to the condenser section, two thermocouples are attached to the adiabatic section, and one thermocouple is attached in the middle of evaporator section. Through record and calculation, the ratio of removed energy of cooling water by condenser section to the heating power by evaporator section with different weight fraction of nanoparticle, and tilt angle of heat pipe, the effects of thermal efficiency under different

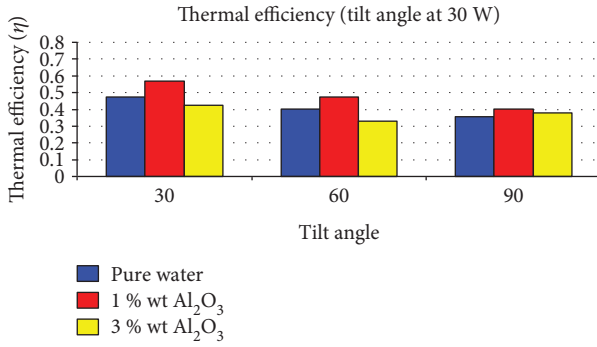


FIGURE 5: Alteration of thermal efficiency of heat pipes by various tilt angles and fluids of heat pipes at 30 W power.

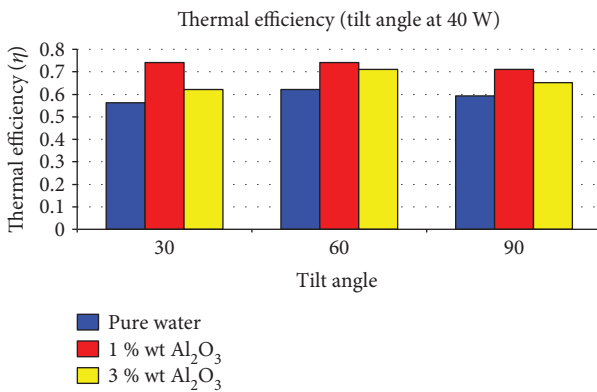


FIGURE 6: Alteration of thermal efficiency of heat pipes by various tilt angles and fluids of heat pipes at 40 W power.

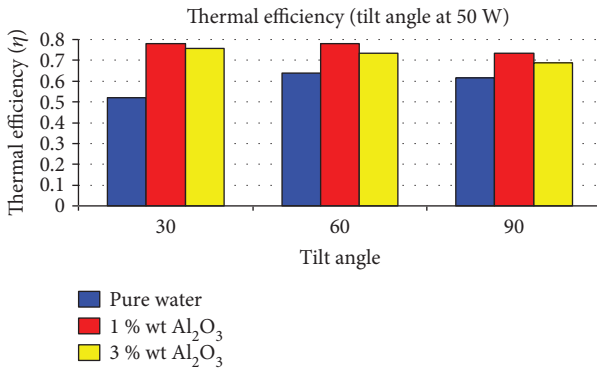


FIGURE 7: Alteration of thermal efficiency of heat pipes by various tilt angles and fluids of heat pipes at 50 W power.

tilt angle and nanofluid can be evaluated. The heat pipe efficiency can be calculated as follows:

$$\eta = m_w C_p \frac{(T_{\text{wout}} - T_{\text{win}})}{(V.I)} \quad (1)$$

### 3. Results and Discussion

The enhancement of convective heat transfer coefficient depends on increasing of the fluid thermal conductivity.

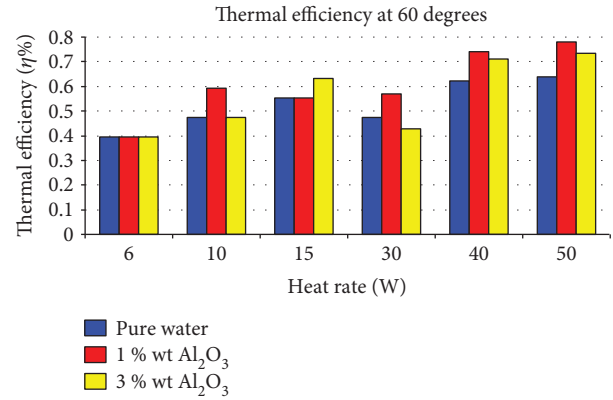


FIGURE 8: Variations of thermal efficiency in different heat rate at 60° tilt.

Thermal conductivity of the nanofluids increases with increasing of the volume concentrations. Adding nanoparticles to liquid strikingly improves energy transport process of the base liquid. A smaller particle size would provide a much larger surface area for molecular collisions and therefore increase the rate of reaction, making it a better catalyst and reactant.

The form of heat pipe, working fluid, and effect of gravity has a considerable effect on its efficiency. In this experiment, several conditions for fluid is taken into consideration, in order to measure the temperature distribution of heat pipe as well as cooling water the evaporator and condenser.

In vertical mode, the vapor bubbles which take up heat in the evaporator grow in size. Their own buoyancy helps them to rise up in the tube section. The rising bubbles in the tube is a natural tendency for the liquid slugs to travel downwards, helped by gravity force, toward the evaporator. In horizontal mode (90° inclination angle) of operation, there was hardly any macromovement of bubbles. This strongly suggests that gravity does play a role in the heat pipe. Since gravity force is ineffective, all the movement of bubbles and slugs has to be necessarily done by the pressure forces. These forces are created due to temperature difference, which exists between evaporator and condenser.

Figures 5 and 6 as well as Figure 7 display the alteration of thermal efficiency related to the heat pipe. By utilizing fluids with various concentration percent of Al<sub>2</sub>O<sub>3</sub> nanoparticles at 30, 60, and 90 tilt angles, different results can be obtained. The increment of tilt angle will cause the enhancement of flow back into the evaporator section. By increment the tilt angle from 0 to 60, the thermal efficiency increases, but if the increment is more than 60°, the thermal efficiency will decrease. The reason is that the effect of gravitational force between the evaporator section and the condenser section is increased. On the other hand, when the tilt angle of heat pipe is taken to be constant, then by adding nanoparticles to the base fluid, the efficacy of thermal conductivity will be increased. The addition of more nanoparticles to fluid causes the property of working fluid at the evaporator section to convert into the solid phase. Also, it results in the decrease of the convection performance of nanofluid inside the

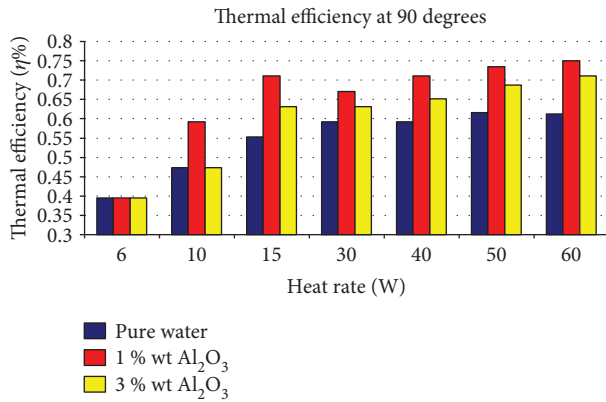


FIGURE 9: Variations of thermal efficiency in different heat rate at 90° tilt.

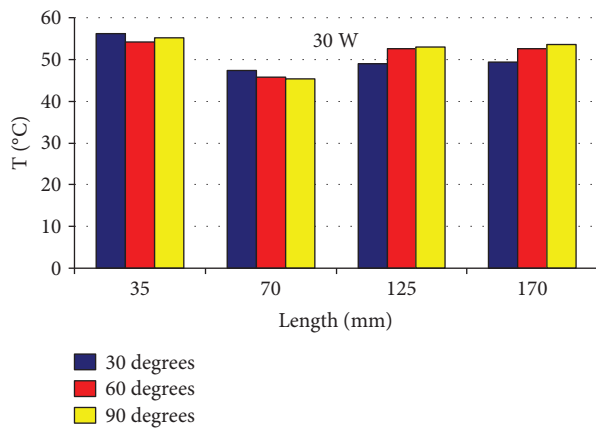


FIGURE 10: Temperature of heat pipe diffusion in different tilt angles of heat pipes at 1.0 wt. % under 30 W input power.

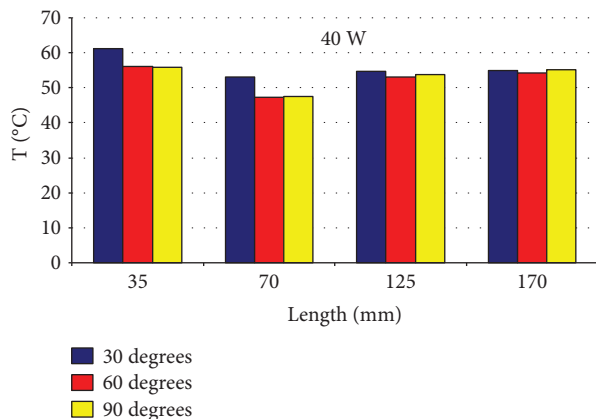


FIGURE 11: Temperature of heat pipe diffusion in different tilt angles of heat pipes at 1.0 wt. % under 40 W input power.

evaporator section. Figures 8 and 9 display that at constant angle of the heat pipe, by the increment of heat rate, the heat pipe efficiency will be increased. In these figures, it can be

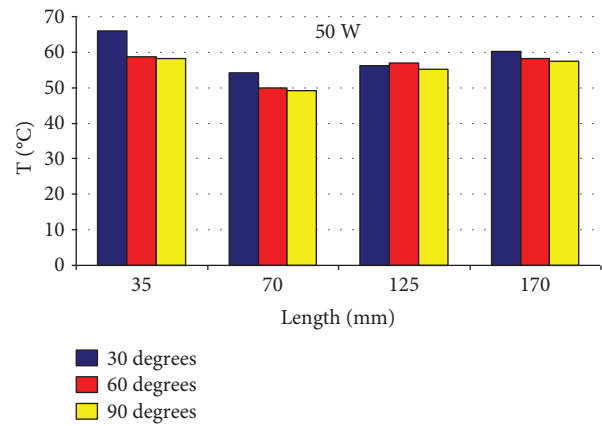


FIGURE 12: Temperature of heat pipe diffusion in different tilt angles of heat pipes at 1.0 wt.% under 50 W input power.

seen that after the tilt angle of 60° (Figure 8), the heat pipe efficiency has been decreased. The temperatures of heat pipe diffusion have been shown in Figures 10–12 in various tilt angles of heat pipes at 1.0 wt % concentration under different input power.

As can be seen, increasing the contact angle causes the condensed vapor to return faster to the evaporator section by means of gravity, and consequently, lower thermal resistances and higher heat transfer coefficients were obtained.

#### 4. Conclusions

In this paper, an experimental research of the thermal enhancement related to the heat pipe is carried out proficiently by adding Al<sub>2</sub>O<sub>3</sub> nanopowder to pure water in side 1 mm wick-thickness sintered circular heat pipe in various tilt angles. The gravity effects on the heat transfer in the heat pipe have been experimentally studied in the paper by four kinds of test orientations.

Important conclusions have been obtained and are summarized as follows:

- (i) The ideal value of thermal efficiency obtains at the concentration of 1.0% wt nanofluid.
- (ii) The heat transfer coefficient increases with increasing the applied heat flux at the evaporator.
- (iii) Adding Al<sub>2</sub>O<sub>3</sub> nanoparticles to pure water could enhance the thermal efficiency of heat pipe.
- (iv) With enhancement of the heat flux, the heat pipe efficiency tends to increase.
- (v) In this experiment, the thermal efficiency of the heat pipe with 0.1% nanoparticle volume concentration is higher than other fluids with different nanoparticle volume concentration.
- (vi) Effects of heat pipe tilt angle on the thermal efficiency are checked and is shown that it can be increased at higher tilt angle.

- (vii) The inclination angle has a great effect on the heat pipe thermal resistance using water as the working fluid.
- (viii) The heat pipe thermal efficiency get enhanced with increasing nanoparticle concentrations and tilt angles.
- (ix) The heat pipe thermal efficiency of the nanoparticle fluids decreases when the heat pipe tilt angle is 60°.

## Data Availability

The data used to support the findings of this study are available from the corresponding author upon request.

## Disclosure

This paper is an extension version of the work originally presented in [28].

## Conflicts of Interest

The authors declare that they have no conflicts of interest.

## Acknowledgments

Also, the authors would like to thank Eng. Roberto Lagunes Feregrino and Eng. José de Jesús Meza Serrano for their helpful cooperation, which has helped the authors in improving the quality of this manuscript.

## References

- [1] W. C. Wei, S. H. Tsai, S. Y. Yang, and S. W. Kang, "Effect of nano-fluid concentration on heat pipe thermal performance," *IEEE SEMI-THERM Symposium*, vol. 2, pp. 1432–1439, 2005.
- [2] S. Lin, P. A. Kew, and K. Cornwell, "Two-phase heat transfer to a refrigerant in a 1 mm diameter tube," *International Journal of Refrigeration*, vol. 24, no. 1, pp. 51–56, 2001.
- [3] W. Gao, C. Li, C. Xu, and D. Wang, "Experimental study on water separation process in a novel spray flash vacuum evaporator with heat-pipe," *Desalination*, vol. 386, pp. 39–47, 2016.
- [4] H. B. Ma, C. Wilson, B. Borgmeyer et al., "Effect of nanofluid on the heat transport capability in an oscillating heat pipe," *Applied Physics Letters*, vol. 88, no. 14, article 143116, 2006.
- [5] K. Park and H. Ma, "Nanofluid effect on the heat transport capability in a well-balanced oscillating heat pipe," *Journal of Thermophysics and Heat Transfer*, vol. 21, no. 2, pp. 443–445, 2007.
- [6] F. Song, D. Ewing, and C. Y. Ching, "Experimental investigation on the heat transfer characteristics of axial rotating heat pipes," *International Journal of Heat and Mass Transfer*, vol. 47, no. 22, pp. 4721–4731, 2004.
- [7] W. Lian, W. Chang, and Y. Xuan, "Numerical investigation on flow and thermal features of a rotating heat pipe," *Applied Thermal Engineering*, vol. 101, pp. 92–100, 2016.
- [8] L. Gao and X. F. Zhou, "Differential effective medium theory for thermal conductivity in nanofluids," *Physics Letters A*, vol. 348, no. 3-6, pp. 355–360, 2006.
- [9] H. Li, B. Zhou, Y. Tang, R. Zhou, Z. Liu, and Y. Xie, "Effect of working fluid on heat transfer performance of the anti-gravity loop-shaped heat pipe," *Applied Thermal Engineering*, vol. 88, pp. 391–397, 2015.
- [10] D. Liu, G. F. Tang, F. Y. Zhao, and H. Q. Wang, "Modeling and experimental investigation of looped separate heat pipe as waste heat recovery facility," *Applied Thermal Engineering*, vol. 26, no. 17-18, pp. 2433–2441, 2006.
- [11] J. Choi, W. Sano, W. Zhang, Y. Yuan, Y. Lee, and D. A. Borca-Tasciuc, "Experimental investigation on sintered porous wicks for miniature loop heat pipe applications," *Experimental Thermal and Fluid Science*, vol. 51, pp. 271–278, 2013.
- [12] M. Khan and R. Malik, "Forced convective heat transfer to Sisko nanofluid past a stretching cylinder in the presence of variable thermal conductivity," *Journal of Molecular Liquids*, vol. 218, pp. 1–7, 2016.
- [13] S. P. Jang and S. U. S. Choi, "Cooling performance of a micro-channel heat sink with nanofluids," *Applied Thermal Engineering*, vol. 26, no. 17-18, pp. 2457–2463, 2006.
- [14] C. T. Nguyen, G. Roy, C. Gauthier, and N. Galanis, "Heat transfer enhancement using Al<sub>2</sub>O<sub>3</sub>-water nanofluid for an electronic liquid cooling system," *Applied Thermal Engineering*, vol. 27, no. 8-9, pp. 1501–1506, 2007.
- [15] A. Atmar and R. Zeinab, "Xylanase extraction from clarified rumen fluid by modified magnetic nano-particles," *International Journal of Advanced and Applied Sciences*, vol. 7, pp. 44–51, 2014.
- [16] N. B. Chien, P. Q. Vu, N. Mohd-Ghazali, and O. Jong-Taek, "Convective heat transfer characteristics of single phase liquid in multiport minichannel tube: experiment and CFD simulation," *Energy Procedia*, vol. 75, pp. 3180–3185, 2015.
- [17] Y. J. Hwang, Y. C. Ahn, H. S. Shin et al., "Investigation on characteristics of thermal conductivity enhancement of nanofluids," *Current Applied Physics*, vol. 6, no. 6, pp. 1068–1071, 2006.
- [18] Y. Hwang, H. S. Park, J. K. Lee, and W. H. Jung, "Thermal conductivity and lubrication characteristics of nanofluids," *Current Applied Physics*, vol. 6, Supplement 1, pp. e67–e71, 2006.
- [19] S. W. Kang, W. C. Wei, S. H. Tsai, and C. C. Huang, "Experimental investigation of nanofluids on sintered heat pipe thermal performance," *Applied Thermal Engineering*, vol. 29, no. 5-6, pp. 973–979, 2009.
- [20] Y. He, Y. Jin, H. Chen, Y. Ding, D. Cang, and H. Lu, "Heat transfer and flow behaviour of aqueous suspensions of TiO<sub>2</sub> nanoparticles (nanofluids) flowing upward through a vertical pipe," *International Journal of Heat and Mass Transfer*, vol. 50, no. 11-12, pp. 2272–2281, 2007.
- [21] M. Keshavarz Moraveji and S. Razvarz, "Experimental investigation of aluminum oxide nanofluid on heat pipe thermal performance," *International Communications in Heat and Mass Transfer*, vol. 39, no. 9, pp. 1444–1448, 2012.
- [22] N. Saha, P. K. Das, and P. K. Sharma, "Influence of process variables on the hydrodynamics and performance of a single loop pulsating heat pipe," *International Journal of Heat and Mass Transfer*, vol. 74, pp. 238–250, 2014.
- [23] L. G. Asirvatham, R. Nimmagadda, and S. Wongwises, "Heat transfer performance of screen mesh wick heat pipes using silver-water nanofluid," *International Journal of Heat and Mass Transfer*, vol. 60, pp. 201–209, 2013.
- [24] Z. Xue and W. Qu, "Experimental study on effect of inclination angles to ammonia pulsating heat pipe," *Chinese Journal of Aeronautics*, vol. 27, no. 5, pp. 1122–1127, 2014.

- [25] H. Batmani, S. Tanomand, and H. Babri, "Effects of  $Al_2O_3$  nanoparticle on the compression flow curve of AZ11 magnesium alloy," *International Journal of Advanced and Applied Sciences*, vol. 2, no. 11, pp. 32–37, 2015.
- [26] S. Senthilraja and K. C. K. Vijayakumar, "Analysis of heat transfer coefficient of CuO/water nanofluid using double pipe heat exchanger," *International Journal of Engineering Research and Technology*, vol. 6, no. 5, pp. 675–680, 2013.
- [27] M. S. Khan and T. Dil, "Heat transfer enhancement of automobile radiator using H<sub>2</sub>O–CuO nanofluid," *AIP Advances*, vol. 7, no. 4, article 045018, 2017.
- [28] S. Razvarz and R. Jafari, *Experimental Study of Al<sub>2</sub>O<sub>3</sub> Nanofluids on the Thermal Efficiency of Curved Heat Pipe at Different Tilt Angle*, 2nd international congress on technology - engineering & science (ICONTES), Malaysia, 2016.

## Research Article

# Porous Activated Carbons Derived from *Pleurotus eryngii* for Supercapacitor Applications

Yudan Yuan <sup>1</sup>, Ruowei Yi,<sup>2,3</sup> Yi Sun,<sup>4,5</sup> Jianqiao Zeng,<sup>4,5</sup> Jiaqi Li,<sup>4,5</sup> Jiahao Hu,<sup>4,5</sup> Yinchao Zhao,<sup>4,5</sup> Wei Sun,<sup>6</sup> Chun Zhao,<sup>4,5</sup> Li Yang <sup>2,3</sup> and Cezhou Zhao <sup>1,4,5</sup>

<sup>1</sup>School of Electronic and Information Engineering, Xi'an Jiaotong University, Xi'an 710049, China

<sup>2</sup>Department of Chemistry, Xi'an Jiaotong-Liverpool University, Suzhou 215123, China

<sup>3</sup>Department of Chemistry, University of Liverpool, Liverpool, UK

<sup>4</sup>Department of Electrical and Electronic Engineering, Xi'an Jiaotong-Liverpool University, Suzhou 215123, China

<sup>5</sup>Department of Electrical Engineering and Electronics, University of Liverpool, UK

<sup>6</sup>GMCC Electronic Technology Wuxi Co. Ltd., Wuxi 214000, China

Correspondence should be addressed to Li Yang; [li.yang@xjtlu.edu.cn](mailto:li.yang@xjtlu.edu.cn) and Cezhou Zhao; [cezhou.zhao@xjtlu.edu.cn](mailto:cezhou.zhao@xjtlu.edu.cn)

Received 27 December 2017; Revised 21 March 2018; Accepted 24 April 2018; Published 5 August 2018

Academic Editor: Ananthakumar Ramadoss

Copyright © 2018 Yudan Yuan et al. This is an open access article distributed under the Creative Commons Attribution License, which permits unrestricted use, distribution, and reproduction in any medium, provided the original work is properly cited.

Varieties of natural biomass have been utilized to prepare porous carbon materials for supercapacitor applications. In this work, porous activated carbons derived from *Pleurotus eryngii* were prepared by carbonization and KOH activation. The activated carbons presented a large specific surface area of  $3255 \text{ m}^2 \cdot \text{g}^{-1}$  with high porosity. The as-prepared electrode exhibited a maximal specific capacitance of  $236 \text{ F} \cdot \text{g}^{-1}$  measured in a three-electrode cell system. Furthermore, the assembled symmetric supercapacitor showed a specific capacitance of  $195 \text{ F} \cdot \text{g}^{-1}$  at  $0.2 \text{ A} \cdot \text{g}^{-1}$  and a superior specific capacitance retention of about 93% after 15000 cycles. The desirable capacitive behavior suggests that *Pleurotus eryngii* is an attractive biomass source of carbon materials for the potential supercapacitor applications.

## 1. Introduction

A supercapacitor is considered a promising energy storage device due to its unique merits of high specific power, high cycle stability, and rapid charge-discharge performance [1]. Owing to these features, a supercapacitor has been widely involved in various application fields, such as electric vehicles, consumer electronics, and industrial energy management [2, 3].

A large amount of electrode materials for supercapacitors has been investigated so far, including carbon materials [4–6], metal oxides [7, 8], and conducting polymers [9, 10]. In recent years, two-dimensional (2D) nanomaterials [11] and hybrid materials [12] have attracted great interests. However, the synthesis of 2D nanosheets and hybrid materials is commonly involved with methods like arc-discharge synthesis, chemical vapor deposition, and microwave radiation, which are expensive, complicated, and sometimes

harmful to the environment [13–15]. Now, the trend is to use biomass as a convenient and economical method for supercapacitors. Porous carbon material derived from biomass is regarded as one of the most promising candidates due to its high surface areas, good electrical conductivity, low cost, and renewability [16, 17].

Recently, varieties of natural biomass have been utilized as starting materials to prepare porous carbon materials for supercapacitor [18–20]. It was reported that willow catkins activated by KOH present large three-dimensional interconnected micrometer-level pores composed of sheet-like primary particles [20]. Five types of tea leaves prepared by high-temperature carbonization and activation with KOH show typical amorphous and porous structures with a high specific surface [21]. Furthermore, N-doped porous carbon microsphere materials, synthesized from fermented rice, offer high porosity and high capacitance [22].

Mushrooms, rich in carbon and oxygen, are widely distributed around the world. They are abundant, economical, and environmentally friendly. In this regard, many kinds of mushrooms have been used in supercapacitor applications [23, 24]. *Pleurotus eryngii*, a kind of mushrooms, has been commercially produced by the industrial process for decades with a considerable yield. This endows the *Pleurotus eryngii* with low price which helps it stand out among other biomass resources. Here, we reported a new facile way to synthesize the electrode materials with *Pleurotus eryngii* as a precursor.

In this work, a facile fabrication of porous activated carbons derived from *Pleurotus eryngii*, followed by carbonization and KOH activation, has been demonstrated. The obtained materials present a high specific surface area of  $3255 \text{ m}^2 \cdot \text{g}^{-1}$ . In a three-electrode cell system, the prepared electrode offers a maximal specific capacitance of  $236 \text{ F} \cdot \text{g}^{-1}$ . Furthermore, the assembled symmetric supercapacitor shows a specific capacitance of  $195 \text{ F} \cdot \text{g}^{-1}$  at  $0.2 \text{ A} \cdot \text{g}^{-1}$  and a superior specific capacitance retention of about 93% after 15000 cycles. This work highlights the attractive features of *Pleurotus eryngii* in a supercapacitor which might inspire their future development in new energy storage device prototypes.

## 2. Experiments

**2.1. Material Synthesis.** *Pleurotus eryngii* was firstly washed with ethanol and dried at  $60^\circ\text{C}$  overnight. Secondly, the dried *Pleurotus eryngii* was carbonized under a nitrogen atmosphere at  $500^\circ\text{C}$  for 12 hours. And then, the carbonized *Pleurotus eryngii* was mixed with KOH solution in a 1:3 weight ratio and dried at  $120^\circ\text{C}$  overnight in a vacuum oven. The mixture was subsequently activated under a nitrogen atmosphere at 600, 700, and  $800^\circ\text{C}$ , respectively. Finally, the activated sample was washed with hydrochloric acid solution and excessive distilled water to remove the impurities. The products were denoted as APE-*X*, where *X* was the activation temperature.

**2.2. Material Characterization.** The samples were examined under a scanning electron microscope (SEM, Hitachi S4700). The morphology images were recorded on a transmission electron microscope (TEM, FEI Tecnai G2 F20 S-twin TEM system). X-ray diffraction (XRD) patterns were measured on a Bruker D8 ADVANCE diffractometer. Raman spectra were examined by a Renishaw inVia Raman microscope. X-ray photoelectron spectroscopy (XPS) analysis was carried out on a Thermo Scientific XPS system. Specific surface areas of the samples were measured by the Brunauer-Emmett-Teller (BET) method on a Beishide 3H-2000PS2 specific surface and pore size analysis instrument.

**2.3. Electrochemical Measurements.** The electrochemical performance of the active materials was measured in both three-electrode and two-electrode systems with 6 M KOH aqueous solution used as the electrolyte. In the three-electrode system, the counter electrode and reference electrode were platinum foil and saturated Ag/AgCl. The working electrode was prepared by mixing the active materials (80 wt%), polyvinylidene fluoride (10 wt%), and carbon black (10 wt%) in a few

drops of N-methyl-2-pyrrolidone solvent. Subsequently, the resulting mixture was coated on a nickel foam substrate and dried at  $80^\circ\text{C}$  vacuum for 24 hours [25]. The mass loading of the active material for each electrode was about  $5 \text{ mg} \cdot \text{cm}^{-2}$ . In the two-electrode system, the symmetric supercapacitor was assembled by employing two APE-700 electrodes with a separator. The cyclic voltammetry (CV), galvanostatic charge/discharge (GCD), and electrochemical impedance spectroscopy (EIS) measurements were carried out on a Metrohm Autolab PGSTAT302N electrochemical workstation. The specific capacitance  $C_m$  ( $\text{F} \cdot \text{g}^{-1}$ ) was calculated according to the discharge curve by the following equation [18, 26]:

$$C_m = \frac{k I \Delta t}{(m \Delta V)} \quad (1)$$

where  $I$  (A) is the discharge current,  $\Delta t$  (s) is the discharge time,  $\Delta V$  (V) is the discharge voltage window excluding the  $IR$  drop,  $m$  (g) is the mass of active materials in a single electrode, and  $k$  is a constant ( $k = 1$  for a three-electrode system and  $k = 2$  for a two-electrode system).

## 3. Results and Discussions

As shown in the SEM image of Figure 1(a), the *Pleurotus eryngii* presents three-dimensional porous network structure with micrometer-level pores. Figures 1(b) and 1(c) show the carbonized samples with different magnifications. The SEM image of the activated samples at  $700^\circ\text{C}$  is displayed in Figure 1(d). When comparing Figures 1(c) and 1(d), it is found that a higher roughness is observed on the surface of the activated samples after KOH activation. The TEM image of APE-700 as shown in Figure 2(a) indicates that numerous nanoparticles are stacked each other in different directions aggregating on the rough surface of the activated samples (Figure 1(d)). A high-resolution TEM (Figure 2(b)) image from APE-700 reveals that less than 1 nm abundant micropores are created after the activation.

The XRD patterns of various temperature-activated samples are shown in Figure 3(a). All the APE samples exhibit two broad- and low-intensity peaks near  $25^\circ$  and  $43^\circ$ , corresponding to (002) and (100) planes of the graphite [25, 27]. The intensity of these two peaks decreases as the activation temperature increases, probably due to a lower graphitization degree [20]. Figures 3(b)–3(d) are the Raman spectra of APEs. Two broad bands centered at  $1350 \text{ cm}^{-1}$  (D-band) and  $1584 \text{ cm}^{-1}$  (G-band) are clearly observed [20, 25]. The relative intensity ratios of D-band to G-band ( $I_D/I_G$ ) of APE-600, APE-700, and APE-800 are 2.9, 3.3, and 3.6, respectively. As the D-band is induced by the defects in the graphite lattice and the G-band is generated by the  $\text{sp}^2$  carbon atomic pair stretching, APE-800 exhibits the lowest graphitization degree [28]. This can be ascribed to the higher temperature facilitating the erosion reaction between carbonaceous material and KOH, which may decrease the graphitization degree of the APE materials. The results are consistent with those of the XRD analysis in Figure 3(a).

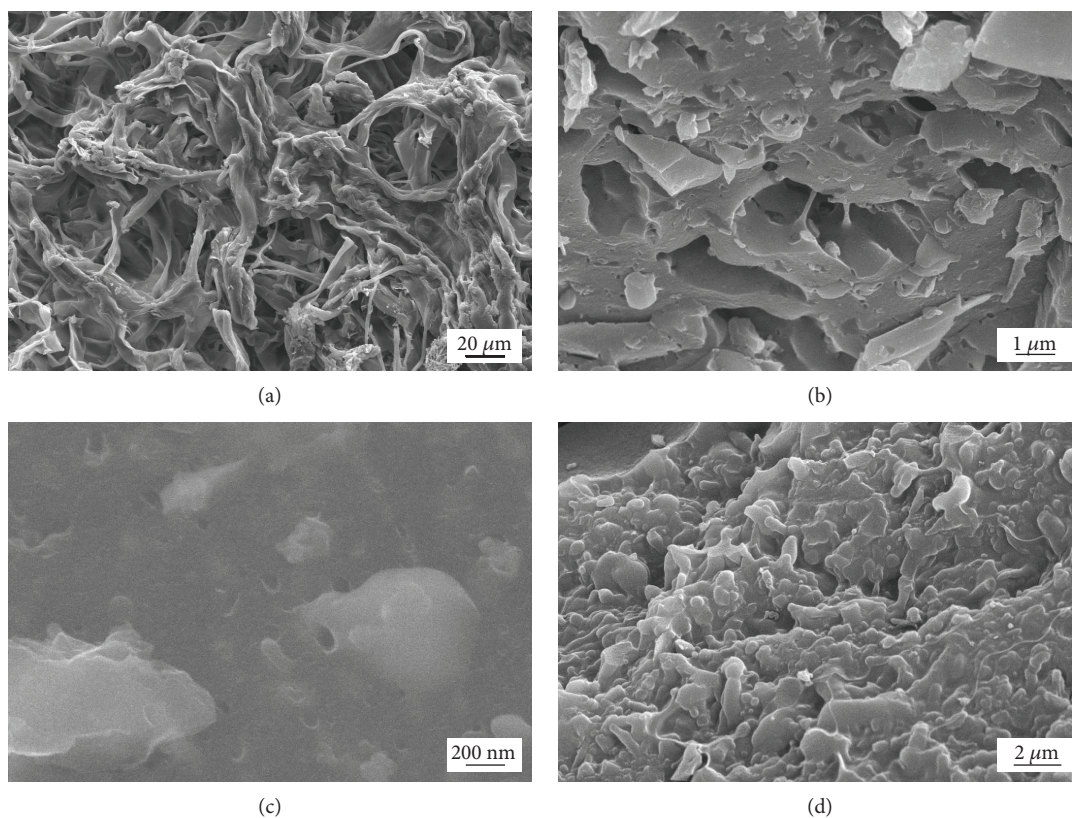


FIGURE 1: SEM images of (a) *Pleurotus eryngii*, (b, c) carbonized *Pleurotus eryngii* with different magnifications, and (d) as-prepared APE-700 electrode sample.

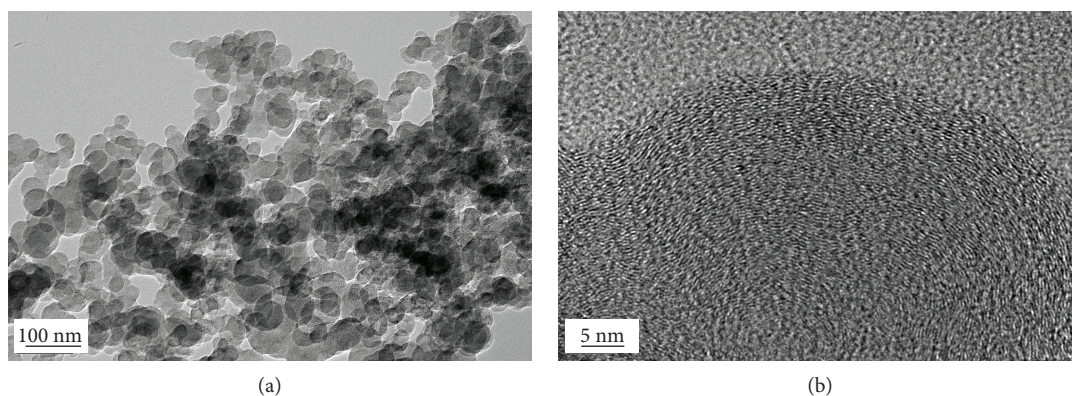


FIGURE 2: (a, b) TEM images of APE-700 with different magnifications.

XPS measurement was used to further confirm the surface chemical properties and atomic compositions of as-prepared APEs. The wide XPS spectra in Figure 4(a) display two peaks at 284 and 533 eV, corresponding to C 1s and O 1s, respectively. There are oxygen-containing functional groups in all the activated samples [25]. The atomic percentage of oxygen decreases from 17.33 to 8.91 atom% (see Table 1) when the activation temperature has been changed from 600°C to 800°C. The C 1s spectra of APEs in Figures 4(b)–4(d) could be approximately fitted into three peaks, which can be assigned to  $sp^2$  C=C bond in graphitic carbon

(284.6 eV),  $sp^3$  C-C hybridization (285.4 eV), and -C=O/-COO- bond (288.6 eV) [25, 29]. The relative intensity of  $sp^3$  C-C hybridization peaks (the purple peaks in Figures 4(b)–4(d)) increases as the temperature raises from 600 to 800°C. The increasing intensity in the C-C bond corresponds to the reduction of the graphitization degree for APE samples at higher temperature. The most probable reason is that the KOH is more reactive with carbonaceous materials, which causes more lattice defects in the activation process.

The nitrogen adsorption-desorption isotherms of APEs activated at 600°C, 700°C, and 800°C are shown in

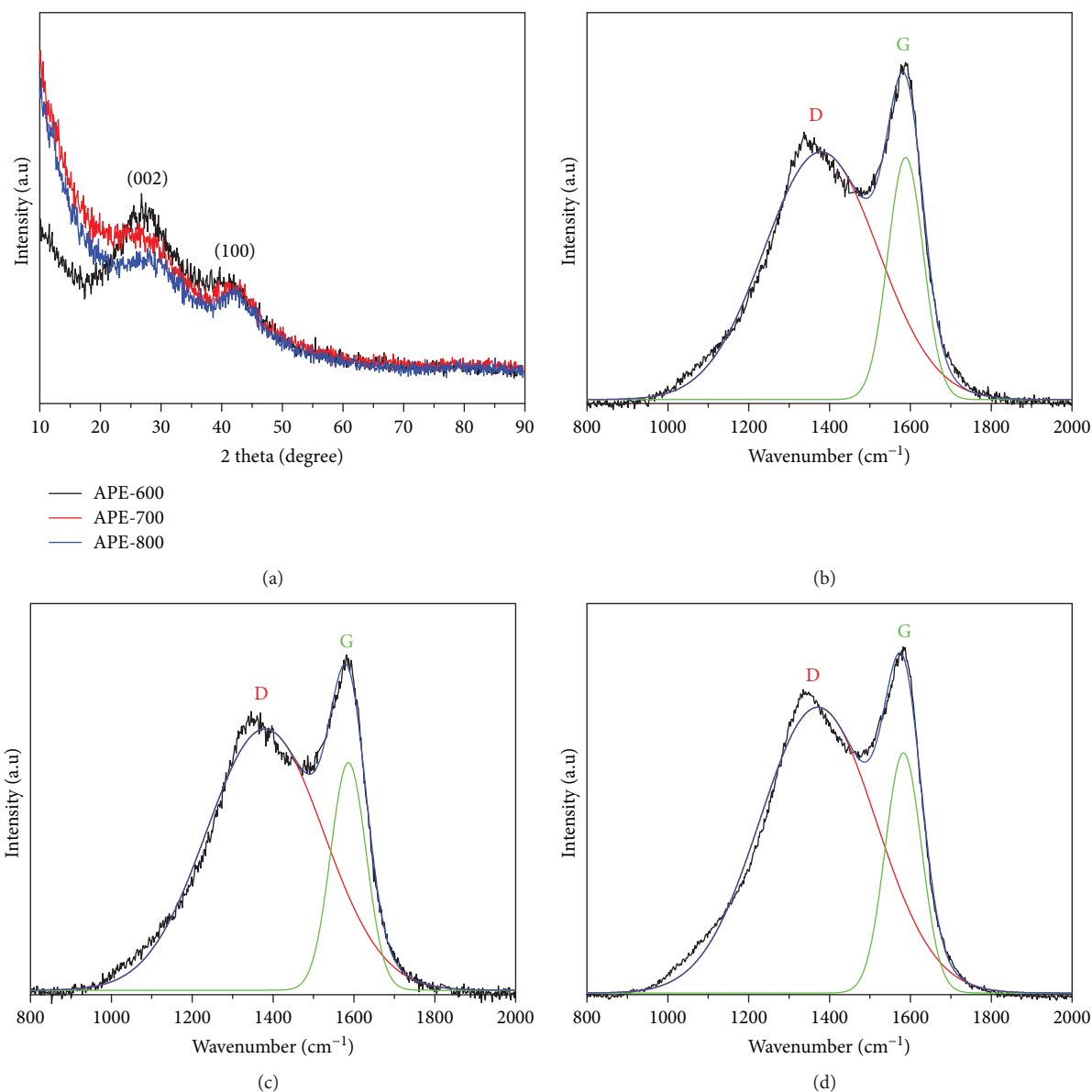
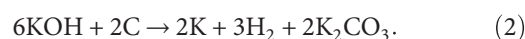


FIGURE 3: (a) XRD patterns of APEs obtained at various activation temperatures. Raman spectra of APE-600 (b), APE-700 (c), and APE-800 (d).

Figure 5(a). An abrupt increase occurs at very low relative pressure (less than 0.1) according to isotherms, followed by a smooth increase at the high relative pressures. From those results, it implies that the APEs have abundant micropores with a narrow pore size distribution [30]. At the relative pressures from 0.4 to 1.0, the subtle hysteresis loops provide evidence for forming a small amount of mesopores in the samples [31].

When the activation temperatures increase from 600°C to 700°C, the flat plateau of the isotherms, as shown in Figure 5(a), moves to a higher position, revealing that more pores are produced and, as a result, a higher specific surface area is achieved [32]. However, it can be noted that the plateau is shifted down when increasing the activation temperature to 800°C. A collapse of the pore structure may probably happen due to the excessive temperature. The total

BET specific surface area of APE-700 is 3255 m<sup>2</sup>·g<sup>-1</sup> with respect to 2253 m<sup>2</sup>·g<sup>-1</sup> for APE-600 and 2704 m<sup>2</sup>·g<sup>-1</sup> for APE-800. The mechanism of KOH activation is shown in the following equation [23, 33]:



During the KOH activation process, the carbon frameworks are etched by the redox reaction. After washing, metallic K and K compounds are removed and pores are created.

The pore size distribution of the APEs measured by the H-K model (supplied by the Beishide 3H-2000PS2 specific surface and pore size analysis instrument) is shown in Figure 5(b). The pore size of the APEs is mainly at a range of 0.5–1.0 nm, implying that massive micropores are present in the APEs. In the aqueous solution of KOH, the micropores

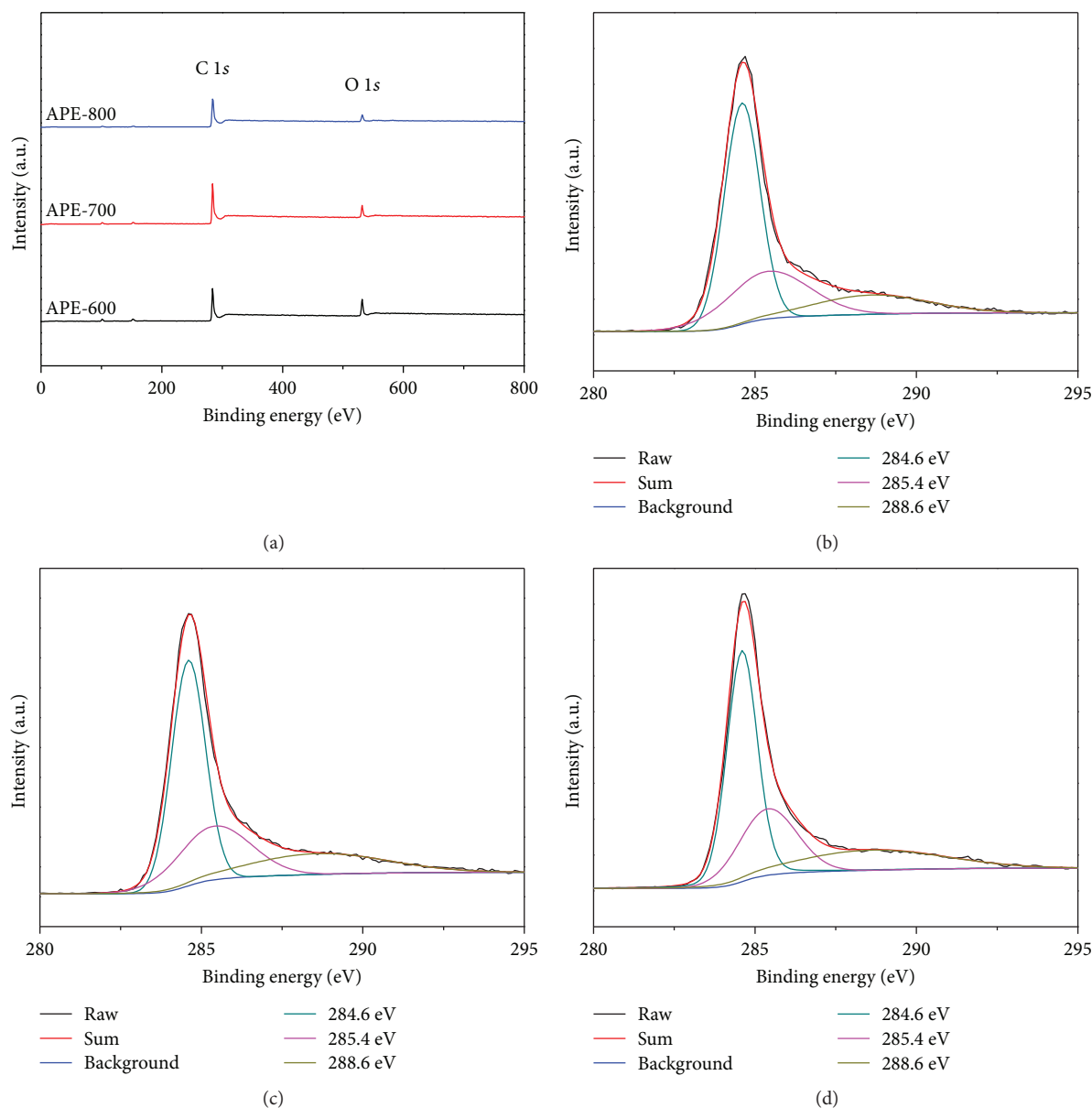


FIGURE 4: (a) XPS spectra of APEs activated at different temperatures. High-resolution C 1s spectra of APE activated at 600°C (b), 700°C (c), and 800°C (d).

TABLE 1: Chemical compositions of as-prepared APEs by XPS analysis.

Element	APE-600	APE-700	APE-800
C (atom%)	82.67	88.96	91.09
O (atom%)	17.33	11.04	8.91

with pore sizes larger than 2 nm are commonly considered too wide to form the double layer while pore sizes less than 0.5 nm are too small for the process [20]. Therefore, it is expected that the pore size of the APEs activated at different temperatures is suitable for the transport of electrolyte ions.

Typical CV curves of the samples with different activation temperatures at the scan rate of  $50 \text{ mV}\cdot\text{s}^{-1}$  are shown

in Figure 6(a). It is clear that all CV curves display rectangular-like shapes with a characteristic feature of a good capacitor behavior, promising to be used as the electrode material of supercapacitors. Figure 6(b) presents the GCD curves of APEs measured at a current density of  $2 \text{ A}\cdot\text{g}^{-1}$ . It is found that the APE-700 has the largest integrated area in the CV curves and the longest charge-discharge time, suggesting the highest specific capacitance for APE-700. Its specific capacitance is calculated as  $236 \text{ F}\cdot\text{g}^{-1}$ . The Nyquist plots of APEs measured from 10 mHz to 100 kHz are shown in Figure 6(c). APEs display good capacitive behavior with a nearly vertical line at low frequencies, among which the slopes are much larger when the activation temperature decreases. At high frequencies, the intercept of plots with the real axis presents a low equivalent serial

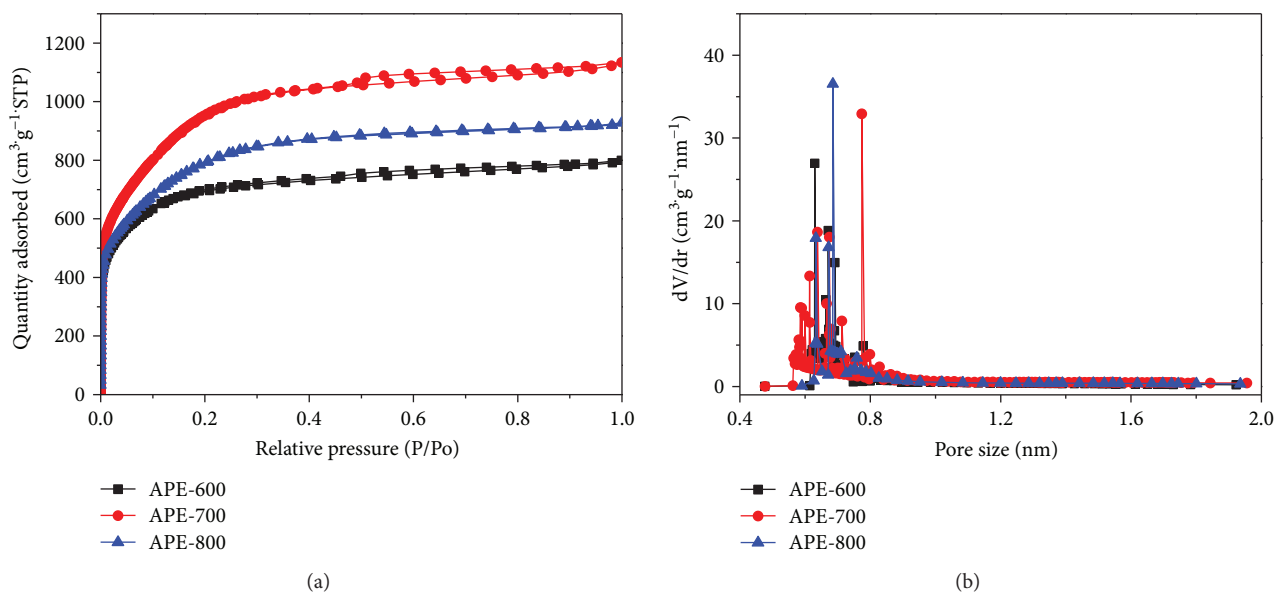


FIGURE 5: (a) Nitrogen adsorption-desorption isotherms of APEs activated at 600°C, 700°C, and 800°C, respectively. (b) Pore size distribution curves of the APEs.

internal resistance of  $\sim 0.3 \Omega$ , including the intrinsic resistance of activated materials, electrolyte and the contact resistance. The bode phase diagrams of all samples are shown in Figure 6(d). Compared with APE-800, the phase angles of APE-600 and APE-700 are  $\sim 85^\circ$  and  $\sim 81^\circ$ , respectively, which are closed to that of an ideal capacity ( $90^\circ$ ), indicating a good capacitive property.

The electrochemistry properties of APE-700 have been investigated further in more detail. The CV curves of APE-700 are presented in Figure 6(e) at scan rates from 5 to  $100 \text{ mV}\cdot\text{s}^{-1}$ . The rectangular-like shape is maintained even at a high scan rate of  $100 \text{ mV}\cdot\text{s}^{-1}$ , revealing low equivalent series resistance and fast charge transport capability [34]. The GCD curves of APE-700 (Figure 6(f)) show almost symmetrical and linear relationship at a series of current densities ranging from 2 to  $20 \text{ A}\cdot\text{g}^{-1}$ , which agreed well to a typical property of electrical double-layer capacitors. However, the rate capability of APE-700 is not high, due to abundant micropores and a small amount of mesopores generated by KOH activation. In general, at low current density, the ions of electrolyte are able to penetrate into the micropores. When the current density increases, the narrow micropores may hinder or restrict the ion diffusion due to the space limitations, leading to a moderate rate capability [1, 35].

Table 2 summarizes a comparison of our result with other biomass-derived carbon materials reported previously. It seems that the APE-700 presents a moderate specific capacitance due to its highest surface area. The main reasons are probably as follows: firstly, the specific capacitance is related not only to the surface area but also to the pore structure, interfacial wettability, and electrical conductivity. Secondly, the measurement and electrolyte of the materials listed in Table 2 are not exactly the same. In particular, the specific capacitance would decay when the current density increases.

In order to investigate the practical electrochemical performance of APE-700, the symmetric supercapacitor was assembled and measured in 6M KOH electrolyte. The CV and GCD curves are shown in Figures 7(a) and 7(b). Good capacitive behaviors at different scan rates and current densities are seen. According to (1), the specific capacitance of APE-700 is calculated as  $195 \text{ F}\cdot\text{g}^{-1}$  at a current density of  $0.2 \text{ A}\cdot\text{g}^{-1}$ . Furthermore, the cycling stability of APE-700 was performed by the GCD test at a constant density of  $2 \text{ A}\cdot\text{g}^{-1}$ . As shown in Figure 7(c), the specific capacitance retention is about 93% with a slight fluctuation after 15000 cycles, exhibiting excellent long-term cycle stability and great potential for energy storage devices.

Figure 7(d) shows the electrochemical impedance spectra of APE-700. It is noted that the equivalent serial internal resistance increases after 15000 cycles, which may be attributed to the abscission of the activated material or the variation of oxygen-containing functional groups. The semicircle loop (nearly  $1 \Omega$ ), an indicator of the charge-transfer resistance between electrolytes and electrode, represents good and stable ionic conductivity of the two samples. The SEM images of APE-700 before and after the cyclic stability test are shown in Figures 8(a) and 8(b). No obvious difference is observed between the two samples.

In summary, *Pleurotus eryngii* activated at 700°C presents a high electrochemistry performance, which may be attributed to the following properties: (a) high specific surface area, which is much more favored to form considerable electrochemical double layers; (b) suitable pore size, which could facilitate ion transport resulting in an effective improvement in the charge-discharge process; (c) high graphitization degree, leading to a good electrical conductivity; and (d) the existence of oxygen-containing functional groups, which not only provides extra pseudo-capacitance but also improves the hydrophilicity and wettability of the porous carbon materials.

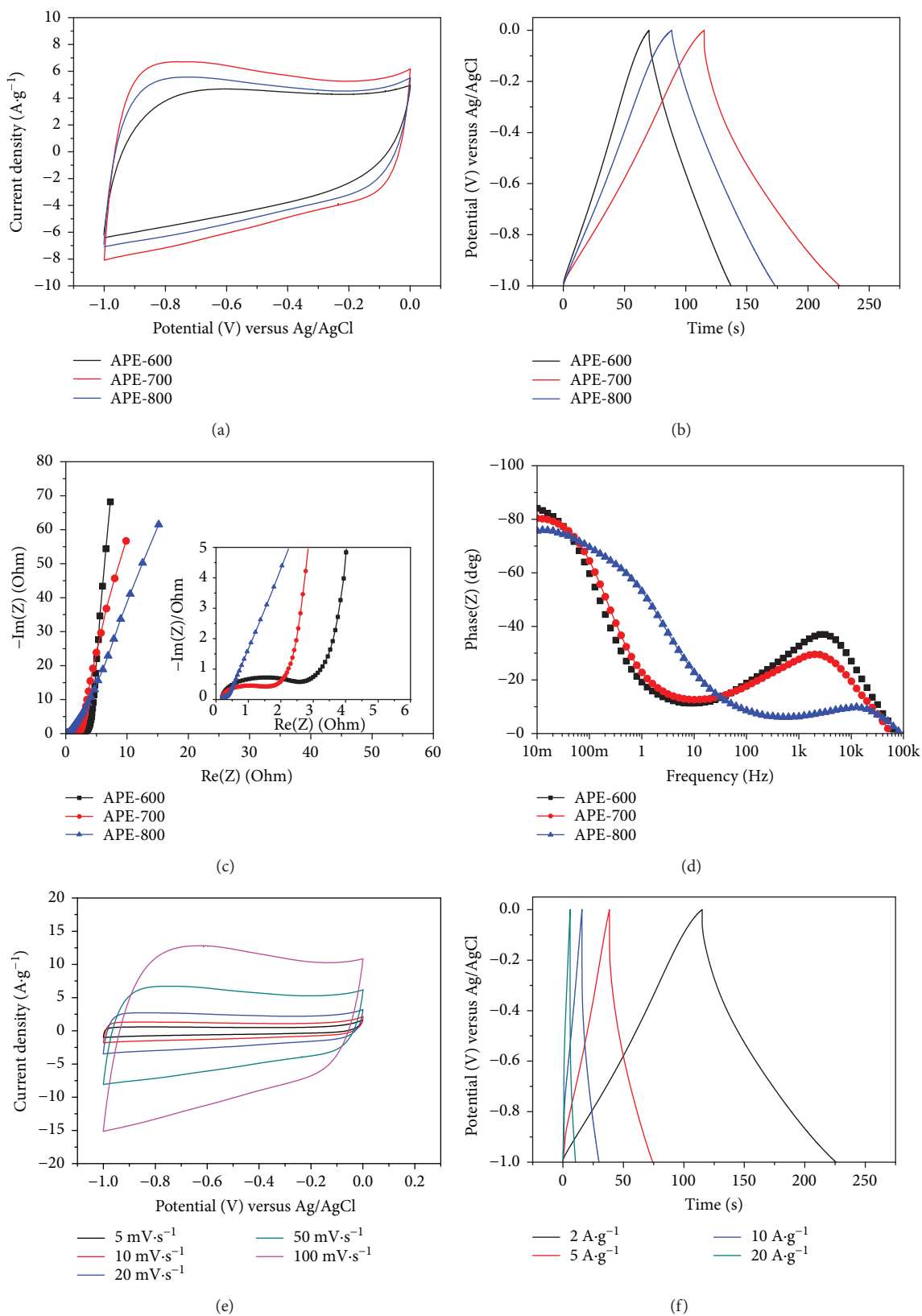


FIGURE 6: Electrochemical performance measured in a three-electrode system: (a) CV curves of APEs activated at 600°C, 700°C, and 800°C, respectively, at  $50 \text{ mV}\cdot\text{s}^{-1}$ ; (b) GCD curves of the APEs at  $2 \text{ A}\cdot\text{g}^{-1}$ ; (c) Nyquist plots of the APEs, an enlarged view in the high-frequency region is shown in the inset; (d) bode phase diagrams of the APEs; (e) CV curves of APE-700 at different scan rates from 5 to  $100 \text{ mV}\cdot\text{s}^{-1}$ ; (f) GCD curves of APE-700 at different current densities from 2 to  $20 \text{ A}\cdot\text{g}^{-1}$ .

TABLE 2: Comparison of the properties of biomass-derived carbon materials.

Biomass	$S_{\text{BET}}$ ( $\text{m}^2 \cdot \text{g}^{-1}$ )	$C_m$ ( $\text{F} \cdot \text{g}^{-1}$ )	Measurement	Electrolyte	Ref.
Willow catkins	1533	298	$0.5 \text{ A} \cdot \text{g}^{-1}$	6 M KOH	[16]
Tea leave	2841	330	$1 \text{ A} \cdot \text{g}^{-1}$	2 M KOH	[21]
Glucose	757	260	$0.5 \text{ A} \cdot \text{g}^{-1}$	6 M KOH	[17]
Coconut shell	1532	228	$5 \text{ mV} \cdot \text{s}^{-1}$	6 M KOH	[19]
Corn starch	1167	162	$0.625 \text{ A} \cdot \text{g}^{-1}$	6 M KOH	[18]
Cotton	1085	207	$1 \text{ A} \cdot \text{g}^{-1}$	1 M $\text{H}_2\text{SO}_4$	[28]
Paulownia sawdust	1900	227	$2 \text{ mV} \cdot \text{s}^{-1}$	6 M KOH	[36]
APE-700	3255	236	$2 \text{ A} \cdot \text{g}^{-1}$	6 M KOH	This work

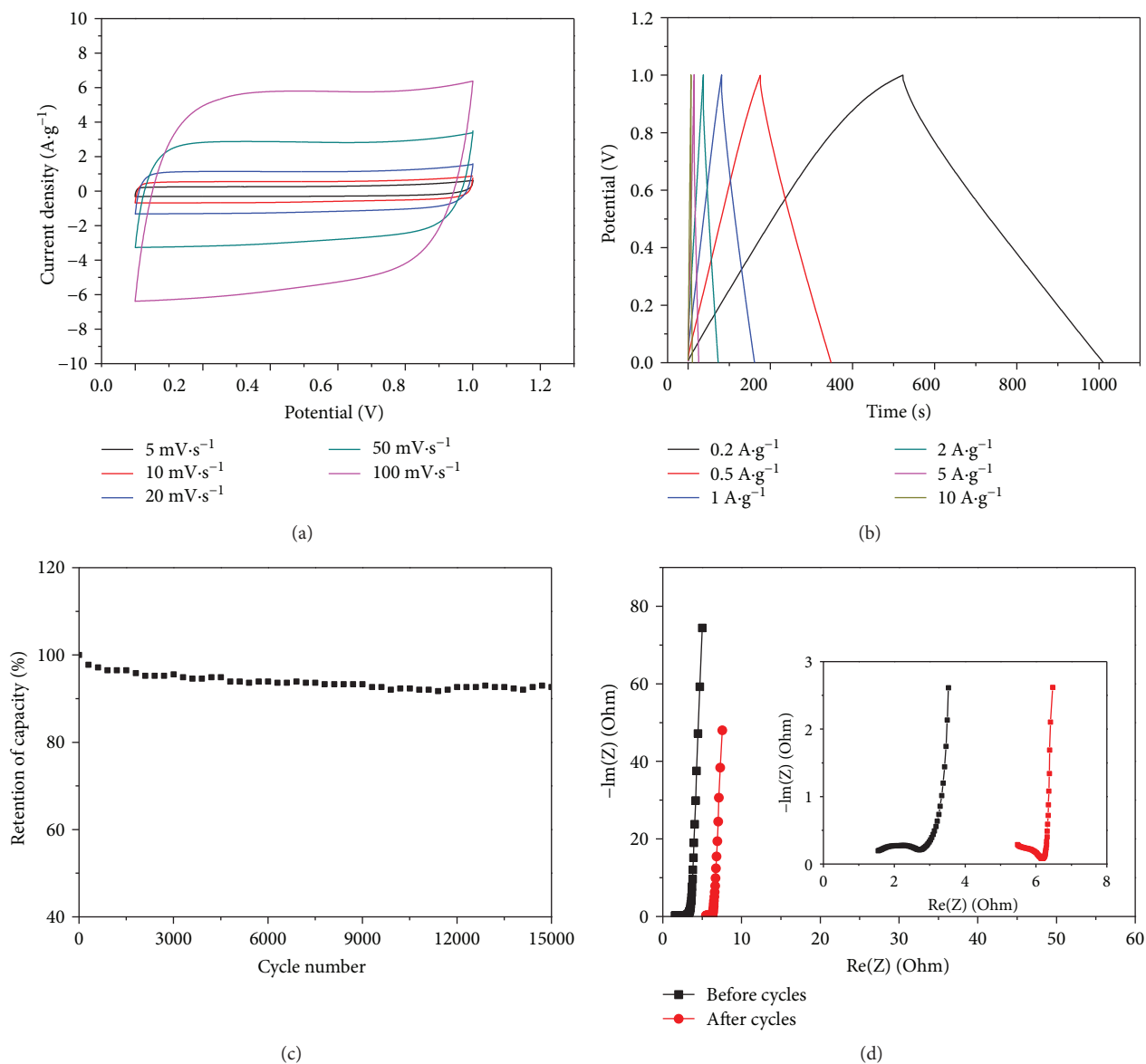


FIGURE 7: Electrochemical performance of APE-700 measured in a two-electrode system: (a) CV curves at different scan rates from 5 to 100  $\text{mV} \cdot \text{s}^{-1}$ ; (b) GCD curves at different current densities from 0.2 to 10  $\text{A} \cdot \text{g}^{-1}$ ; (c) cycle stability at a current density of 2  $\text{A} \cdot \text{g}^{-1}$  in 6 M KOH solution; (d) EIS before and after the cyclic stability test, an enlarged view in the high-frequency region is shown in the inset.

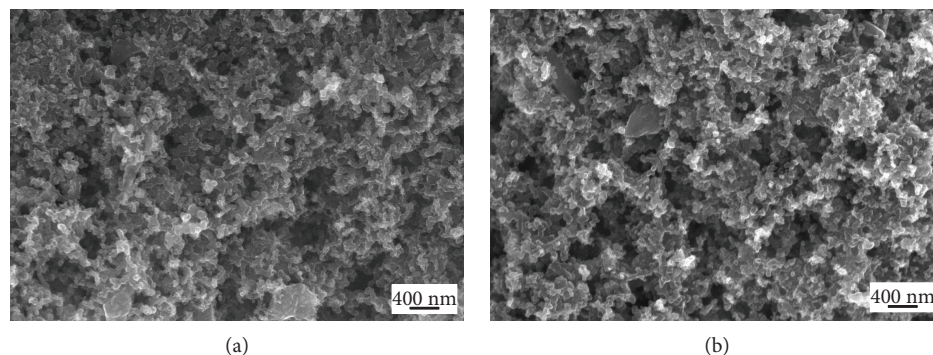


FIGURE 8: SEM images of APE-700 (a) before the cyclic stability test and (b) after the cyclic stability test.

#### 4. Conclusion

Porous activated carbons derived from *Pleurotus eryngii* were synthesized by carbonization firstly and then KOH activation. The porous carbons activated at 700°C, among other activation temperatures, exhibit the highest specific surface area of 3255 m<sup>2</sup>·g<sup>-1</sup>, and the prepared electrode offers a maximal specific capacitance of 236 F·g<sup>-1</sup> measured in a three-electrode cell system. Furthermore, the assembled symmetric supercapacitor shows a specific capacitance of 195 F·g<sup>-1</sup> at 0.2 A·g<sup>-1</sup> and excellent long-term cycle stability with a capacitance retention of 93% after 15000 charge/discharge cycles at a current density of 2 A·g<sup>-1</sup>. This work highlights the attractive capacitive features of the *Pleurotus eryngii* as a readily available biomass source, which might inspire their future development as a new resource of porous activated carbons for supercapacitors and other energy storage devices.

#### Conflicts of Interest

The authors declare that they have no conflicts of interest.

#### Acknowledgments

This work was supported by the National Natural Science Foundation of China (NSFC Grant 21750110441), Jiangsu Human Resource and Social Security Grant (2014-XCL-038), Suzhou Science and Technology Programme (SYG 201623), Suzhou Industrial Park Initiative Platform Development for Suzhou Municipal Key Lab for New Energy Technology (RR0140), Guangdong Research Center for Interfacial Engineering of Functional Materials (201701), Key Program Special Fund in XJTU (KSF-P-02, KSF-A-04, KSF-A-05 and KSF-A-07), and the XJTU Research Development Fund (RDF-14-02-42 and RDF-17-01-13).

#### References

- [1] A. G. Pandolfo and A. F. Hollenkamp, "Carbon properties and their role in supercapacitors," *Journal of Power Sources*, vol. 157, no. 1, pp. 11–27, 2006.
- [2] D. Pech, M. Brunet, H. Durou et al., "Ultra-high-power micrometre-sized supercapacitors based on onion-like carbon," *Nature Nanotechnology*, vol. 5, no. 9, pp. 651–654, 2010.
- [3] A. Nishino, "Capacitors: operating principles, current market and technical trends," *Journal of Power Sources*, vol. 60, no. 2, pp. 137–147, 1996.
- [4] C.-M. Chen, Q. Zhang, C. H. Huang et al., "Macroporous 'bubble' graphene film via template-directed ordered-assembly for high rate supercapacitors," *Chemical Communications*, vol. 48, no. 57, pp. 7149–7151, 2012.
- [5] Y. S. Yun, G. Yoon, K. Kang, and H.-J. Jin, "High-performance supercapacitors based on defect-engineered carbon nanotubes," *Carbon*, vol. 80, pp. 246–254, 2014.
- [6] D. T. Pham, T. H. Lee, D. H. Luong et al., "Carbon nanotube-bridged graphene 3D building blocks for ultrafast compact supercapacitors," *ACS Nano*, vol. 9, no. 2, pp. 2018–2027, 2015.
- [7] Q. Liao, N. Li, S. Jin, G. Yang, and C. Wang, "All-solid-state symmetric supercapacitor based on Co<sub>3</sub>O<sub>4</sub> nanoparticles on vertically aligned graphene," *ACS Nano*, vol. 9, no. 5, pp. 5310–5317, 2015.
- [8] L. Liu, J. Lang, P. Zhang, B. Hu, and X. Yan, "Facile synthesis of Fe<sub>2</sub>O<sub>3</sub> nano-dots @ nitrogen-doped graphene for supercapacitor electrode with ultralong cycle life in KOH electrolyte," *ACS Applied Materials & Interfaces*, vol. 8, no. 14, pp. 9335–9344, 2016.
- [9] S. A. Ansari, H. Fouad, S. G. Ansari, M. P. Sk, and M. H. Cho, "Mechanically exfoliated MoS<sub>2</sub> sheet coupled with conductive polyaniline as a superior supercapacitor electrode material," *Journal of Colloid and Interface Science*, vol. 504, pp. 276–282, 2017.
- [10] L. Ma, R. Liu, H. Niu, M. Zhao, and Y. Huang, "Flexible and freestanding electrode based on polypyrrole/graphene/bacterial cellulose paper for supercapacitor," *Composites Science and Technology*, vol. 137, pp. 87–93, 2016.
- [11] Y. Han, Y. Ge, Y. Chao, C. Wang, and G. G. Wallace, "Recent progress in 2D materials for flexible supercapacitors," *Journal of Energy Chemistry*, vol. 27, no. 1, pp. 57–72, 2018.
- [12] L.-F. Chen, Z.-H. Huang, H.-W. Liang, Q.-F. Guan, and S.-H. Yu, "Bacterial-cellulose-derived carbon nanofiber@MnO<sub>2</sub> and nitrogen-doped carbon nanofiber electrode materials: an asymmetric supercapacitor with high energy and power density," *Advanced Materials*, vol. 25, no. 34, pp. 4746–4752, 2013.
- [13] K. Krishnamoorthy and S. J. Kim, "Mechanochemical preparation of graphene nanosheets and their supercapacitor applications," *Journal of Industrial and Engineering Chemistry*, vol. 32, pp. 39–43, 2015.

- [14] L.-F. Chen, Y. Feng, H.-W. Liang, Z.-Y. Wu, and S.-H. Yu, "Macroscopic-scale three-dimensional carbon nanofiber architectures for electrochemical energy storage devices," *Advanced Energy Materials*, vol. 7, no. 23, article 1700826, 2017.
- [15] J. Deng, M. Li, and Y. Wang, "Biomass-derived carbon: synthesis and applications in energy storage and conversion," *Green Chemistry*, vol. 18, no. 18, pp. 4824–4854, 2016.
- [16] Y. Li, G. Wang, T. Wei, Z. Fan, and P. Yan, "Nitrogen and sulfur co-doped porous carbon nanosheets derived from willow catkin for supercapacitors," *Nano Energy*, vol. 19, pp. 165–175, 2016.
- [17] J. Wang, L. Shen, B. Ding et al., "Fabrication of porous carbon spheres for high-performance electrochemical capacitors," *RSC Advances*, vol. 4, no. 15, pp. 7538–7544, 2014.
- [18] L. Pang, B. Zou, X. Han, L. Cao, W. Wang, and Y. Guo, "One-step synthesis of high-performance porous carbon from corn starch for supercapacitor," *Materials Letters*, vol. 184, pp. 88–91, 2016.
- [19] J. Mi, X. R. Wang, R. J. Fan, W. H. Qu, and W. C. Li, "Coconut-shell-based porous carbons with a tunable micro/mesopore ratio for high-performance supercapacitors," *Energy & Fuels*, vol. 26, no. 8, pp. 5321–5329, 2012.
- [20] K. Wang, N. Zhao, S. Lei et al., "Promising biomass-based activated carbons derived from willow catkins for high performance supercapacitors," *Electrochimica Acta*, vol. 166, pp. 1–11, 2015.
- [21] C. Peng, X. B. Yan, R. T. Wang, J. W. Lang, Y. J. Ou, and Q. J. Xue, "Promising activated carbons derived from waste tea-leaves and their application in high performance supercapacitors electrodes," *Electrochimica Acta*, vol. 87, pp. 401–408, 2013.
- [22] S. Gao, Y. Chen, H. Fan et al., "Large scale production of biomass-derived N-doped porous carbon spheres for oxygen reduction and supercapacitors," *Journal of Materials Chemistry A*, vol. 2, no. 10, pp. 3317–3324, 2014.
- [23] P. Cheng, S. Gao, P. Zang et al., "Hierarchically porous carbon by activation of shiitake mushroom for capacitive energy storage," *Carbon*, vol. 93, pp. 315–324, 2015.
- [24] P. Yadav, A. Basu, A. Suryawanshi, O. Game, and S. Ogale, "Highly stable laser-scribed flexible planar microsupercapacitor using mushroom derived carbon electrodes," *Advanced Materials Interfaces*, vol. 3, no. 11, article 1600057, 2016.
- [25] L. Yao, G. Yang, P. Han, Z. Tang, and J. Yang, "Three-dimensional beehive-like hierarchical porous polyacrylonitrile-based carbons as a high performance supercapacitor electrodes," *Journal of Power Sources*, vol. 315, pp. 209–217, 2016.
- [26] W. K. Chee, H. N. Lim, Z. Zainal, N. M. Huang, I. Harrison, and Y. Andou, "Flexible graphene-based supercapacitors: a review," *Journal of Physical Chemistry C*, vol. 120, no. 8, pp. 4153–4172, 2016.
- [27] C.-S. Yang, Y. S. Jang, and H. K. Jeong, "Bamboo-based activated carbon for supercapacitor applications," *Current Applied Physics*, vol. 14, no. 12, pp. 1616–1620, 2014.
- [28] L. Li, Q. Zhong, N. D. Kim et al., "Nitrogen-doped carbonized cotton for highly flexible supercapacitors," *Carbon*, vol. 105, pp. 260–267, 2016.
- [29] T. I. T. Okpalugo, P. Papakonstantinou, H. Murphy, J. McLaughlin, and N. M. D. Brown, "High resolution XPS characterization of chemical functionalised MWCNTs and SWCNTs," *Carbon*, vol. 43, no. 1, pp. 153–161, 2005.
- [30] Q. Wang, Q. Cao, X. Wang, B. Jing, H. Kuang, and L. Zhou, "A high-capacity carbon prepared from renewable chicken feather biopolymer for supercapacitors," *Journal of Power Sources*, vol. 225, pp. 101–107, 2013.
- [31] J. Yin, D. Zhang, J. Zhao, X. Wang, H. Zhu, and C. Wang, "Meso- and micro-porous composite carbons derived from humic acid for supercapacitors," *Electrochimica Acta*, vol. 136, pp. 504–512, 2014.
- [32] Z. Hu, M. P. Srinivasan, and Y. Ni, "Preparation of mesoporous high-surface-area activated carbon," *Advanced Materials*, vol. 12, no. 1, pp. 62–65, 2000.
- [33] J. Wang and S. Kaskel, "KOH activation of carbon-based materials for energy storage," *Journal of Materials Chemistry*, vol. 22, no. 45, pp. 23710–23725, 2012.
- [34] J. Zhi, W. Zhao, X. Liu, A. Chen, Z. Liu, and F. Huang, "Highly conductive ordered mesoporous carbon based electrodes decorated by 3D graphene and 1D silver nanowire for flexible supercapacitor," *Advanced Functional Materials*, vol. 24, no. 14, pp. 2013–2019, 2014.
- [35] W. Xing, C. C. Huang, S. P. Zhuo et al., "Hierarchical porous carbons with high performance for supercapacitor electrodes," *Carbon*, vol. 47, no. 7, pp. 1715–1722, 2009.
- [36] X. Liu, M. Zheng, Y. Xiao et al., "Microtube bundle carbon derived from paulownia sawdust for hybrid supercapacitor electrodes," *ACS Applied Materials & Interfaces*, vol. 5, no. 11, pp. 4667–4677, 2013.

## Research Article

# Hierarchical N- and O-Doped Porous Carbon Composites for High-Performance Supercapacitors

Ben-Xue Zou <sup>1,2</sup>, Yan Wang,<sup>1</sup> Xiaodong Huang,<sup>1</sup> and Yanhua Lu <sup>2</sup>

<sup>1</sup>Department of Chemical Engineering, Eastern Liaoning University, Dandong 118001, China

<sup>2</sup>Liaoning Key Laboratory of Functional Textile Materials, Dandong 118001, China

Correspondence should be addressed to Ben-Xue Zou; [benxue\\_dd@163.com](mailto:benxue_dd@163.com) and Yanhua Lu; [yanhualu@aliyun.com](mailto:yanhualu@aliyun.com)

Received 26 December 2017; Revised 27 February 2018; Accepted 27 March 2018; Published 27 June 2018

Academic Editor: Suresh Kannan Balasingam

Copyright © 2018 Ben-Xue Zou et al. This is an open access article distributed under the Creative Commons Attribution License, which permits unrestricted use, distribution, and reproduction in any medium, provided the original work is properly cited.

Hierarchical N- and O-doped porous carbon composites were prepared by hydrothermally assembling of silk fibers with low molecular weight phenolic resin, followed by carbonization and KOH activation process. Silk fibroin is expected to provide nitrogen and oxygen functionalities for the final composite carbon. The introduction of thin layer graphitic structures of low molecular weight phenolic resin-derived carbon offers more abundant structures, low resistance, and hierarchical porosity with a high BET surface area of  $1927 \text{ m}^2 \cdot \text{g}^{-1}$ . The composition and electrochemical properties of the composite carbon have been studied as a function of the annealing temperature for KOH activation process. The obtained carbon composite exhibits high specific capacitance as high as  $330 \text{ F} \cdot \text{g}^{-1}$  ( $1000 \text{ mF} \cdot \text{cm}^{-2}$ ) at  $0.5 \text{ A} \cdot \text{g}^{-1}$ , good rate capability, and excellent cycling stability (91% of capacitance retention after 10000 cycles) in 6 M KOH electrolyte.

## 1. Introduction

Electrochemical capacitors (ECs), also called supercapacitors or ultracapacitors, are considered to be promising devices for high power demand and long cycle life [1–4]. ECs can harvest and release more energy within time less than 10 s and can be used for an almost unlimited number of charge and discharge cycles, which are superior to or distinctive from Li-ion batteries. Thus, ECs are playing important role in the energy storage devices requiring fast burst of energy and back-up of power sources.

Carbon materials have been widely employed as electrodes for ECs because of their fast charge/discharge kinetics, bipolar operational flexibility, and good stability and because of being environmentally friendly [5–8]. It has been demonstrated that the initial material has a significant impact on the formation mechanism, the specific surface area, and the composition of the final carbon materials [9–12]. The different pore size distribution can be obtained by different physical and chemical activation methods using KOH,  $\text{CO}_2$ , or steam as activating agent [13–16]. Kim et al. found that the steam-activated silk carbons have smaller capacitance in gravimetric

unit than that of the KOH-activated silk carbon (with nearly doubled gravimetric capacitance), but the steam-activated silk carbons showed comparable volumetric capacitance to that of the conventional phenolic resin-based carbon prepared by KOH activation [17]. Thus, they suggested that the steam-activated silk carbon was superior to the conventional KOH-activated phenolic resin carbon materials regarding to the production cost. Zhu et al. synthesized a porous carbon by using KOH chemical activation of exfoliated graphite oxide [18]. This carbon electrode exhibited a large surface area of up to  $3100 \text{ m}^2 \cdot \text{g}^{-1}$  and a specific capacitance of  $166 \text{ F} \cdot \text{g}^{-1}$  in BMIM  $\text{BF}_4/\text{AN}$  electrolyte.

Moreover, the modification with heteroatom is an important route to improve the electrochemical performance of carbon materials for ECs [19–22]. Heteroatom doping such as N and O is expected to enhance the surface polarity and the electron-donor affinity and thus improve the interfacial interaction between carbon electrode and electrolyte [23–26]. N and O functionalities can significantly enhance the wettability, hydrophilicity, and compatibility, which are beneficial for the electrolyte ions accessible to the micropores of carbon materials, thus leading to high

power output and rate performance of carbon electrode. They can also give rise to Faradic capacitance through electrochemical redox reactions. N and O functional groups are usually introduced into carbon materials by employing nitrogen- and oxygen-containing compounds as a nitrogen and oxygen dopant. It is generally accepted that using nitrogen-containing polymers such as polyimide, melamine, polyvinylpyridine, polypyrrole, and cyanamide as a nitrogen dopant by direct carbonization process is a simple and controllable method. Lin et al. have recently reported N-doped ordered mesoporous few layer carbons with extraordinary capacitance of  $855 \text{ F}\cdot\text{g}^{-1}$  in aqueous electrolytes for electrochemical energy storage [27]. Wang et al. used urea-modified lignin as raw materials to produce N-doped porous carbon with high specific capacitance and low resistance for electric double-layer capacitors (EDLCs) [28]. Chen et al. explored N-doped graphene by carbonization process of aromatic polyimide films deposited on the surface of graphene by molecular layer deposition [29]. This N-doped graphene exhibited a high specific capacitance of  $290 \text{ F}\cdot\text{g}^{-1}$  at a current density of  $1 \text{ A}\cdot\text{g}^{-1}$  in 6 M KOH electrolyte. Recently, N- and O-codoped carbon materials have been explored for ECs which is expected to produce the synergistic effect and significantly enhance the capacitance performance [23, 30, 31].

In this work, high porosity of N- and O-doped carbon composites was successfully prepared by hydrothermal reaction, carbonization, and KOH activation process, with silk fibers and low molecular weight phenolic resin as carbon sources. The silk fiber networks were used as the matrix to incorporate the low molecular weight phenolic resin during the hydrothermal reaction. The introduction of low molecular weight phenolic resin provides more abundant structures, high conductivity, and hierarchical porosity for carbon composite materials. The further KOH activation process makes the carbon composite larger surface area and hierarchical opened pores. The resulting porous carbon possesses a high specific capacitance of  $330 \text{ F}\cdot\text{g}^{-1}$  and excellent charge and discharge rates with high porosity and high specific surface area.

## 2. Experimental Section

**2.1. Preparation of Hierarchical N- and O-Doped Porous Carbon Composites.** The hierarchical N- and O-doped porous carbon composites were prepared with silk fibroin as starting materials. Firstly, the amount of silk tussah cocoon was immersed in 0.3 M NaOH solution for 24 h to obtain dispersive silk fibroin (SF), followed by washing with deionized water and drying at  $80^\circ\text{C}$  for 2 h. Then, the coating of low molecular weight phenolic resin on silk fibroin (SF/PR) was prepared by hydrothermal reaction similar to our previous report [32]. After that, the composite (SF/PR) was carbonized at  $600^\circ\text{C}$  for 2 h under pure nitrogen atmosphere at a heating rate of  $10^\circ\text{C}/\text{min}$ . The  $\text{N}_2$  flow rate was adjusted 5~10 ml/min. The as-made carbon composite was ground to fine powders and mechanically mixed with 4-fold amount of KOH (weight ratio, KOH/carbon) for chemical activation. The chemical activation process was carried out under a  $\text{N}_2$  atmosphere with tubular furnace individually at  $700^\circ\text{C}$ ,  $800^\circ\text{C}$ , and  $900^\circ\text{C}$  to obtain samples KCP-700, KCP-800,

and KCP-900 for 2 h, respectively. Finally, the obtained carbon samples were placed in 20 ml 0.1 M HCl, stirred for 0.5 h, and washed with deionized water until the pH stabilized at 7.0. To illustrate the advantage of the carbon composite KCP, pure silk fibroin-derived carbon (named as KSW) without coating of phenolic resin was also prepared.

**2.2. Material Characterization.** The morphologies of the samples were observed with field emission scanning electron microscopy (FESEM, Carl Zeiss, Germany) and transmission electron microscopy (TEM, JEM2010-HR, 200 kV). Thermogravimetric analysis (TGA, NETZSCH STA 449 F3, Germany) was carried out from room temperature to  $1000^\circ\text{C}$  at the heating rate of  $30^\circ\text{C}/\text{min}$  under inert atmosphere with Ar. Raman spectra were performed using confocal laser micro Raman spectrometer (HR800UV, HORIBA Jobin Yvon, France) with the excitation wavelength at 633 nm. XPS spectra were recorded on Thermo ESCALAB 250 electron spectrometer using Al  $K\alpha$  radiation (1486.6 eV). The porous structure of the carbon was evaluated by the classical analysis of nitrogen adsorption-desorption isotherms using ASAP 2020 instrument at  $-196^\circ\text{C}$ . The pore-size distributions were calculated via the Dubinin-Astakhov and BJH (Barrett-Joyner-Halenda) methods. The specific surface areas were calculated using Brunauer-Emmett-Teller (BET) equation. The pore volume was obtained from the adsorbed amount at a relative pressure of  $P/P_0 = 0.97$ .

**2.3. Electrochemical Measurements.** Electrochemical experiments were carried out on a CHI660E potentiostat in a three-electrode cell with a platinum plate as the counter electrode and saturated calomel electrode (SCE) as the reference electrode. Carbon cloth was used as the working electrode's current collector. The electrode active materials (including the pure KSW, composites KCP-700, KCP-800, and KCP-900) were firstly separately mixed with carbon colloid at a weight ratio of 3:1 in ethanol. The obtained pastes were then separately coated onto carbon cloth with a working area of  $1.5 \times 1.2 \text{ cm}^2$ . The mass loading of the two electrodes was about 6 mg. Electrochemical capacitive performances of the electrodes were studied by cyclic voltammetry (CV), chronopotentiometry (CP), and electrochemical impedance spectroscopy (EIS) with 6 M KOH electrolyte. EIS spectra were scanned from a frequency range of 100 kHz to 10 MHz with the operating potential of 0 V and the potential amplitude of 5 mV. Symmetric ECs were assembled by using KCP fixed on carbon cloth as two electrodes in 6 M KOH electrolyte solution.

## 3. Results and Discussion

**3.1. Characterization of KCP Carbon Composite.** To determine the carbonization temperature for the initial hydrothermally assembled composite of silk fibers and low molecular phenolic resin (SF/PR), thermogravimetric analysis profiles of the composite SF/PR, as well as the pristine silk fibers (SF), are represented in Figure 1. The original decomposition temperature for SF/PR composite (ca.  $320^\circ\text{C}$ ) is slightly higher than that of the pristine SF (ca.  $294^\circ\text{C}$ ), indicating that

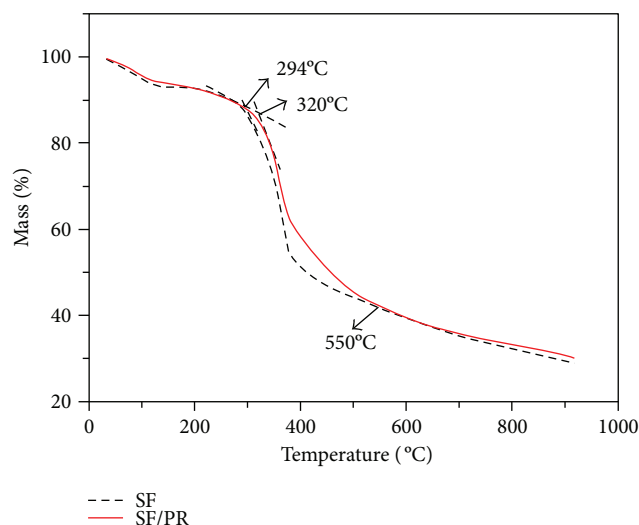


FIGURE 1: Thermogravimetric analysis profiles of pristine SF and SF/PR composite.

the thermal stability of SF/PR composite was enhanced by the introduction of phenolic resin. A drastic weight loss between 320 and 550°C is accompanied by the loss of hydrated water and the decomposition of nitrogen/oxygen functionalities [17]. The weight loss tends to be slow above 550°C, implying that the thermal treatment temperature of 600°C is high enough for the carbonization of the SF/PR composite.

The morphologies of the final KCP sample (derived from the composite SF/PR after carbonization and KOH activation) were examined by FESEM. The typical SEM image results show the final products KCP-800 and KCP-900 have abundant morphologies and microstructures. As shown in Figures 2(a) and 2(b), plenty of pores with different pore size were homogeneously distributed in the honeycomb-like or sponge-like bulk, ranging from micropores (<2 nm) to mesopores (e.g., 2~50 nm) to macropores (e.g., >50 nm). The opened pore size of KCP-800 is smaller than that of KCP-900 by comparing Figures 2(a) and 2(b), indicating the higher activation temperature leads to larger pores in the carbon samples. Figure 2(c) shows much feather duster-like or tree-like structures in the carbon product, which possess axis in the middle of the bulk and split layers with much opened narrow slit. SEM image of Figure 2(d) also presented lamellar structure with plenty of pores between layers. These lamellar platelet structures may be derived from low molecular weight phenolic resin raw materials, which are very different from the silk fiber structures. It should be pointed out that the tree-like or branched structures which are made of mesoporous channels with micropores around different branches have been reported to be possible ideal electrode because these mesopores should be channels for ions in the electrolyte to the abundant number of micropores throughout the electrode [5].

The SEM images clearly present varied microstructures with numerous hierarchical opened pores, which construct a three dimensional (3D) distribution of a porous material. These 3D networks of pores are originated from the thermal treatment process and followed KOH activation process.

During the first carbonization step, micro- and mesopores are generated in the carbon product due to small molecule of gases ( $\text{CO}_x$ ,  $\text{NO}_x$ ,  $\text{H}_2\text{O}$ , etc.) produced and released. The further KOH activation process yields a 3D network of nanoscale pores [30, 33]. The TEM images with a number of light dots presented as Figure 2(e) further corroborate dense pore structures with a distribution of pore sizes between ~1 nm and ~10 nm. And Figure 2(f) illustrates curved graphene-like sheets in the KCP-800 sample, which is desirable for a higher conductivity, higher surface area, and better capacitive performance.

The porous structure of KCP-800 was further confirmed by nitrogen adsorption and desorption measurements. The isotherm, as shown in Figure 3(a), reveals a steep increase of nitrogen adsorption in the initial part of low relative pressure ( $P/P_0 < 0.1$ ), which is attributed to the accessible micropore filling, and the hysteresis loop in the relative high pressure region ( $P/P_0 > 0.4$ ) which is associated with capillary condensation taking place in the mesopores. The isotherm reveals a combined I/IV type isotherm and limiting adsorption over a wide range of  $P/P_0$  which is an indicative of H4 hysteresis loop according to the International Union of Pure and Applied Chemistry (IUPAC) classification [34]. Type H4 loop appears to be associated with narrow slit-like mesopores, and the type I isotherm character is an indicative of microporosity. The BET surface area and total pore volume reached about  $1927 \text{ m}^2 \cdot \text{g}^{-1}$  and  $0.83 \text{ cm}^3 \cdot \text{g}^{-1}$ , respectively, which is expected to provide large contact area and space between the electrode and electrolyte. From the pore-size distribution curve shown in the inset of Figure 3(a), it is evident that the micro- and mesopores less than 5 nm are dominant in the KCP-800 sample. The adsorption average pore width by BET is 3.19 nm, which could be accessible electrochemically for electrolyte solution. The total pore volume is  $\sim 0.83 \text{ cm}^3 \cdot \text{g}^{-1}$ , ranging from the pore size of 1.7 to 300 nm, assuming the hierarchical nanopore structure of KCP-800 sample, which appears to be agreeable to the SEM and TEM results. This hierarchical pore structure with high surface area and pore volume is desirable for charge transfer in low resistance.

For comparison, Figure 3(b) shows the isotherm profiles of single-silk carbon KSW-800, together with its pore-size distribution curve. The low pressure hysteresis is observed extending to the lowest attainable pressures in KSW-800, which is distinct from that of the composite KCP-800. This phenomenon is thought to be associated with the swelling of a nonrigid porous structure or with the irreversible uptake of molecules in pores of about the same width as that of the adsorbate ( $\text{N}_2$ ), implying that the introduction of low molecular weight phenolic resin into the silk fibers may change the mechanism of activation process and thus alter the porous structures of the carbon composite [34]. The pore-size distribution curves indicate the superiority of KCP-800 to single KSW-800 in terms of accumulated pore volume and hierarchical pore-size distribution.

Raman spectroscopy is performed to identify the structure of graphite- and graphene-based species. The Raman spectra (Figure 4(a)) clearly indicated the D band at  $1335 \text{ cm}^{-1}$ , the G band at  $1591 \text{ cm}^{-1}$ , and 2D at  $2700 \text{ cm}^{-1}$ . The D band at  $1335 \text{ cm}^{-1}$  is associated with disordered or functionality-

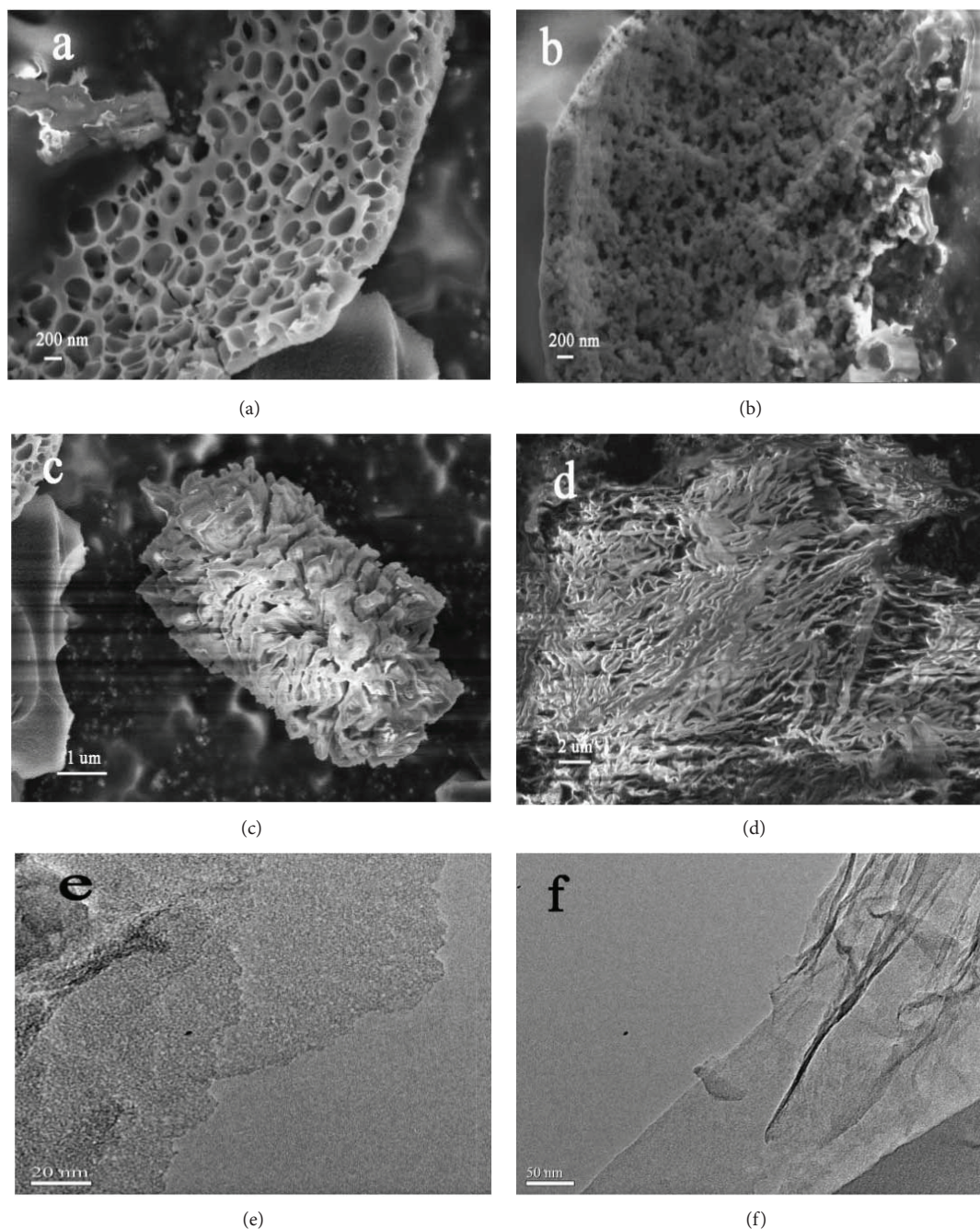


FIGURE 2: (a) Low resolution of SEM for KCP-900. (b–d) Low resolution of SEM for KCP-800. (e, f) High resolution of TEM for KCP-800.

enriched graphite [35]. The high G-band peak at  $1591\text{ cm}^{-1}$  reflects the presence of graphite/graphene structures. The intensity ratio of  $I_G/I_D$  is about 1.0, suggesting that the disordered or functional group-doped graphite coexists with the ordinary graphitic materials [36].

The elemental composition and chemical states were investigated by means of XPS. The XPS survey spectrum shown in Figure 4(b) reveals signals of C, O, and N elements, indicating the presence of oxygen and nitrogen functionalities. XPS analysis results showed that the composition ratio of N/C is about 1.9% and that of O/C is about 16.0%. The involvement of nitrogen and oxygen can dramatically

improve the wettability, hydrophilicity, and compatibility for KCP-800 in the electrolyte solution. These natures, as well as the high porosity, may offer an appreciate reservoir for electrolyte ion transport which will increase the charge-transfer efficiency and create a large capacitance. The C1s spectrum (Figure 4(c)) was deconvoluted into four component peaks at binding energy ca. 284.7 eV for C-C, 284.8 eV for C=C, 285.9 eV for C-N, and 288.6 eV for C-O [36]. The N1s peak as shown in Figure 4(d) can be deconvoluted into two component peaks, namely, pyrrolic N (N-5, 399.9 eV) and quaternary N (N-Q, 400.9 eV) [37]. The presence of the N-Q bond can facilitate the electron transfer and cause

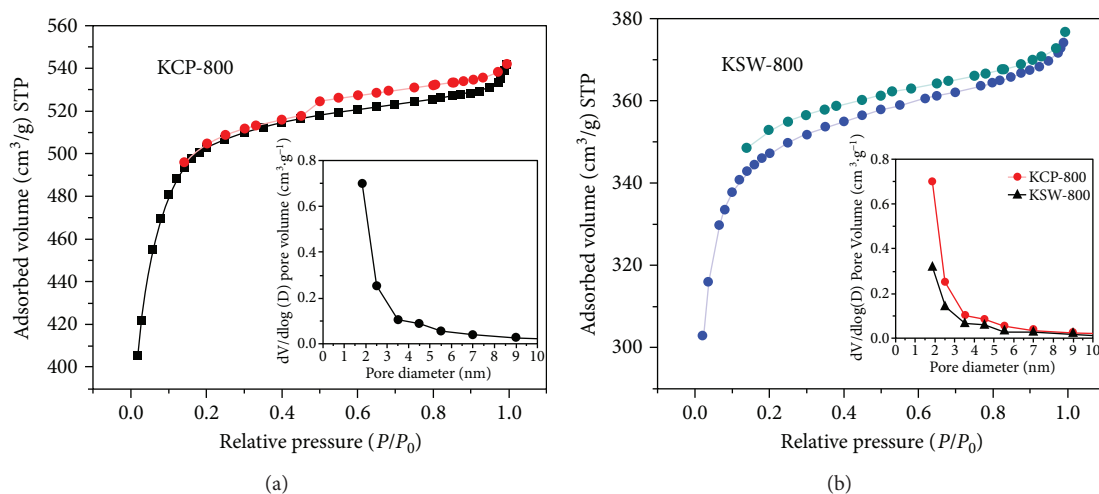


FIGURE 3: (a)  $N_2$  adsorption-desorption isotherms of KCP-800 and pore-size distribution shown inset. (b)  $N_2$  adsorption-desorption isotherms of KSW-800 and pore-size distribution shown inset.

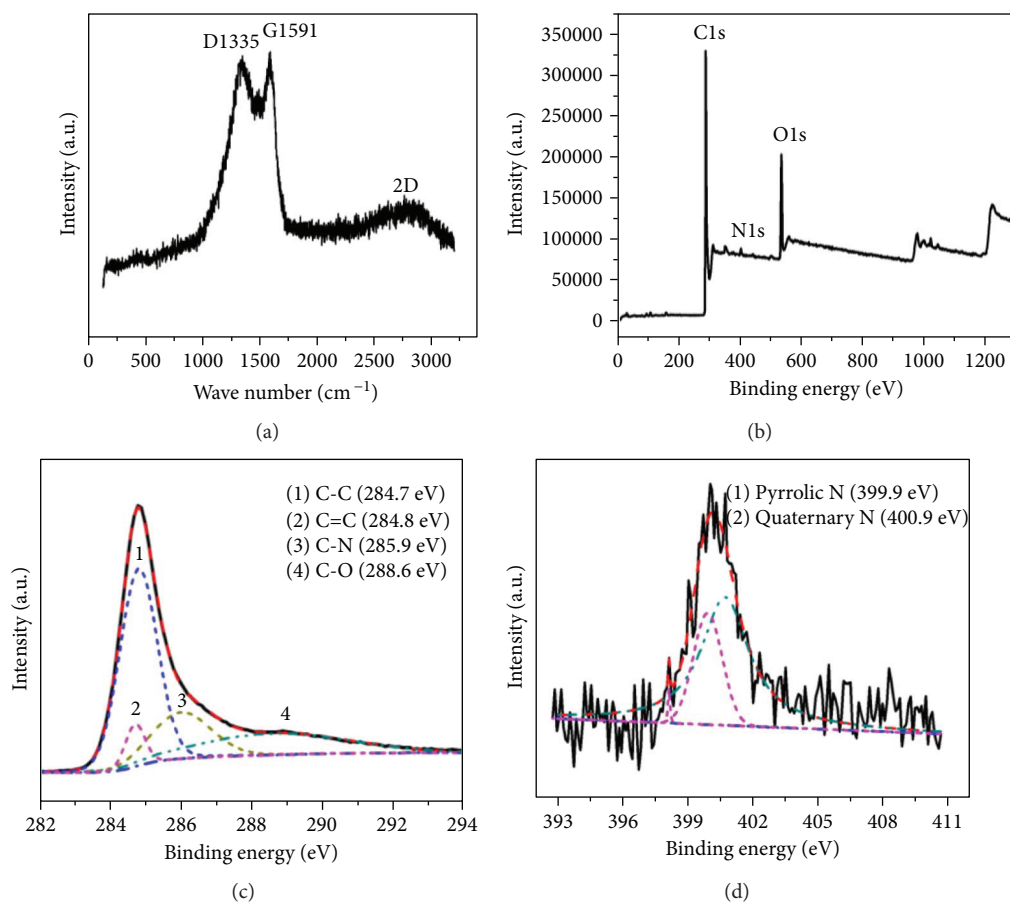


FIGURE 4: (a) Raman spectra of KCP-800. (b) XPS survey spectra of KCP-800. (c-d) High-resolution XPS spectra of deconvoluted C1s and N1s peaks.

the enhancement of the conductivity of carbon materials, which is beneficial for rate and cycling performance of supercapacitors. In addition, the presence of pyrrolic N is assumed to contribute the Faradaic reaction-based pseudocapacitive and thus increase the capacitance performance of the

electrode [38, 39]. The mechanism of redox reaction in acidic electrolyte (e.g.,  $H_2SO_4$ ) for N-doped carbon has been explained by the Lewis base behavior of the nitrogen functionalities on the carbon electrode. The possibilities of redox reactions for N-doped carbon in KOH electrolyte were also

TABLE 1: Porosity parameters and element composition by XPS of the carbon samples.

	Raw materials	Activity temperature (°C)	BET surface area (m <sup>2</sup> /g)	Cumulative volume of pores (cm <sup>3</sup> /g)	N/C content (at.%)	O/C content (at.%)
KCP-700	Silk/LPR	700	911	0.043	3.44	35.9
KCP-800	Silk/LPR	800	1927	0.127	1.9	16.0
KCP-900	Silk/LPR	900	1886	0.160	2.1	16.2
KSW-800	Silk	800	1334	0.082	8.8	22.2

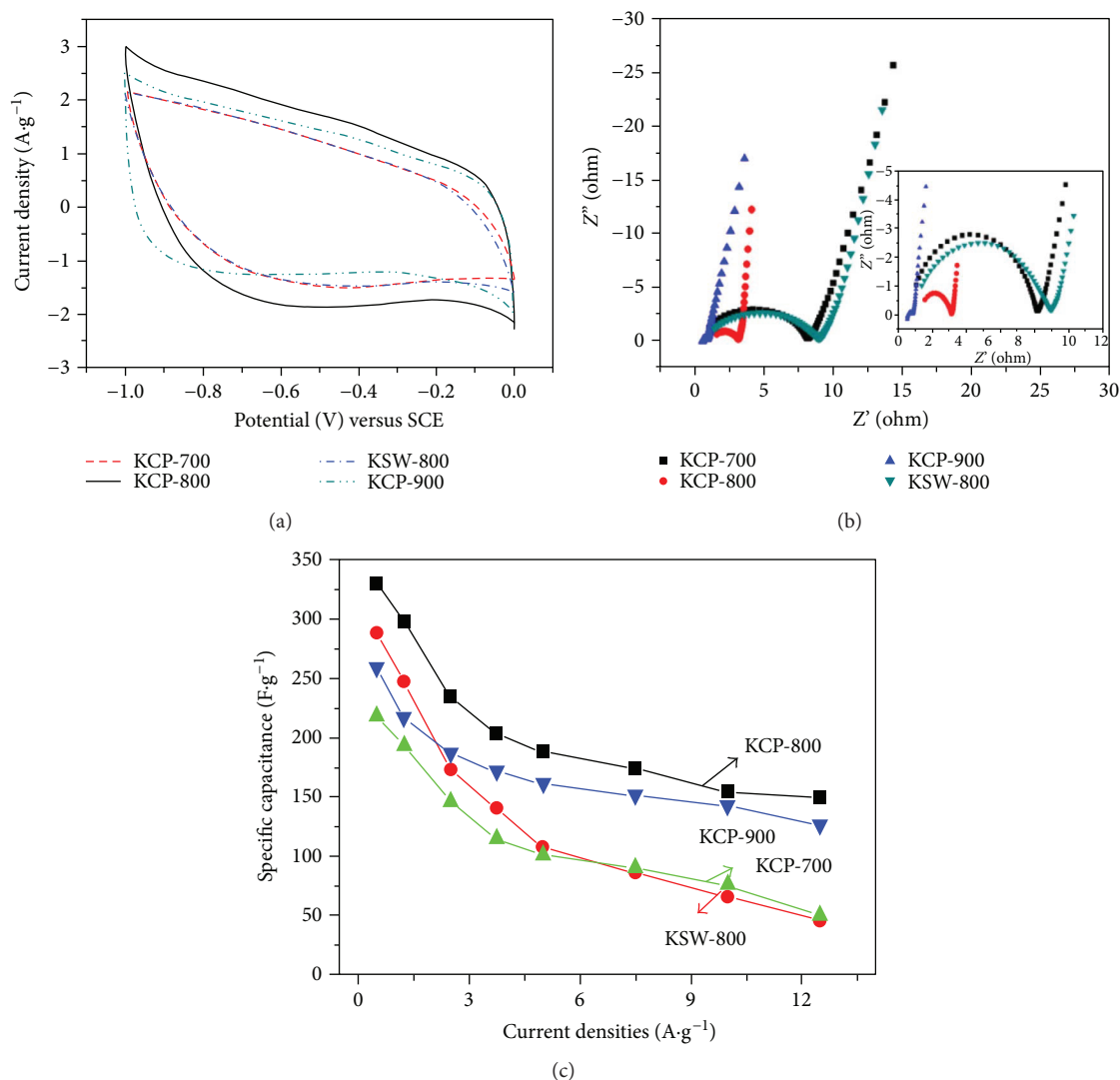


FIGURE 5: (a) CV curves of composites KCP-700, KCP-800, and KCP-900 electrodes and single-silk carbon KSW-800 electrode at 10 mV/s. (b) Nyquist plots for those electrodes measured at 0 V DC potential in the frequency range of 100 kHz to 10 MHz. (c) Specific capacitance of the four samples at different current densities in 6 M KOH electrolyte.

elucidated by previous reports [40]. It was assumed that the pyrrolic N (N-5) can be electrochemical oxidized to pyridone nitrogen (N-5 (OH)) in KOH electrolyte. The pyridone nitrogen atoms are considered as pyridine nitrogen atoms with one adjacent carbon atom that absorbs a hydroxyl group.

The porous structure and chemical composition of carbonaceous materials are summarized in Table 1. These

values are considered to be useful for understanding the relationships of many properties of the carbon materials. The BET surface area and cumulative pore volume of carbon composite KCP-800 are much higher than those of single-silk carbonaceous KSW-800, indicating that the introduction of low molecular weight phenolic resin provides more abundant structures and porosities for carbon composite

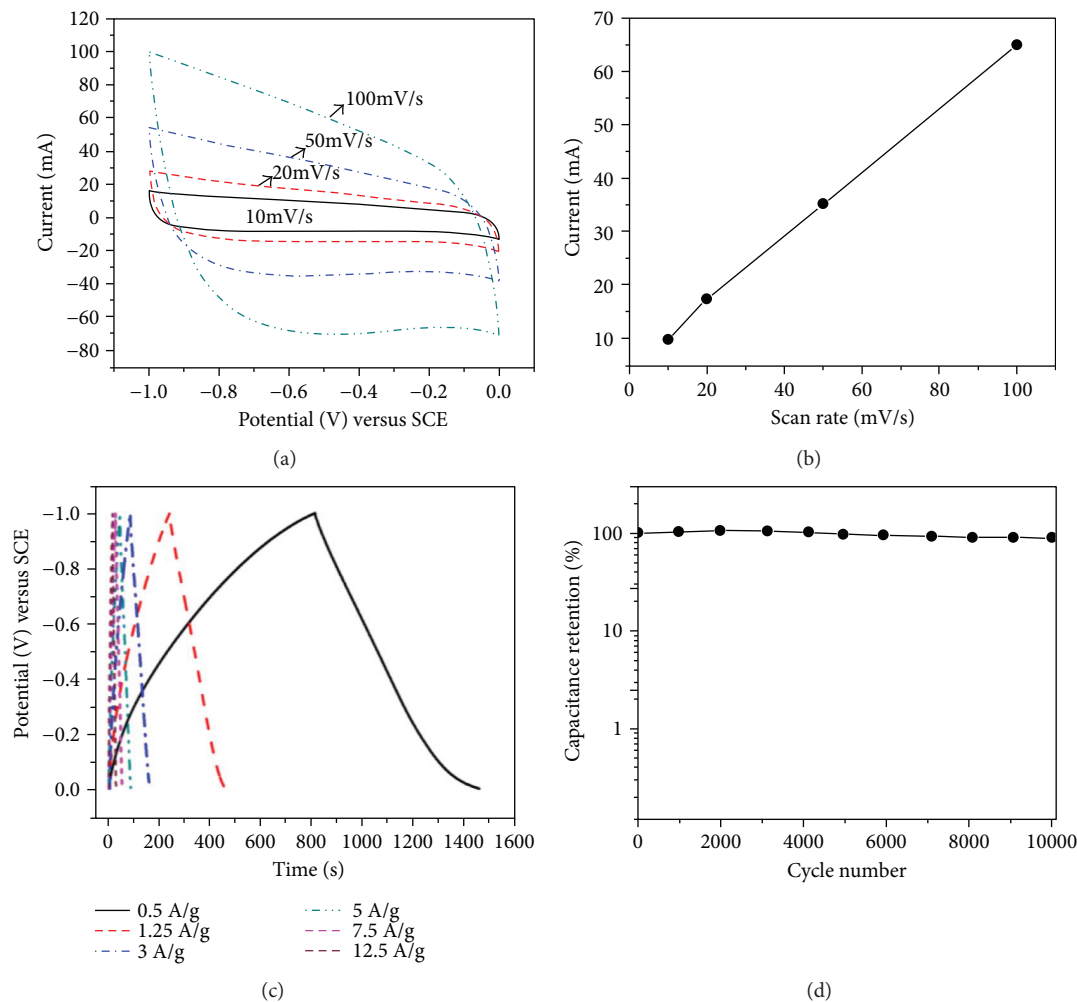


FIGURE 6: (a) CV curves of KCP-800 at various scan rates. (b) The dependence of the discharge current at  $-0.5$  V on scan rate. (c) Galvanostatic charge/discharge profiles at various charge-discharge current densities from  $0.5$  to  $12.5$   $\text{A}\cdot\text{g}^{-1}$ . (d) Capacitive retention of KCP-800 at a current density of  $3$   $\text{A}\cdot\text{g}^{-1}$  over 10000 cycles in  $6$  M KOH electrolyte.

TABLE 2: Comparison of the specific capacitance of carbon-based electrode in the literature.

Materials	Specific capacitance	Area capacitance	Reference
N-doped ordered mesoporous carbon	$227 \text{ F}\cdot\text{g}^{-1}$ ( $0.2 \text{ A}\cdot\text{g}^{-1}$ )		[12]
P-doped carbon	$133 \text{ F}\cdot\text{g}^{-1}$ ( $10 \text{ A}\cdot\text{g}^{-1}$ )	$146 \text{ mF}\cdot\text{cm}^{-2}$	[19]
N-doped graphene	$286 \text{ F}\cdot\text{g}^{-1}$ ( $0.5 \text{ A}\cdot\text{g}^{-1}$ )		[21]
N- and O-doped 3D porous carbon	$318 \text{ F}\cdot\text{g}^{-1}$ ( $0.5 \text{ A}\cdot\text{g}^{-1}$ )		[30]
N- and O-doped carbon	$302 \text{ F}\cdot\text{g}^{-1}$ ( $5 \text{ A}\cdot\text{g}^{-1}$ )		[31]
Porous carbon	$255 \text{ F}\cdot\text{g}^{-1}$ ( $0.5 \text{ A}\cdot\text{g}^{-1}$ )		[35]
N-doped graphene	$324 \text{ F}\cdot\text{g}^{-1}$ ( $0.5 \text{ A}\cdot\text{g}^{-1}$ )		[36]
CVT-on-VG	$278 \text{ F}\cdot\text{g}^{-1}$ ( $10 \text{ mV}^{-1}$ )	$36 \text{ mF}\cdot\text{cm}^{-2}$	[43]
Porous carbon	$296.2 \text{ F}\cdot\text{g}^{-1}$ ( $0.05 \text{ A}\cdot\text{g}^{-1}$ )		[44]
Porous N-doped carbon	$330 \text{ F}\cdot\text{g}^{-1}$ ( $0.5 \text{ A}\cdot\text{g}^{-1}$ )	$1000 \text{ mF}\cdot\text{cm}^{-2}$	This work

materials. Moreover, the activated carbon composite KCP-800 shows the highest BET surface area and moderate cumulative pore volume among the carbon samples. KCP-900 shows the highest cumulative volume of pores, indicating

that the higher activation temperature may promote the formation of more porous structures [16]. The relative amounts of oxygen (O) and nitrogen (N) on the surface are also shown in Table 1. The composition ratio of N/C of the composite

samples is about 3.55% after carbonization at 600°C. The N/C ratio is changed to 3.44%, 1.9%, and 2.2% after KOH activation at 700°C, 800°C, and 900°C, respectively. The O/C ratio shows similar trend with the increase of the activation temperature. The observable changes of the N/C and O/C ratios are taken place at temperatures above 700°C, implying further decomposition of nitrogen functionalities or digestion of the carbon by KOH during the activation process.

**3.2. Capacitive Performance of Carbon Composite KCP Electrode.** Cyclic voltammetric scans were conducted in 6 M KOH at a scan rate of 10 mV·s<sup>-1</sup> to investigate the electrochemical performance of the carbon composite KCP (Figure 5(a)). All these electrodes with the same mass loading (about 6 mg) display similar rectangular shapes in their CV curves and no significant gas evolution in the negative potential range of -1.0~0 V. These wide negative potential ranges can be ascribed to electrochemical reactions of N and O functionalities on these electrodes which lead to higher overpotentials for gas evolution and the increase of energy density for supercapacitors [41]. KCP-800 exhibits the highest current density among these electrodes, indicating the better pseudocapacitive behavior of KCP-800. Otherwise, from the CV curves, KCP-800 and KCP-900 show more rectangular shapes and faster current transfer respond at the potential limits, indicating that dealing with higher temperature in KOH activity process may provide more hierarchical porous structures for carbon materials and thus give rise to the lower resistance for charge transfer throughout the electrode.

The electrical characterization of capacitor electrodes is usefully evaluated with frequency response of their impedance. Figure 5(b) shows frequency responses in the range of 100 kHz to 10 MHz for these electrodes. The distorted semicircle in the high-frequency region and the nearly vertical linear in the low-frequency region indicate the typical capacitive behavior of these electrodes. The RC semicircle is associated with electrochemical process at the electrode-electrolyte interface, which is described as the capacitance ( $C$ ) in parallel with the charge-transfer resistance ( $R_{ct}$ ) due to the charge exchange of electroactive functionality groups such as C-N, C-OH, and -COOH at the interface [42]. The charge-transfer resistance ( $R_{ct}$ ) for composite KCP-800 (1.8 Ω) is much smaller than that of single-silk carbon KSW-800 (8 Ω), implying the synergistic action of two types of carbon materials. The  $R_{ct}$  decreases with the increasing of the activation temperature. The composite KCP-900 exhibits the smallest  $R_{ct}$  (0.37 Ω) and the lowest relaxation time ( $\tau_0$ ) of 3.1 s calculated by using the following equation [27]:

$$\tau_0 = \frac{1}{f_0}, \quad (1)$$

where  $f_0$  is the frequency at phase angle of -45°. The KCP-800 electrode displays the smallest value of  $Z''$  and the highest capacitance of 1.45 F (1000 mF·cm<sup>-2</sup>) at the low frequency of 10 MHz, calculated by the following equation [32]:

$$C = \frac{1}{2\pi f Z''}, \quad (2)$$

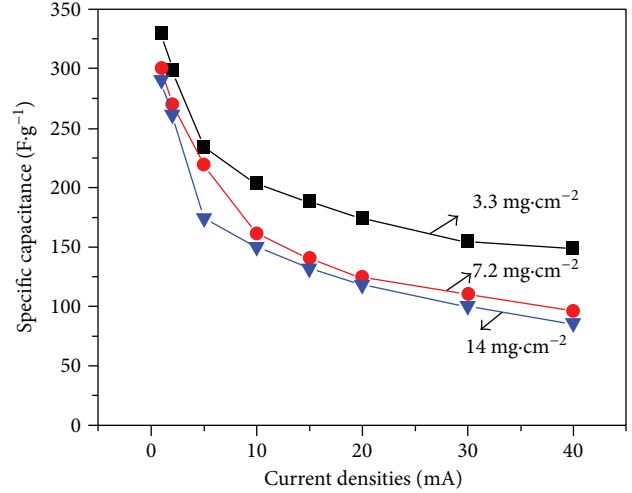


FIGURE 7: The dependence of the specific capacitance on the mass loading of active materials at different current densities.

where  $f$  is the frequency and  $Z''$  is the corresponding imaginary impedance, which is in agreement with the CV and CP results.

The specific capacitances as a function of charge-discharge current densities for these electrodes measured by CP are shown in Figure 5(c). KCP-800 exhibits a maximum specific capacitance of 330 F·g<sup>-1</sup> at 0.5 A·g<sup>-1</sup>, which is superior to the value of KCP-900 (242 F·g<sup>-1</sup>), KCP-700 (218 F·g<sup>-1</sup>), and single-silk carbon KSW-800 (288 F·g<sup>-1</sup>). The specific capacitance is calculated from the following equation [29]:

$$C_s = \frac{I \times \Delta t}{m \times \Delta V}, \quad (3)$$

$$C_A = \frac{I \times \Delta t}{A \times \Delta V},$$

where  $C_s$  is the specific capacitance (F·g<sup>-1</sup>),  $C_A$  is the area specific capacitance (F·cm<sup>-2</sup>),  $I$  is the applied working current (A),  $\Delta t$  is the discharge time (s),  $\Delta V$  is the voltage range,  $m$  is the mass of the KCP of one electrode (g), and  $A$  is the total electrode area (cm<sup>2</sup>). It can be seen that the specific capacitance value of single-silk carbon KSW-800 (red line) decreases more significantly than that of the composite KCP (other lines), indicating the advantage of the combination of silk fibers and phenolic resin-derived carbon materials.

The electrochemical properties of KCP-800 were inspected from 10 to 100 mV·s<sup>-1</sup> using cyclic voltammetry (Figure 6(a)). The CV curves are close to rectangular shapes at scan rates from 10 to 100 mV·s<sup>-1</sup>, indicating a good capacitive behavior of the electrode. It can be observed that KCP-800 possesses fast charge and discharge capability since a nearly linear dependence of current versus the scan rate is identified up to 100 mV·s<sup>-1</sup> (Figure 6(b)). Consistently, the charge/discharge curves in Figure 6(c) exhibit symmetric at different current densities, showing high reversibility and coulombic efficiency (ca. 92%). The KCP-800 electrode can

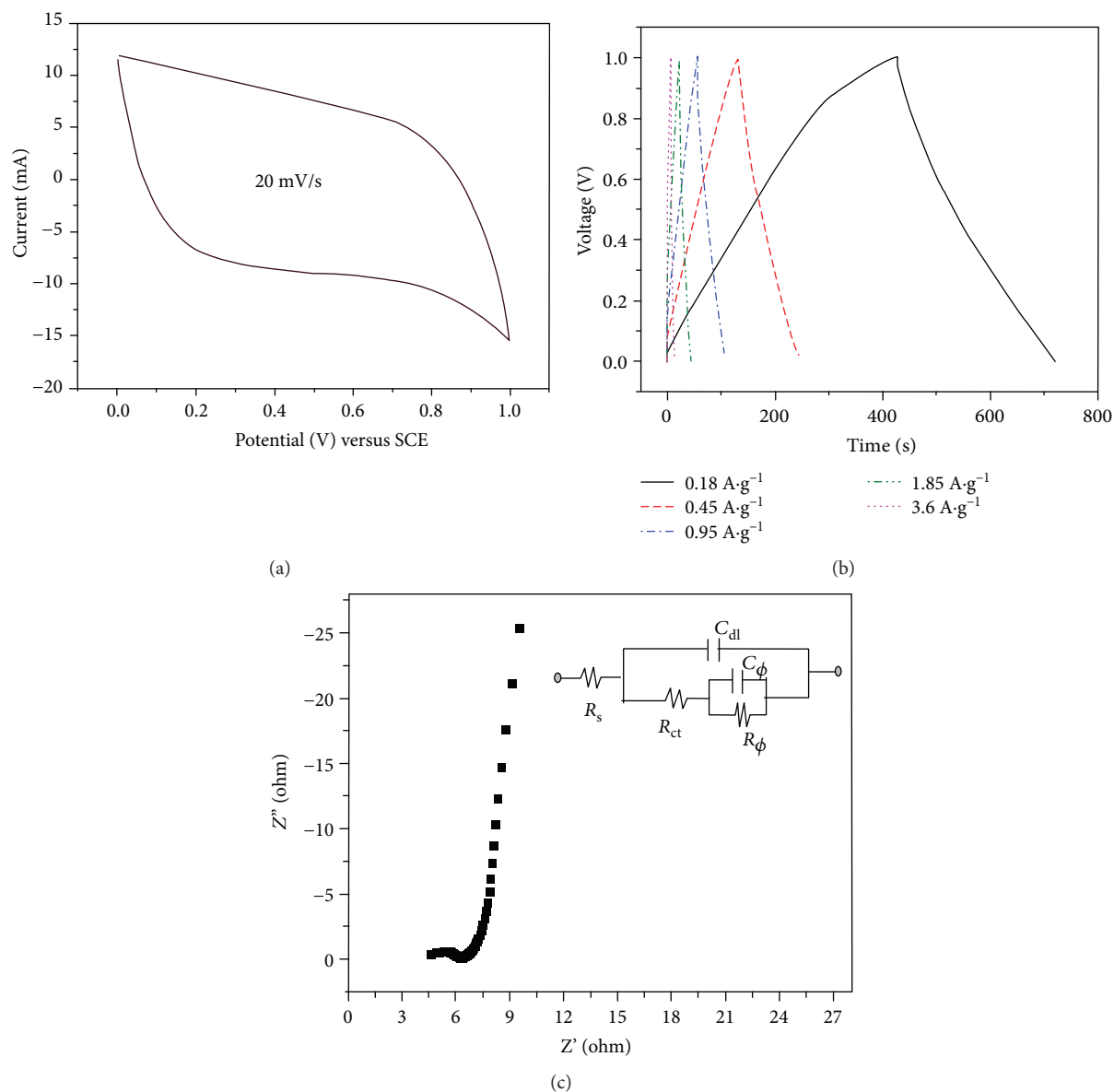


FIGURE 8: (a) CV curve of assembled symmetric ECs based on two KCP electrodes at a scan rate of 20 mV/s. (b) Galvanostatic charging/discharging curves of KCP//KCP symmetric ECs measured with different current densities. (c) Nyquist plots for KCP//KCP supercapacitor measured at 0 V DC potential; inset shows the corresponding equivalent circuit.

deliver an excellent specific capacitance of  $330 \text{ F}\cdot\text{g}^{-1}$  at a current density of  $0.5 \text{ A}\cdot\text{g}^{-1}$ , which is higher than the values recently reported for carbon-based electrodes (Table 2). Even at the high current density of  $12.5 \text{ A}\cdot\text{g}^{-1}$ , KCP-800 can still achieve high charge storage values of  $151 \text{ F}\cdot\text{g}^{-1}$ , showing a high rate capability. The presence of hierarchical porosities and nitrogen/oxygen functionalities is responsible for the high capacitance and good rate capability. The cyclic stability of KCP-800 is also investigated by constant charge-discharge for 10000 cycles at current density of  $3 \text{ A}\cdot\text{g}^{-1}$ . As shown in Figure 6(d), it was retained about 91% of the initial capacitance, showing good stability of the electrode.

It is worth noting that the performance of the capacitors is closely related with thicknesses and mass loading of active materials [45, 46]. The thicker the electrode, the less efficient

is the ion diffusion. As a consequence, the great drop of the capacitive performance often occurs, especially at high loadings. Figure 7 shows the dependence of the specific capacitance on the mass loading of active materials at various charging/discharging current densities. As can be seen, the specific capacitance value at 1 mA decreases from  $330 \text{ F}\cdot\text{g}^{-1}$  for  $3.3 \text{ mg}\cdot\text{cm}^{-2}$  to  $300 \text{ F}\cdot\text{g}^{-1}$  for  $7.2 \text{ mg}\cdot\text{cm}^{-2}$  and  $290 \text{ F}\cdot\text{g}^{-1}$  for  $14 \text{ mg}\cdot\text{cm}^{-2}$ , suggesting that the mass loading of KCP-800 impacts a little influence on the performance of the electrode. KCP-800 can still provide a significant specific capacitance for high mass loading even at high charge/discharge current density of 40 mA. These characters are attributed to the high surface area and excellent ionic diffusion within the hierarchical porous structures of the composite carbon electrode.

Two-electrode KCP//KCP symmetric ECs were also assembled and evaluated by CV, CP, and EIS techniques in 6 M KOH solution. Figure 8(a) shows the CV curve of two electrodes recorded over the voltage range of 1.0 V. The CV curve is close to rectangular shape at a scan rate of 20 mV/s, indicating a good capacitive behavior of the electrode. The galvanostatic charge-discharge profiles of the KCP//KCP ECs at different current densities are shown in Figure 8(b). The specific capacitance of the capacitor was calculated from the discharge curves with the values of 52.8, 51.0, 46.1, 37.8, and 22.3 F·g<sup>-1</sup> obtained from current densities of 0.18, 0.45, 0.9, 1.8, and 3.6 A·g<sup>-1</sup>, respectively. The capacitance retained about 72% when the charge/discharge current density increased from 0.18 to 1.8 A·g<sup>-1</sup>, suggesting the good rate capacity. The voltage drop at the initiation of the discharge is 0.07 V at the current density of 0.45 A·g<sup>-1</sup>, implying a low electron series resistance (ESR) in the cell. The energy density  $E_s$  and power density of the symmetric capacitor are calculated by the following equation [11]:

$$\begin{aligned} E_s &= \frac{1}{2} C_s U^2, \\ P_s &= \frac{E_s}{t}, \end{aligned} \quad (4)$$

where  $C_s$  is the specific capacitance of the total mass of the two electrodes,  $U$  is the operating voltage of the cell, and  $t$  is the discharge time. The cell device achieved a maximum energy density of 7.4 Wh·kg<sup>-1</sup> at a power density of 90.1 W·kg<sup>-1</sup> and 5.3 Wh·kg<sup>-1</sup> at a power density of 900 W·kg<sup>-1</sup>. Figure 8(c) shows the frequency response of the impedance for the KCP//KCP ECs. Nyquist plot displays a nearly linear and vertical characteristic at low frequency, indicating the capacitive behavior of the ECs. An equivalent circuit corresponding to the impedance responses achieved by ZSimpleWin software is in the inset of Figure 8(c), which exhibits the Faradaic pseudocapacitance ( $C_\varphi$ ) in a parallel with the double-layer capacitance ( $C_{dl}$ ), through the charge-transfer resistance ( $R_{ct}$ ) and some possible further Faradaic discharge resistance ( $R_\varphi$ ). The capacitance of the ECs arises from the combination of the Faradaic pseudocapacitance and the double-layer capacitance. The pseudocapacitance should be related to some participation of electrochemical surface reactions involving electron transfer of oxygen and nitrogen functionalities on the carbon electrode [40]. The KCP//KCP ECs show a low charge-transfer resistance ( $R_{ct}$ ) of 1.9 Ω and a high capacitance of 0.63 F at the low frequency of 10 MHz calculated by the (2), suggesting that the KCP-800 electrode is a good candidate for ECs.

#### 4. Conclusion

Hierarchical porous N- and O-doped carbon composites were successfully achieved by a combination of low molecular weight phenolic resin and silk fibers via a hydrothermal method followed by carbonization and KOH activation process. Due to the high surface area, enriched functional group, and hierarchical porous structures, the carbon composite showed excellent capacitive performance up to 330 F·g<sup>-1</sup>

(or 1000 mF·cm<sup>-2</sup>) for 3.3 mg·cm<sup>-2</sup> loading and high rate capability. The prepared carbon shows a good storage capacitance even at high mass loading of active materials (290 F·g<sup>-1</sup> for 14 mg·cm<sup>-2</sup>). The combination of low molecular phenolic resin and silk fibers increases the surface area and enhances the electron transport within active materials. The KCP electrode symmetric ECs are able to deliver a maximum energy density of 7.4 Wh·kg<sup>-1</sup> in a voltage of 1.0 V with 6 M KOH electrolyte solution, suggesting a good prospect for practical applications.

#### Conflicts of Interest

The authors declare that they have no conflicts of interest.

#### Acknowledgments

The authors acknowledge the Liaoning Key Laboratory of Functional Textile Materials and Dalian Institute of Chemical Physics for the technical support of SEM, XRD, TEM, and BET measurements. The authors acknowledge the financial support by the National Natural Science Foundation of China (Project no. 51343002).

#### References

- [1] J. R. Miller, "Engineering electrochemical capacitor applications," *Journal of Power Sources*, vol. 326, pp. 726–735, 2016.
- [2] T. Brousse, D. Bélanger, and J. W. Long, "To be or not to be pseudocapacitive," *Journal of the Electrochemical Society*, vol. 162, no. 5, pp. A5185–A5189, 2015.
- [3] P. Simon and Y. Gogotsi, "Materials for electrochemical capacitors," *Nature Materials*, vol. 7, no. 11, pp. 845–854, 2008.
- [4] P. Simon, Y. Gogotsi, and B. Dunn, "Where do batteries end and supercapacitors begin?," *Science*, vol. 343, no. 6176, pp. 1210–1211, 2014.
- [5] A. Ghosh and Y. H. Lee, "Carbon-based electrochemical capacitors," *ChemSusChem*, vol. 5, no. 3, pp. 480–499, 2012.
- [6] A. González, E. Goikolea, J. A. Barrena, and R. Mysyk, "Review on supercapacitors: technologies and materials," *Renewable and Sustainable Energy Reviews*, vol. 58, pp. 1189–1206, 2016.
- [7] L. G. H. Staaf, P. Lundgren, and P. Enoksson, "Present and future supercapacitor carbon electrode materials for improved energy storage used in intelligent wireless sensor systems," *Nano Energy*, vol. 9, pp. 128–141, 2014.
- [8] A. Chen, Y. Yu, T. Xing, R. Wang, Y. Li, and Y. Li, "Synthesis of nitrogen-doped hierarchical porous carbon for supercapacitors," *Materials Letters*, vol. 157, pp. 30–33, 2015.
- [9] K. Fic, M. Meller, and E. Frackowiak, "Interfacial redox phenomena for enhanced aqueous supercapacitors," *Journal of the Electrochemical Society*, vol. 162, no. 5, pp. A5140–A5147, 2015.
- [10] A. K. Mondal, K. Kretschmer, Y. Zhao, H. Liu, H. Fan, and G. Wang, "Naturally nitrogen doped porous carbon derived from waste shrimp shells for high-performance lithium ion batteries and supercapacitors," *Microporous and Mesoporous Materials*, vol. 246, pp. 72–80, 2017.
- [11] W. Si, J. Zhou, S. Zhang, S. Li, W. Xing, and S. Zhuo, "Tunable N-doped or dual N, S-doped activated hydrothermal carbons derived from human hair and glucose for supercapacitor applications," *Electrochimica Acta*, vol. 107, pp. 397–405, 2013.

- [12] J. Wei, D. Zhou, Z. Sun, Y. Deng, Y. Xia, and D. Zhao, "A controllable synthesis of rich nitrogen-doped ordered mesoporous carbon for CO<sub>2</sub> capture and supercapacitors," *Advanced Functional Materials*, vol. 23, no. 18, pp. 2322–2328, 2013.
- [13] J. Jiang, L. Bao, Y. Qiang et al., "Sol-gel process-derived rich nitrogen-doped porous carbon through KOH activation for supercapacitors," *Electrochimica Acta*, vol. 158, pp. 229–236, 2015.
- [14] C. Zhang, R. Kong, X. Wang et al., "Porous carbons derived from hypercrosslinked porous polymers for gas adsorption and energy storage," *Carbon*, vol. 114, pp. 608–618, 2017.
- [15] J. Jiang, H. Chen, Z. Wang et al., "Nitrogen-doped hierarchical porous carbon microsphere through KOH activation for supercapacitors," *Journal of Colloid and Interface Science*, vol. 452, pp. 54–61, 2015.
- [16] P. Li, C. Xing, S. Qu, B. Li, and W. Shen, "Carbon dioxide capturing by nitrogen-doping microporous carbon," *ACS Sustainable Chemistry & Engineering*, vol. 3, no. 7, pp. 1434–1442, 2015.
- [17] Y. J. Kim, Y. Abe, T. Yanagiura et al., "Easy preparation of nitrogen-enriched carbon materials from peptides of silk fibroins and their use to produce a high volumetric energy density in supercapacitors," *Carbon*, vol. 45, no. 10, pp. 2116–2125, 2007.
- [18] Y. Zhu, S. Murali, M. D. Stoller et al., "Carbon-based supercapacitors produced by activation of graphene," *Science*, vol. 332, no. 6037, pp. 1537–1541, 2011.
- [19] J. Yi, Y. Qing, C. T. Wu et al., "Lignocellulose-derived porous phosphorus-doped carbon as advanced electrode for supercapacitors," *Journal of Power Sources*, vol. 351, pp. 130–137, 2017.
- [20] Q. Wang, J. Yan, Z. Dong, L. Qu, and Z. Fan, "Densely stacked bubble-pillared graphene blocks for high volumetric performance supercapacitors," *Energy Storage Materials*, vol. 1, pp. 42–50, 2015.
- [21] S. S. Balaji, A. Elavarasan, and M. Sathish, "High performance supercapacitor using N-doped graphene prepared via supercritical fluid processing with an oxime nitrogen source," *Electrochimica Acta*, vol. 200, pp. 37–45, 2016.
- [22] Y. Li, S. Zhang, H. Song, X. Chen, J. Zhou, and S. Hong, "New insight into the heteroatom-doped carbon as the electrode material for supercapacitors," *Electrochimica Acta*, vol. 180, pp. 879–886, 2015.
- [23] C. Tang, Y. Liu, D. Yang, M. Yang, and H. Li, "Oxygen and nitrogen co-doped porous carbons with finely-layered schistose structure for high-rate-performance supercapacitors," *Carbon*, vol. 122, pp. 538–546, 2017.
- [24] Q. Shi, R. Zhang, Y. Lv, Y. Deng, A. A. Elzatahrya, and D. Zhao, "Nitrogen-doped ordered mesoporous carbons based on cyanamide as the dopant for supercapacitor," *Carbon*, vol. 84, pp. 335–346, 2015.
- [25] Z. Gao, X. Liu, J. Chang et al., "Graphene incorporated, N doped activated carbon as catalytic electrode in redox active electrolyte mediated supercapacitor," *Journal of Power Sources*, vol. 337, pp. 25–35, 2017.
- [26] H.-F. Yen, Y. Y. Horng, M. S. Hu et al., "Vertically aligned epitaxial graphene nanowalls with dominated nitrogen doping for superior supercapacitors," *Carbon*, vol. 82, pp. 124–134, 2015.
- [27] T. Lin, I.-W. Chen, F. Liu et al., "Nitrogen-doped mesoporous carbon of extraordinary capacitance for electrochemical energy storage," *Science*, vol. 350, no. 6267, pp. 1508–1513, 2015.
- [28] K. Wang, M. Xu, Y. Gu, Z. Gu, and Q. H. Fan, "Symmetric supercapacitors using urea-modified lignin derived N-doped porous carbon as electrode materials in liquid and solid electrolytes," *Journal of Power Sources*, vol. 332, pp. 180–186, 2016.
- [29] Y. Chen, Z. Gao, B. Zhang, S. Zhao, and Y. Qin, "Graphene coated with controllable N-doped carbon layer by molecular layer deposition as electrode materials for supercapacitors," *Journal of Power Sources*, vol. 315, pp. 254–260, 2016.
- [30] L. Qie, W. Chen, H. Xu et al., "Synthesis of functionalized 3D hierarchical porous carbon for high-performance supercapacitors," *Energy & Environmental Science*, vol. 6, no. 8, pp. 2497–2505, 2013.
- [31] J. Shao, F. Ma, G. Wu et al., "Facile preparation of 3D nanostructured O/N co-doped porous carbon constructed by interconnected carbon nanosheets for excellent-performance supercapacitors," *Electrochimica Acta*, vol. 222, no. 20, pp. 793–805, 2016.
- [32] B.-X. Zou, Y. Gao, B. Liu, Y. Yu, and Y. Lu, "Three dimensional heteroatom-doped carbon composite film for flexible solid-state supercapacitors," *RSC Advances*, vol. 6, no. 6, pp. 4483–4489, 2016.
- [33] X. He, H. Yu, L. Fan, M. Yu, and M. Zheng, "Honeycomb-like porous carbons synthesized by a soft template strategy for supercapacitors," *Materials Letters*, vol. 195, pp. 31–33, 2017.
- [34] K. S. W. Sing, "Reporting physisorption data for gas/solid systems with special reference to the determination of surface area and porosity (provisional)," *Pure and Applied Chemistry*, vol. 54, no. 11, pp. 2201–2218, 1982.
- [35] X. Xu, J. Gao, Q. Tian, X. Zhai, and Y. Liu, "Walnut shell derived porous carbon for a symmetric all-solid-state supercapacitor," *Applied Surface Science*, vol. 411, pp. 170–176, 2017.
- [36] H. Jin, X. Wang, Z. Gu, Q. Fan, and B. Luo, "A facile method for preparing nitrogen-doped graphene and its application in supercapacitors," *Journal of Power Sources*, vol. 273, pp. 1156–1162, 2015.
- [37] D. Liu, C. Zeng, D. Qu et al., "Highly efficient synthesis of ordered nitrogen-doped mesoporous carbons with tunable properties and its application in high performance supercapacitors," *Journal of Power Sources*, vol. 321, pp. 143–154, 2016.
- [38] X. Laloyaux, E. Fautré, T. Blin et al., "Temperature-responsive polymer brushes switching from bactericidal to cell-repellent," *Advanced Materials*, vol. 22, no. 44, pp. 5024–5028, 2010.
- [39] F. Gao, J. Qu, Z. Zhao, Z. Wang, and J. Qiu, "Nitrogen-doped activated carbon derived from prawn shells for high-performance supercapacitors," *Electrochimica Acta*, vol. 190, pp. 1134–1141, 2016.
- [40] D.-W. Wang, F. Li, L.-C. Yin et al., "Nitrogen-doped carbon monolith for alkaline supercapacitors and understanding nitrogen-induced redox transitions," *Chemistry - A European Journal*, vol. 18, no. 17, pp. 5345–5351, 2012.
- [41] B. You, L. Wang, L. Yao, and J. Yang, "Three dimensional N-doped graphene-CNT networks for supercapacitor," *Chemical Communications*, vol. 49, no. 44, pp. 5016–5018, 2013.
- [42] B.-X. Zou, Y. Liang, X. X. Liu, D. Diamond, and K. T. Lau, "Electrodeposition and pseudocapacitive properties of tungsten oxide/polyaniline composite," *Journal of Power Sources*, vol. 196, no. 10, pp. 4842–4848, 2011.
- [43] Z. Bo, S. Mao, Z. Jun Han, K. Cen, J. Chen, and K. (. K.). Ostrikov, "Emerging energy and environmental applications

- of vertically-oriented graphenes,” *Chemical Society Reviews*, vol. 44, no. 8, pp. 2108–2121, 2015.
- [44] X. He, H. Ma, J. Wang, Y. Xie, N. Xiao, and J. Qiu, “Porous carbon nanosheets from coal tar for high-performance supercapacitors,” *Journal of Power Sources*, vol. 357, pp. 41–46, 2017.
- [45] Y. Gogotsi and P. Simon, “True performance metrics in electrochemical energy storage,” *Science*, vol. 334, no. 6058, pp. 917–918, 2011.
- [46] K. Shi and I. Zhitomirsky, “Fabrication of polypyrrole-coated carbon nanotubes using oxidant–surfactant nanocrystals for supercapacitor electrodes with high mass loading and enhanced performance,” *ACS Applied Materials & Interfaces*, vol. 5, no. 24, pp. 13161–13170, 2013.